

**Integrated nonlinear photonics based on coupled-cavity
resonator systems**

by

Xiaoge Zeng

B.S., University of Science and Technology of China, 2008

M.S., University of Colorado Boulder, 2011

A thesis submitted to the
Faculty of the Graduate School of the
University of Colorado in partial fulfillment
of the requirements for the degree of
Doctor of Philosophy
Department of Physics

2016

This thesis entitled:
Integrated nonlinear photonics based on coupled-cavity resonator systems
written by Xiaoge Zeng
has been approved for the Department of Physics

Prof. Miloš A. Popović

Prof. Juliet Gopinath

Dr. Richard Mirin

Prof. James Thompson

Prof. Kelvin Wagner

Date _____

The final copy of this thesis has been examined by the signatories, and we find that both the content and the form meet acceptable presentation standards of scholarly work in the above mentioned discipline.

Zeng, Xiaoge (Ph.D., Physics)

Integrated nonlinear photonics based on coupled-cavity resonator systems

Thesis directed by Prof. Miloš A. Popović

Efficient nonlinear optical devices are designed and demonstrated in “photonic molecule”-like coupled-cavity resonator systems on a semiconductor chip. A coupled-cavity resonator may be designed to support distributed supermodes, and to allow independent control of the resonant frequency and linewidth of each supermode. Such control allows reduction of dispersion without compromising effective nonlinearity in the resonator, as well as the design of anisotropic output coupling or radiation that allows optimized nonlinear functions. Therefore this resonator manifests itself as a favorable platform for building nonlinear devices including optical parametric wavelength converters and oscillators based on four-wave mixing that call for different couplings to the signal, pump and idler modes. A physical model based on coupled-mode theory describes all relevant linear and nonlinear processes in triply-resonant microcavities, and a generalization of the usual nonlinear figure of merit is proposed to evaluate the effects of distributed supermodes on nonlinear conversion efficiency in such devices. Experimental work is presented that demonstrates coupled cavity devices for wavelength conversion in crystalline silicon, where two-photon absorption sets conversion efficiency limitations. In addition, an investigation of deposition conditions of hydrogenated amorphous silicon is described where amorphous silicon allows for a higher nonlinear figure of merit than crystalline silicon, promising increased performance in such devices. More generally, mode interference and coupling in coupled-cavity resonators, as a unique degree of freedom in integrated optics, is explored through designs of linear devices including efficient optical filters, wavelength converters, and modulators.

Dedicated

To my wife, Wanyan
to my brother, parents and grandparents

Acknowledgements

This thesis documents aspects of my research work over the past six years. Many people have provided support in my pursuit of Ph.D. degree, and my appreciation for their help will go on.

First of all, I owe many thanks to my adviser, Prof. Miloš A. Popović. As a professor, he is very approachable and easygoing to students. His way of designing optical devices by starting from the basic Maxwell equations resonates very well with my desire of thoroughly understanding fundamental physics behind applied scientific problems. His enthusiasm for research has infected me, and I always remember him patiently teaching me how to write and present more professionally.

I also learnt a lot from my colleagues at the Nanophotonics System Laboratory at the University of Colorado Boulder – Yangyang Liu, Dr. Jeff Shainline, Cale Gentry, Mark Wade, Chris Poulton, Dr. Fabio Pavanello, Dr. Rajesh Kumar, Gil Triginer and other group members not listed. They all have unique perspectives on research, and discussing problems with them has always been fun.

A lot of people outside of the lab have aided me in the course of my Ph.D. program. In particular, Prof. Kelvin Wagner taught me the course of nonlinear optics, the single-photon detector team led by Dr. Sae Woo Nam and Dr. Richard Mirin at NIST brought me insights on quantum optics through the collaboration, Dr. Jason Pelc guided me on nonlinear material research during my internship at Hewlett-Packard Laboratories, Dr. Andrew Funk introduced me to fiber optics at the Cundiff laboratory, and the staff at CNL trained me on nanofabrication and characterization. And I thank all my committee members for giving advice on the thesis.

Studying abroad without good friends would be a lonely experience. I have been lucky to meet Jianfeng Xie, Weisen Shen and Zhibin Yu (just to name a few), and I thank them for their friendship and help in my life outside the lab.

My greatest gratitude goes to my family. Their love has built me a warm and harmonious place called “home”, no matter where I go. My parents and grandparents consistently respect and support my ideas. Their pride in me always gives me strength. I am indebted to my brother for taking care of the family while I was away, especially during family misfortune. Last but not most, I am deeply grateful for my wife, Wanyan, who has sacrificed a lot while accompanying me through this arduous and long journey.

Contents

Chapter

1	Introduction	1
1.1	Overview of integrated photonics	1
1.2	Overview of integrated nonlinear optics	2
1.3	Outline of the thesis	4
2	Coupled-cavity resonator systems for nonlinear optics	7
2.1	Microcavity	7
2.1.1	Microring cavity	8
2.1.2	Photonic crystal nanobeam cavity	9
2.2	Low-loss directional couplers	10
2.3	Coupled-cavity resonators	12
2.3.1	Triple-cavity resonators	13
3	Development of amorphous silicon as an efficient nonlinear material	18
3.1	Growth of hydrogenated amorphous silicon material	21
3.2	Characterization of a-Si:H	23
3.2.1	Linear refractive index, absorption and microstructure	23
3.2.2	Kerr coefficient	26
3.2.3	Nonlinear absorption	28

4	Theory of coupled-cavity four-wave mixing and a generalized nonlinear figure of merit	35
4.1	A nonlinear optics model based on coupled-mode theory	35
4.2	Cavity mode topology and effective nonlinear figure of merit	40
5	Optical parametric wavelength conversion	46
5.1	Theoretical efficiency and optimum designs	47
5.2	Experiment demonstration: four-wave mixing in silicon coupled-cavity resonators with port-selective, orthogonal supermode excitation	52
5.3	Estimate of energy cost for data bit conversion based on four-wave mixing	58
6	Optimum design of optical parametric oscillators	60
6.1	Introduction	60
6.2	Physical model of a parametric oscillator	63
6.2.1	Normalized model of a parametric oscillator	65
6.3	Approach to finding the optimum OPO design	67
6.3.1	Traveling-wave single-cavity model with pump-assisted TPA only and no FCA	69
6.3.2	Model with full TPA but no FCA	78
6.3.3	Model with full TPA and FCA	84
6.4	Extension of analysis to coupled-cavity systems with distributed resonance modes . .	89
6.5	Future work and conclusion	91
7	Conclusion	94
7.1	Summary of major achievements	94
7.2	Remaining challenges and future work	96

Bibliography	99
---------------------	-----------

Appendix

A Nonlinear coupling coefficients	106
A.1 Nonlinear coupling coefficients and effective mode volume in microresonators	107
A.2 Nonlinear coupling coefficients and effective mode area in waveguides	109
A.3 Conversion formulas for nonlinear parameters	110
A.4 Comparison of nonlinear coupling coefficients in single- and triple-cavity resonators with travelling-wave and standing-wave excitations	111
A.5 Free carrier absorption coefficients	112

Tables

Table

3.1	Growth conditions of a-Si:H in PECVD	22
4.1	Third-order nonlinear properties of some common on-chip nonlinear material	42
4.2	Comparison of FWM and TPA coefficients in various cavity topologies	45
6.1	Predicted performance of optical parametric oscillators based on some common on-chip nonlinear material in a single-ring cavity with traveling-wave mode	81
6.2	Predicted performance of optical parametric oscillators based on 3-ring photonic molecule with traveling-wave mode	91
A.1	Comparison of longitudinal field profiles of single- and triple-ring resonator with travelling-wave and standing-wave excitations. Each constituent ring of the triple-ring cavity is identical to the single-ring cavity. The amplitude of each field has been chosen to have equal energy in all resonator.	112

Figures

Figure

2.1	SEM pictures of single and triple microring and one-dimensional single and triple photonic crystal cavities designed in the course of this thesis work.	9
2.2	Low-loss cavity-bus couplers with: (a) a curved bus with equal curvature as the ring cavity; (b) a straight bus coupled to a straight section of a racetrack cavity; (c) a bus interferometrically coupled to a cavity via two coupling region; and (d) a combination of techniques used in (a) and (c). In all couplers, a combination of large coupler gap and large coupling length is used.	12
2.3	Low-loss cavity-cavity couplers with: (a) straight waveguides in the coupling region between two racetrack cavities; (b) curved waveguides with similar curvature at the coupling region between racetrack and ring cavities; (c) curved waveguides with similar curvature at the coupling region between ring cavities, where each individual cavity is accessible by external waveguides; and (d) indirect coupling between two ring cavities via connecting buses taking advantage of low-loss cavity-bus couplers. In all couplers, the ring cavity is designed to have low loss, and a combination of large coupler gap and large coupling length is used.	12

2.4	(a) Schematic of proposed triple-cavity resonator system. It has three microrings coupled in series and two access bus waveguides. One bus couples to the outer two cavities, and the other bus couples only to the middle cavity; (b) Density of states (DoS) versus frequency (with arbitrary unit) in the proposed triple-cavity resonator. Due to cavity-cavity coupling, there are three supermodes at each longitudinal order.	14
2.5	Simulated supermode field profile of triple-ring resonator with resonance frequency of: (a) $\omega_0 - \Delta\omega$, (b) ω_0 and (c) $\omega_0 + \Delta\omega$. showing suppressed coupling of signal bus to pump resonance and pump bus to signal/idler resonances.	16
2.6	(a) Schematic illustrating mode-selective coupling to ports; (b) effect of choices of the “pump bus” and “signal bus” gaps, in the proposed orthogonal supermode linewidth engineering scheme.	17
3.1	A schematic illustration of the electronic density of states in hydrogenated amorphous silicon. VB: valence band; CB: conduction band. The red dashed line denotes the mobility edges.	20
3.2	Hydrogenated amorphous silicon fabrication and characterization procedure.	23
3.3	Linear optical properties of hydrogenated amorphous silicon (a-Si:H). (a) Real (n) and imaginary (k) parts of the complex refractive index of an a-Si:H film measured by spectral ellipsometry; (b) Absorption spectrum of an a-Si:H film characterized by Fourier transform infrared spectroscopy. The relative absorption strength at different characteristic frequencies reveals the microstructure of a-Si:H films; (c) Linear optical loss versus lengths of a-Si:H waveguides.	25
3.4	Experimental setup for measuring Kerr coefficient based on picosecond pulse linewidth broadening in an a-Si:H waveguide. Abbreviations: MLL, mode-locked laser; TBPF, tunable band-pass filter; EDFA, erbium-doped fiber amplifier; VATT, variable optical attenuator; PC, polarization controller; OSA, optical spectrum analyzer.	27

3.5	Pulse spectrum broadening due to self-phase modulation. (a) Power spectral density at different pulse peak power as measured by OSA; (b) Root-mean-square (RMS) of the angular frequency components of the pulse ($\Delta\omega_{\text{rms}}$) versus on-chip peak power. The slope of the fitted line is proportional to the Kerr coefficient n_2	27
3.6	Experimental setup for pump-probe measurements of transient nonlinear absorption in an a-Si:H waveguide. Abbreviations: MLL, mode-locked laser; TBPF, tunable band-pass filter; EDFA, erbium-doped fiber amplifier; VATT, variable optical attenuator; PC, polarization controller; WDM, wavelength-division multiplexer; OSA, optical spectrum analyzer. The pump light and probe light travel in different channels of WDM.	29
3.7	Transient absorption of the probe light in the pump-probe experiment. (a) Fractional absorption of the probe light versus time at different pump pulse peak power. The fitted τ_e is about 3.0 ps.; (b) Absorption coefficient at pump-probe delay (Δt) of a third of fitted decay time (τ_e) of the in-gap states, versus pump pulse peak intensity.	30
4.1	(a) Cartoon of a general triply-resonant resonator system with third-order nonlinearity. It has three resonance modes interacting via $\overline{\chi}^{(3)}$ -based effect, including four-wave mixing, cross-phase modulation and cross two-photon absorption. Each resonance mode also couples to an external waveguide mode, represented by an excitation field $S_{k,+}$ ($k \in \{p, s, i\}$) and field decay rate of $r_{k,\text{ext}}$ ($k \in \{p, s, i\}$). Besides, all resonance modes decay due to a combination of linear and nonlinear loss; (b) An example triply-resonant resonator system has a microring cavity with three travelling-wave resonance modes and a single bus waveguide coupled to the ring cavity.	36

4.2	Example microring cavity topology for illustration of effective figure of merit: (a) single-ring cavity with traveling-wave mode; (b) single-ring cavity with standing-wave mode; (c) triple-ring cavity with traveling-wave mode; (d) triple-ring cavity with standing-wave mode.	43
4.3	Mode fields of the pump, signal and idler resonances for the configurations (a)–(d) in Fig. 4.2 (color-coded intensity scales are different in single and triple-cavity cases in order to show the mode features clearly).	44
4.4	Mode overlap integrand for the FWM and various TPA coefficients for configurations (a)–(d) in Fig. 4.2. It shows that a vector of FOM is needed to account for the ratio of FWM relative to various TPA terms. Besides, different cavity topologies have different FOM (see Table 4.2).	44
5.1	(a) Micrographs of device under test with heaters; (b) optical transmission spectra of four port combinations (legend: “ps”=“pump bus” input, “signal bus” output). The little transmission dips E (A,C) show that “signal (pump) bus” couples weakly to pump (signal/idler) resonance.	55
5.2	(a) Seeded FWM in silicon triple-ring resonator with conversion efficiency of -54 dB. (b) Degenerate-pump FWM wavelength conversion efficiency vs. normalized pump power [1] in a silicon microcavity with nonlinear loss included. Critical coupling and perfect phase matching are assumed. A few ratios of free carrier and photon lifetime are used.	57
6.1	(a) Illustration of the micro-OPO model including a multimode resonator; (b) a traveling-wave resonant structure enables separated input and output ports; (c) example proposed multimode resonator based on 3 coupled microring cavities, showing an approach to unequal pump and signal/idler external coupling [2].	62

6.2	Normalized design curves for optimum OPO (using a “partial-TPA” model with pump-assisted TPA terms only and no FCA included): (a) maximum pump-to-signal/idler conversion efficiency versus pump power (normalized by oscillation threshold when loss due to TPA is ignored) and nonlinear loss sine [defined in Eq. (4.11)]; (b) corresponding optimum pump resonance coupling normalized by cavity intrinsic loss; (c) corresponding optimum ratio of signal/idler relative to pump resonance coupling.	76
6.3	Performance comparison of OPO designs with optimum unequal pump and signal/idler couplings and with optimized equal couplings (assuming no FCA): (a) power conversion efficiency; (b) optimum coupling values.	78
6.4	Normalized design curves for optimum OPO (I) using a “full-TPA” model (with all TPA terms but no FCA included) and (II) comparison of “partial-TPA” and “full-TPA” models (assuming no FCA): (a) maximum efficiency versus pump power and nonlinear loss sine, and corresponding (b) pump resonance coupling and (c) ratio of signal/idler relative to pump resonance coupling in (I) and signal/idler resonance coupling in (II). See Fig. 6.2 for parameter definitions.	80
6.5	Optimum OPO design curves for nonlinear media with and without TPA loss (assuming no FCA), representative of, e.g., of silicon nitride at 1550 nm and Si at 2.3 μm (linear), and Si at 1550 nm ($\sigma_3 = 0.23$).	82
6.6	Performance of silicon microcavity at 1550 nm resonance with various free-carrier lifetime and intrinsic cavity quality factors.	85
6.7	The OPO threshold vs (a) normalized free carrier lifetime and σ_3 ; (b) free carrier lifetime for silicon cavity resonant near 1550 nm with linear unloaded Q of 10^6 and effective volume of $8.4 \mu\text{m}^3$	87
6.8	Small signal gain and loss in an optical parametric oscillator based on degenerate four wave mixing.	89

A.1 Illustration of the atomic transition processes in cross two-photon absorption (cross TPA) and self two-photon absorption (self TPA). For the atomic transition from electronic state $ 1\rangle$ to $ 3\rangle$, there are two transition paths in cross TPA compared to a single transition path in self TPA. As a result of the quantum interference between the two transition paths, cross TPA has a factor of 4 in generating free carriers compared to self TPA.	115
--	-----

Chapter 1

Introduction

1.1 Overview of integrated photonics

Integrated photonics is the study of constructing integrated micro-scale optical devices to fulfil various photonic functionalities. It wins over the conventional bulk optics in a few aspects. First of all, on-chip optical devices have small footprint, and thousands of them can be densely integrated to realize complex optical functionalities. In addition, devices fabricated on a solid chip have stable performance with less sensitivity to environmental vibrations compared to free optics. There are also unique degrees of freedom in designing optical devices on a chip [3, 4, 5]. For example, microresonators have large free spectral range and wavelength-dependent coupling to external ports, which are useful properties in designing single-mode lasers [6] and optical parametric oscillators [1], respectively. Another inherent advantage of building optical devices on a semiconductor chip is the capability of integration with the mature advanced CMOS electronics [7, 8]. Complex electric circuits can be easily fabricated next to the photonic devices, and utilized to control photonic devices with high speed and low energy cost.

Integrated photonics, especially silicon photonics, has undergone rapid advances in recent years, and an abundance of linear optical devices have been developed. Such devices include grating couplers for fiber-to-chip optical coupling, low-loss optical waveguides for routing of light, beam splitter and combiners, polarization rotating devices, optical filters for selecting optical signals according to their wavelengths, optical modulators for encoding information to light carriers, optical detectors based on linear absorption for decoding optical signals and thermal heaters for post-

fabrication tuning, wavelength-selective switches and optical buffers based on delay lines and so on. Most importantly, in addition to on-chip optical signal processing, integrated optics can also be employed as a platform for cross-discipline research, such as RF signal processing, optical sensors, optical microfluidics, opto-mechanics taking advantage of the mature MEMS technology.

However, as one important building element of integrated photonics, an integrated light source is still missing in silicon photonics. Although on-chip light sources can be built from III-V materials with optical gain at telecom bands, and then heterogeneously integrated onto silicon chips where optical signals are processed, it is desirable to have light sources on the silicon chip for reduced fabrication complexity and cost, enhanced signal processing speed and in cases when chip bonding and deposition of exotic gain materials are not feasible. Although on-chip lasers have been directly built on silicon using Raman gain [9], the demonstrated lasing wavelength range was limited. One alternative feasible approach for generating coherent light on chip is to make use of optical parametric gain which is characterized with broad gain bandwidth. Moreover, on-chip optical parametric oscillators can produce new wavelengths from a single wavelength of input pump light, and even optical pulses of coherent comb light from a CW pump, for the applications of e.g. sensing[10], photonic A/D conversion etc. In addition, all-optical control is desired in many ultrafast optical devices such as switches [11] and logic gates for optical computing [12]. All these applications motivate the study of integrated nonlinear optics.

1.2 Overview of integrated nonlinear optics

A broad definition of material optical nonlinearity is the change of the optical property of the material due to the optical field itself. Since the optical property of a material, characterized by the complex refractive index, is affected by factors such as temperature, material density and vibration of constituent molecules, an optical field can indirectly change the refractive index. For example, photons can be absorbed resulting in material temperature change (called thermal nonlinearity). And in stimulated Brillouin scattering and stimulated Raman scattering, photons are scattered by acoustic and optical phonons, respectively, with the phonon density amplified by optical intensity.

In this thesis, focus is put on the direct optical nonlinearity characterized by the susceptibility due to bound electrons, $\overline{\overline{\chi}}$.

Specifically, the direct reaction of a material to the light field is conveniently described by the polarization, $\mathbf{P}(t)$, which is a function of the vector optical field, $\mathbf{E}(t)$:

$$\mathbf{P}(t) = \epsilon_0 \left[\overline{\overline{\chi}}^{(1)} \mathbf{E}(t) + \overline{\overline{\chi}}^{(2)} \mathbf{E}^2(t) + \overline{\overline{\chi}}^{(3)} \mathbf{E}^3(t) + \dots \right] \quad (1.1)$$

where ϵ_0 is the permittivity of free space, $\overline{\overline{\chi}}^{(1)}$ is the linear optical susceptibility, $\overline{\overline{\chi}}^{(2)}$ and $\overline{\overline{\chi}}^{(3)}$ are the second- and third-order nonlinear optical susceptibility. For most centrosymmetric crystals and amorphous materials used in CMOS chip fabrication, $\overline{\overline{\chi}}^{(2)}$ is 0 due to the existence of inversion symmetry. Therefore the lowest-order, dominant nonlinear susceptibility is $\overline{\overline{\chi}}^{(3)}$. Its real part is related to nonlinear phase shift (ϕ_{NL}), which is the origin of new optical frequency components generation. Its imaginary part denotes two-photon absorption rate, and is detrimental in most nonlinear optical devices (except in photo-detectors based on two-photon absorption [13]). Usually a large ratio of real versus imaginary part of $\overline{\overline{\chi}}^{(3)}$ is preferred. Notably, the absolute value of $\overline{\overline{\chi}}^{(3)}$ is relevant in some nonlinear processes such as four-wave mixing (see Appendix A.1).

The strength of third-order optical nonlinearity in an optical device is usually characterized by the beneficial nonlinear phase shift $\phi_{\text{NL}} \equiv \Delta n k_0 L_{\text{eff}}$, where the nonlinear index change is intensity dependent, $\Delta n = n_2 I$. The Kerr coefficient, n_2 , is related to the real part of $\overline{\overline{\chi}}^{(3)}$ (see Eq. A.19). The optical nonlinearity is greatly enhanced in nanowaveguides thanks to the enhanced optical intensity of strongly confined modes. Common semiconductor materials such as silicon and silicon nitride also have greater Kerr coefficients than that of silicon oxide in optical fiber.

The optical nonlinearity can be further enhanced in optical microcavities due to further resonant enhancement of optical intensity [14]. Thus it is desirable to build nonlinear devices based on microresonators where the interacting waves are resonant. For devices based on four-wave mixing (FWM), a minimum of three resonant modes are needed if two of the wave frequencies are chosen to be degenerate. This thesis focuses on degenerate-pump FWM in triply-resonant cavities.

Efficient optical nonlinear interaction also demands phase matching among interacting waves.

Phase mismatch is mainly dependent on mode dispersion, which is dominated by the waveguiding effect in micro-structures. Unfortunately mode dispersion is substantial in optical waveguides and microcavities due to the strong field confinement. To minimize mode dispersion, the dimensions of waveguide cross sections have to be carefully chosen [15], putting constraint on fabrication accuracy. However, mode dispersion can be easily controlled in coupled-cavity resonators as explained in Chapter 2.

A coupled-cavity resonator system can also have different linewidth for its compound resonant modes based on different coupling rates to bus waveguides, and therefore manifest itself as a favorable platform for building several nonlinear devices including optical parametric oscillators, wavelength converters, correlated photo pair quantum light sources and so on. For example, optical parametric wavelength converters prefer a weak critical coupling to the pump resonance and a strong coupling to the signal resonance, in order to simultaneously provide maximum parametric gain and allow for a large signal bandwidth. In addition, the generated weak signal can be separated from the strong pump light by design in triple-cavity resonators.

Optical nonlinearity in optical waveguides and single microcavities has enabled on-chip, coherent light generation for many classical photonics applications, including light sources at wavelengths where gain media are underdeveloped, optical frequency comb generation [16, 17], and optical data stream wavelength conversion [14]. It has also enabled ultrafast all-optical switching [11] for optical communication as well as optical logic gates for optical computing [12]. Moreover, on-chip optical nonlinearity has been employed to study quantum optics, including for heralded single photon [18] and correlated photon pair generation [19, 20]. It is of interest to build these nonlinear devices on coupled-cavity resonator systems to take advantage of their unique mode structures.

1.3 Outline of the thesis

In this thesis a few nonlinear optical devices based on coupled-cavity resonator systems are designed and demonstrated. Chapter 2 describes the coupled-cavity resonator systems which have unique compound mode structures for efficient on-chip nonlinear interactions. The design of the

constituent microcavity is summarized, with emphasis on the commonly used microring cavities and photonic crystal beam cavities. Low-loss directional couplers are critical for both cavity-cavity coupling and cavity-waveguide coupling, and a few design guidelines are provided. The complex resonance modes of both dual-cavity and triple-cavity resonators are examined, and their special properties for controlling dispersion and tailoring nonlinear interaction processes are explained.

One essential building block of all integrated nonlinear optical devices is nonlinear materials, and Chapter 3 is devoted to describing the fabrication and characterization of a common nonlinear material, hydrogenated amorphous silicon (a-Si:H). Specifically, the conditions for growing a-Si:H films are optimized to reduce linear and nonlinear loss. The linear refractive index, linear loss, Kerr coefficient and nonlinear absorption rate of a-Si:H samples are measured, and a nonlinear two-state absorption model is utilized to explain the observed non-instantaneous nonlinear absorption.

In Chapter 4, a general physical model for integrated nonlinear optics is built based on the coupled-mode theory. This model uses degenerate four-wave mixing in triply-resonant cavities as an example, and includes all linear and nonlinear processes relevant for the design of efficient optical devices. Such processes include the parasitic two-photon absorption and free carrier absorption relevant in low-bandgap materials like crystalline silicon. In the model, a vector of effective figures of merit are also introduced to take into account the distributed mode profile of coupled-cavity resonators.

Chapter 5 presents both theoretical and experimental studies on optical parametric wavelength conversion (OPWC) based on stimulated four-wave mixing. The theoretical investigation summarizes the design for efficient OPWC by controlling resonance detuning, phase mismatch and coupling rates. The experiment demonstration shows OPWC in silicon triple-ring resonators, where the pump and signal light can be separately excited, and the generated output light can be isolated from the strong pump light in a separate bus waveguide. The energy cost for data bit conversion using OPWC is also estimated.

Chapter 6 explores the design of optical parametric oscillators (OPO) based on triply-resonant systems, and shows a triple-cavity resonator can be used to realize an efficient OPO by taking

advantage of its unique resonance modes with mode-dependent linewidth. The effects of nonlinear two-photon absorption and free carrier absorption are considered, and expressions of maximum achievable efficiency, oscillation threshold and optimum coupling rates are presented for OPOs built in some example nonlinear materials.

Chapter 2

Coupled-cavity resonator systems for nonlinear optics

This chapter describes the compound mode structures of coupled-cavity resonator systems, with an emphasis on their unique advantages for on-chip nonlinear optical interactions. First, design of the constituent microcavity is described, using microring and photonic crystal cavities as examples. Next, the effects of cavity-bus and cavity-cavity coupling losses on optical nonlinearity is presented, and several low-loss coupler designs are summarized. Finally, the compound modes of coupled-cavity resonator systems are examined in detail, including mode frequency splitting, dispersion engineering and mode-selective coupling.

2.1 Microcavity

In an optical resonator, light of certain wavelengths is enhanced due to constructive interference, while light of other wavelengths is prohibited due to destructive interference. As a result, a resonator has enhanced density of optical states at discrete photon energies, and can be used to build lasers, filters and interferometers. A microcavity usually refers to a dielectric cavity with size smaller than 1 mm, and thus has a larger free spectral range (FSR) compared to macroscopic cavities, which is useful, say, for building a continuous-wave laser with single-mode operation and a pulsed laser with a high repetition rate. In addition, the resonant modes of a microcavity can couple to external bus waveguides with wavelength-dependent coupling rates [21, 22], which, together with loss mechanisms, determines a mode's linewidth. Therefore, the small volume, large FSR and degree of freedom in controlling external coupling, together make a microcavity an ad-

vantageous geometry for building nonlinear optical devices. Even though dispersion in a small microcavity affects the phase matching condition for optical nonlinearity, it can be well controlled in coupled-cavity resonators by engineering their compound modes (see Sec. 2.3).

A microcavity can have travelling-wave resonance modes as in a disk, toroid, and ring cavity, and standing-wave resonance modes in photonic crystal (PhC) cavities of one-, two- and three dimensions, while in the former case a standing-wave field in the coupling waveguide can excite a combination of two degenerate travelling-wave resonance modes. In this section, designs for microring and one-dimensional PhC cavities are summarized.

2.1.1 Microring cavity

A microring cavity, as shown in Fig. 2.1 (a), is basically a waveguide connected in a loop. Its resonant condition is satisfied with a total phase change of multiple 2π in one round-trip propagation, i.e., $\int_0^{2\pi} \gamma d\theta = m \cdot 2\pi$. The integer number, m , is called the longitudinal order. The angular propagation constant, γ , is roughly equal to $\beta\bar{R}$, where β is the linear propagation constant, and \bar{R} is the mean radius of local mode fields. For a perfect circular ring with azimuthal symmetry, γ is equal to m . It should be noted that the intrinsic eigenvalue of a ring mode is not the linear propagation constant, β , but rather the angular propagation constant, γ .

An optimum ring radius should be chosen to maximize the nonlinear effect in a microring cavity. For example, the third-order nonlinear effect scales with the quantity Q^2/V_{eff} , where Q is the cavity quality factor, and V_{eff} is the nonlinear mode volume which is linearly proportional to the ring radius (see Appendix A). In a circular microring cavity, the optical fields shift outwards in the radial direction, resulting in a radiation loss that increases exponentially with its curvature. Such bending loss, together with other linear loss due to material absorption, surface scattering and coupler loss, determines the cavity's intrinsic quality factor. Therefore an optimum radius is chosen that minimize V_{eff} without compromising Q^2 . For a single ring cavity, this design problem is non-trivial because the cavity mode dispersion also varies with the radius (i.e., the difference in FSR usually increases with ring curvature), however, a coupled-ring resonator as shown in Fig. 2.1

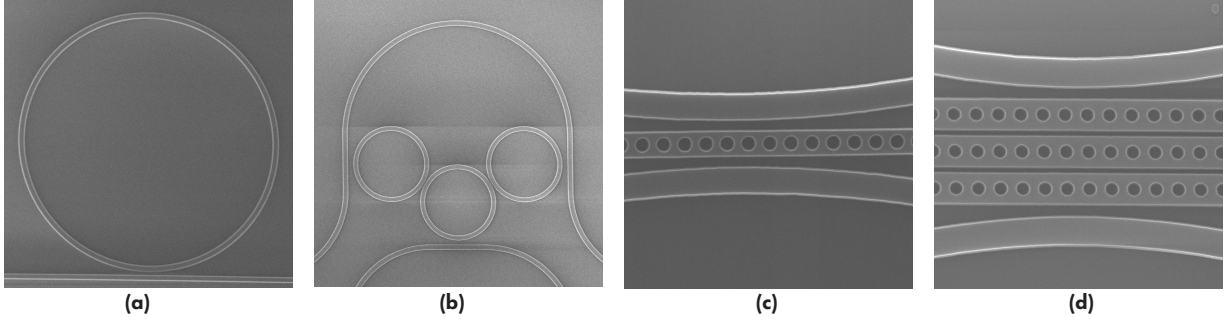


Figure 2.1: SEM pictures of single and triple microring and one-dimensional single and triple photonic crystal cavities designed in the course of this thesis work.

(b) can resolve the problem as shown in Sec. 2.3.

2.1.2 Photonic crystal nanobeam cavity

A photonic crystal (PhC) nanobeam cavity is a standing-wave cavity consisting of quasi-periodic unit cells [23, 8] (see Fig. 2.1 (c)). Its resonant modes are confined by index contrast in the transverse directions and by energy bandgap in the longitudinal direction. The energy bandgap is formed by shifting the band structures of central unit cell relative to those of surrounding unit cells. A one-dimensional (1D) PhC cavity is endowed with a small mode volume since its mode field decays exponentially across unit cells. It can also be designed to have large quality factors by minimizing the spatial Fourier harmonics of the cavity mode inside the lightcone [23]. Since the resonant modes of a 1D PhC cavity extend in a straight nanobeam both along and via evanescent field to the sides of the structure, it can couple efficiently to a straight waveguide or another 1D PhC cavity. With these properties, PhC cavities can be used to build efficient filters despite the fact that they have standing-wave modes which cause difficulties with separating input and through ports without a circulator[24, 25], and can be used for opto-mechanical applications after being suspended [26].

Photonic crystal nanobeam cavities can also be employed to build efficient nonlinear devices. It is difficult to build a triple-resonant single-PhC cavity for four-wave mixing (FWM) since its resonance modes of different longitudinal orders have unevenly-spaced frequencies. Alternatively, a

coupled-PhC resonator where identical PhC cavities are coupled side-by-side (see Fig. 2.1 (d)) can be used to enhance both spontaneous and stimulated four-wave mixing [27], where their compound modes resonantly enhance the signal, pump and idler light.

However, there is a compromise between reducing mode volume and increasing quality factor in 1D PhC cavities. Specifically, when a mode extends over fewer unit cells, it is wider in momentum space, and some spatial frequency components of the mode field cross over into the lightzone. In addition, PhC cavity modes are sensitive to dimensional errors in fabrication and require fine feature sizes that push the compatibilities of lithography.

2.2 Low-loss directional couplers

Directional couplers are ubiquitous within photonic circuits and are used wherever light travels between waveguides or/and cavities. When two waveguides are close to each other, the evanescent field of an optical mode in one waveguide generates a polarization current in the other waveguide, and this polarization current can excite a number of optical modes in itself. The amplitude of each excited mode depends on the overlap between the polarization current and the eigenmode profile. A good coupler is characterized with large coupling rates to desired modes. Couplings to all other modes, whether bounded modes or radiation modes, are effectively optical loss. In fact, it is worse to couple to other bounded modes of the second waveguides as it introduces crosstalk in the optical signal (unless it is appropriately converted back to the desired mode). Coupler loss contributes directly to insertion loss in optical devices (filters, modulators etc.) and should be minimized.

Reducing coupler loss is especially important in designing nonlinear optical devices based on coupled cavities. Unlike optical filters based on coupled cavities where the cavity-cavity coupling is usually weak and coupling-induced frequency splitting is smaller than the linewidth of individual cavity mode (so that a flat top in the filter response is achieved), nonlinear optical devices based on coupled cavities need strong cavity-cavity coupling to enable distinctive compound modes with narrow linewidth than the mode frequency spacing. Thus it is vital to design a coupler with large

ratio of desired coupling versus loss.

The effect of coupler loss on a cavity resonance mode is quantified by a loss-limited quality factor, Q_{CL} . In a microcavity coupled with a bus waveguide, as well as in a dual-cavity resonator, the power loss at the coupler is $l^2 P_o$, and thus $Q_{\text{CL}} = \frac{\omega_o P_o}{l^2 P_o \cdot \text{FSR}} = \frac{\omega_o}{l^2 \cdot \text{FSR}}$, where l^2 is the percentage of power lost at one pass through the coupler.

There are a few guidelines for designing low-loss directional couplers. A general directional coupler consists of two waveguides with arbitrary shapes. The total coupling rate from one mode in one waveguide (m_{1i}) to another mode (m_{2j}) in the other waveguide, depends on the accumulative field in mode m_{2j} excited by distributed polarization current at the second waveguide. Large coupling from mode m_{1i} to mode m_{2j} occurs when the fields in mode m_{2j} excited by the polarization current add up constructively. This is essentially a phase matching requirement, similar to that in nonlinear optical interaction.

For a given coupling rate per distance, it is more advantageous to use a combination of smaller waveguide width and larger gaps in order to achieve larger coupling-to-loss ratio. This can be understood from the compound modes picture of the two coupled waveguides. An optical mode in one waveguide can be approximately represented as a combination of a pair of symmetric and anti-symmetric compound modes of the two-waveguide system. Such approximation is more accurate with a large gap between the two waveguides. Thus optical coupling occurs as an interference effect of the two supermodes with unequal propagation constants. Since coupler loss results from excitation of other compound modes, it is thus desirable to use a larger gap in the directional coupler.

For a given total power coupling to a desired mode, one can use a directional coupler with either a large coupling rate per distance and a small coupler region length, or a small coupling rate per distance and a large coupler region length. The latter design usually has larger coupling-to-loss ratio if the two waveguides have similar propagation constants. This is because phase mismatch between modes of different propagation constants increases with propagation length, resulting in cancelling of coupling to undesired modes. Besides, a weaker coupler means weaker perturbation

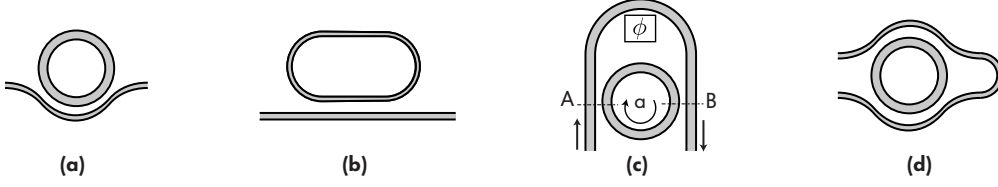


Figure 2.2: Low-loss cavity-bus couplers with: (a) a curved bus with equal curvature as the ring cavity; (b) a straight bus coupled to a straight section of a racetrack cavity; (c) a bus interferometrically coupled to a cavity via two coupling region; and (d) a combination of techniques used in (a) and (c). In all couplers, a combination of large coupler gap and large coupling length is used.

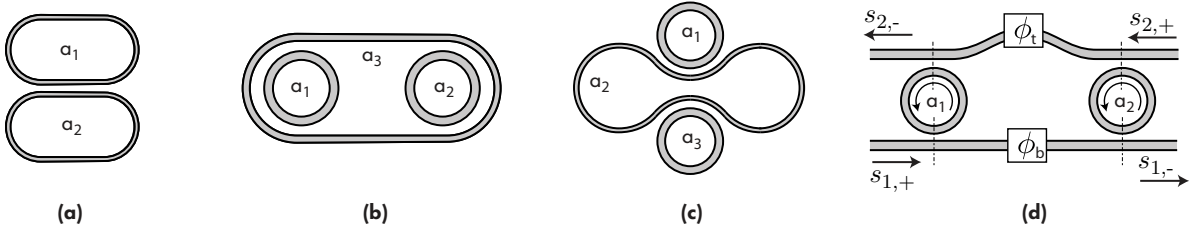


Figure 2.3: Low-loss cavity-cavity couplers with: (a) straight waveguides in the coupling region between two racetrack cavities; (b) curved waveguides with similar curvature at the coupling region between racetrack and ring cavities; (c) curved waveguides with similar curvature at the coupling region between ring cavities, where each individual cavity is accessible by external waveguides; and (d) indirect coupling between two ring cavities via connecting buses taking advantage of low-loss cavity-bus couplers. In all couplers, the ring cavity is designed to have low loss, and a combination of large coupler gap and large coupling length is used.

to the original waveguide mode.

Based on the above design principles, a few geometries that may permit low-loss directional couplers are presented for cavity-bus coupling in Fig. 2.2 and cavity-cavity coupling in Fig. 2.3, respectively.

2.3 Coupled-cavity resonators

This section describes coupled-cavity resonator systems with desired resonance mode structures for applications in nonlinear optics. When individual microcavities, as shown in Sec. 2.1, couple to each other either directly or indirectly, their resonance modes split and form compound resonance modes with distributed energy in each constituent cavity. The compound modes of coupled-cavity resonators are equivalent to molecules' electron states which result from orbital

hybridization of the electron states of their constituent atoms.

The compound states of a coupled-cavity resonator can be engineered for efficient nonlinear interaction by resonantly enhancing interacting light mode excitations with controlled mode dispersion, as well as providing independent control of cavity photon lifetime for each mode. For example in a dual-cavity resonator, the large cavity mode dispersion in a single cavity can be effectively reduced by selectively shifting the resonance frequency of one longitudinal mode upon coupling to a second cavity. The primary and secondary cavities are designed to have unequal free spectral ranges, and therefore the resonance frequencies of other longitudinal modes of the primary cavity are unaffected. As a result, efficient degenerate four-wave mixing can happen in such a coupled-cavity resonator [28].

2.3.1 Triple-cavity resonators

A triple-cavity resonator system is a promising platform for building integrated nonlinear devices based on third-order nonlinearity. Such a resonator consists of three microcavities coupled to each other (see Fig. 2.4(a)). It has three compound modes for each single-cavity mode due to cavity-cavity coupling. The frequency spacings of these three compound modes are determined by the strength of cavity-cavity couplings and differences in resonance frequencies of each constituent cavity. When each individual cavity has equal resonance frequency either by design or active tuning, the three compound modes are evenly spaced in frequency. In addition, they have the same longitudinal order, and thus automatically satisfy the phase matching condition required by degenerate-pump four-wave mixing. Moreover, the linewidth of each compound mode can be separately controlled by independent coupling to external bus waveguides, making triple-cavity resonators a good platform for third-order nonlinear interactions.

In this section we use a travelling-wave triple-ring resonator to explain the above concept in detail. For simplicity, we assume the three microrings are connected in series, and there is no direct optical coupling between the first and the third microrings, otherwise the two travelling-wave modes of opposite propagation directions in each ring would couple to each other and form

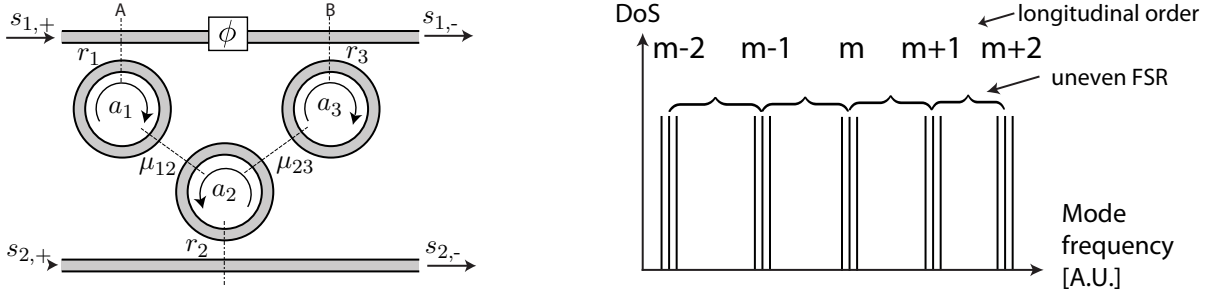


Figure 2.4: (a) Schematic of proposed triple-cavity resonator system. It has three microrings coupled in series and two access bus waveguides. One bus couples to the outer two cavities, and the other bus couples only to the middle cavity; (b) Density of states (DoS) versus frequency (with arbitrary unit) in the proposed triple-cavity resonator. Due to cavity-cavity coupling, there are three supermodes at each longitudinal order.

standing-wave modes. Also, we only consider the case where all three cavities are identical, and the direct cavity-cavity couplings are equal.

2.3.1.1 Dispersion engineering

To study the eigenmodes of a triple-ring resonator, we ignore the bus waveguides in Fig. 2.4(a) for now and treat the triple-ring resonator as a closed system. According to the coupled-mode theory [29], the three individual cavity modes evolve as

$$\frac{d\vec{a}}{dt} = j\overline{\overline{M}} \cdot \vec{a} \quad (2.1)$$

where the mode amplitude \vec{a} and the coupling matrix $\overline{\overline{M}}$ are given by

$$\vec{a} = \begin{bmatrix} a_1 \\ a_2 \\ a_3 \end{bmatrix}, \quad \overline{\overline{M}} = \begin{bmatrix} \omega_0 & \mu_{12} & 0 \\ \mu_{21} & \omega_0 & \mu_{23} \\ 0 & \mu_{32} & \omega_0 \end{bmatrix} \quad (2.2)$$

where a_k , $k \in \{1, 2, 3\}$ is the mode amplitude in each constituent cavity, and $|a_k|^2$ denotes the total energy in cavity k , ω_0 is the resonance frequency of each cavity, and μ_{mn} , $m, n \in \{1, 2, 3\}$ is the cavity-cavity coupling rate set by the geometric gap between adjacent cavities. In a closed system energy is conserved, and thus the coupling matrix $\overline{\overline{M}}$ is Hermitian. Therefore $\mu_{21} = \mu_{12}^*$,

and $\mu_{32} = \mu_{23}^*$. The resonance frequencies and mode profile of the “supermodes” of the triple-cavity resonator are given by the eigenvalues and eigenvector of coupling matrix $\overline{\overline{M}}$, respectively

$$\tilde{\omega}_1 = \omega_0 - \sqrt{2}\mu, \quad \tilde{a}_1 = \left[\frac{1}{2}, \frac{1}{\sqrt{2}}, \frac{1}{2}\right] \cdot \vec{a} \quad (2.3)$$

$$\tilde{\omega}_2 = \omega_0, \quad \tilde{a}_2 = \left[\frac{1}{\sqrt{2}}, 0, -\frac{1}{\sqrt{2}}\right] \cdot \vec{a} \quad (2.4)$$

$$\tilde{\omega}_3 = \omega_0 + \sqrt{2}\mu, \quad \tilde{a}_3 = \left[\frac{1}{2}, -\frac{1}{\sqrt{2}}, \frac{1}{2}\right] \cdot \vec{a} \quad (2.5)$$

where $\mu \equiv |\mu_{12}| = |\mu_{23}|$. The “supermodes” have equal frequency spacings as expected. Therefore when used to enhance signal ($\omega_s = \omega_o - \sqrt{2}\mu$), pump ($\omega_p = \omega_o$) and idler ($\omega_i = \omega_o + \sqrt{2}\mu$) wavelengths in a degenerate FWM process, these three supermodes automatically satisfy both photon energy conservation ($2\omega_p = \omega_s + \omega_i$) and phase matching ($2k_p = k_s + k_i$) conditions. Unlike a single-ring resonator, a triple-ring resonator does not require careful design of waveguide cross section dimensions to minimize dispersion for phase matching — the three supermodes of the same longitudinal order in triple cavities automatically satisfy the phase matching condition as long as the constituent rings are identical and the couplings between rings are small. One benefit of employing the triple-cavity resonator for FWM is that, even if the microring cavity is dispersive and has non-constant FSR, the coupling-induced frequency splitting can be designed to provide equally spaced resonances to enable FWM. As a result, the individual microring cavity can be optimized for parametric gain, without a competing requirement to produce zero dispersion, while the coupling provides the choice of output signal/idler wavelengths. In contrast, in a single-ring microcavity, the choice of wavelengths is directly coupled to the size, as is parametric gain. In other words, minimizing the mode volume for higher gain also requires one to use signal/idler wavelengths that are spaced far apart due to the large FSR. Therefore there is a limit on how small an optical cavity can be made before the dispersion begins to work against the increase in parametric gain. However, since the three compound modes in a triple-cavity resonator have different mode profiles, their effective overlap volume for FWM is four times as large as that of a single microring [1]. This efficiency reduction may serve as a necessary trade off for the additional flexibility in design. Besides, the fact of different resonance mode profiles leads to different effective mode volumes for

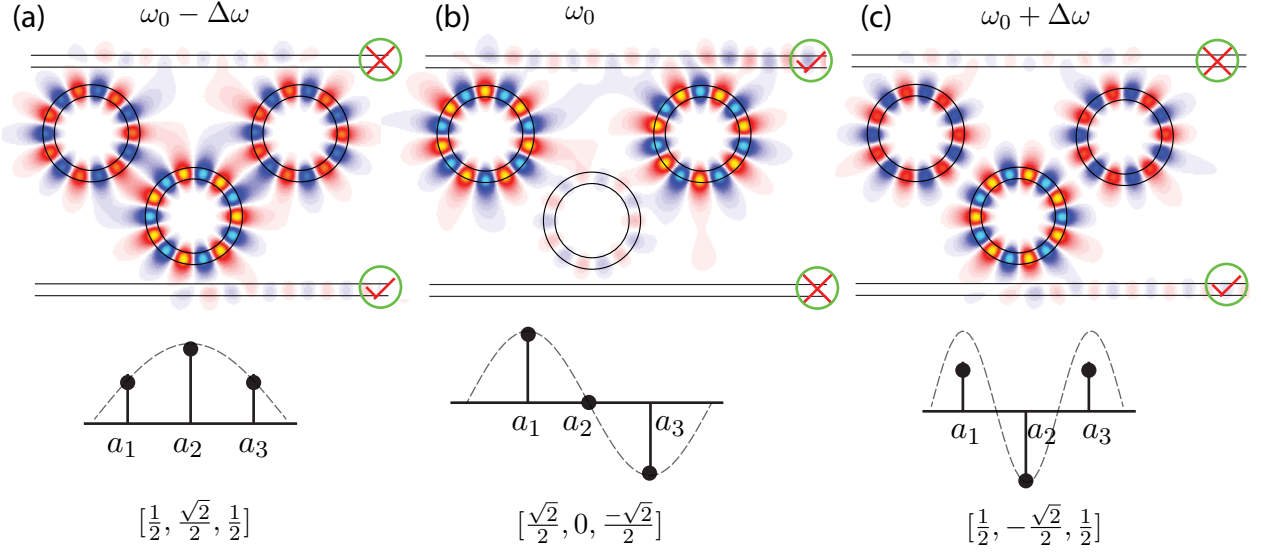


Figure 2.5: Simulated supermode field profile of triple-ring resonator with resonance frequency of: (a) $\omega_0 - \Delta\omega$, (b) ω_0 and (c) $\omega_0 + \Delta\omega$. showing suppressed coupling of signal bus to pump resonance and pump bus to signal/idler resonances.

different set of four waves in third-order nonlinear interaction (see a detailed explanation in the discussion on a generalization of nonlinear figure of merit in Sec. 4.2).

2.3.1.2 Mode-selective coupling

The compound modes of a triple-cavity resonator can also be designed to have different linewidth by independent couplings to external bus waveguides. As solved from the CMT model in the previous section, the field of each supermode is distributed across the cavities [see Fig. 2.5] with field amplitudes in each cavity akin to a discrete version of the (1-, 2- and 3-half-wavelength) wavefunctions of a particle-in-a-box-potential in the three lowest-energy eigenstates.

We next engineer the couplings of two waveguides to the compound resonator to be mode-selective. As Fig. 2.5 shows, the pump resonance has nearly zero energy in the middle cavity, and thus barely couples to the bottom bus which is only coupled to the middle cavity. However, the signal and idler resonances have significant energies in the middle cavity and couple to the bottom bus (which we shall call the “signal bus”). Next, the top bus (we shall call it the “pump bus”)

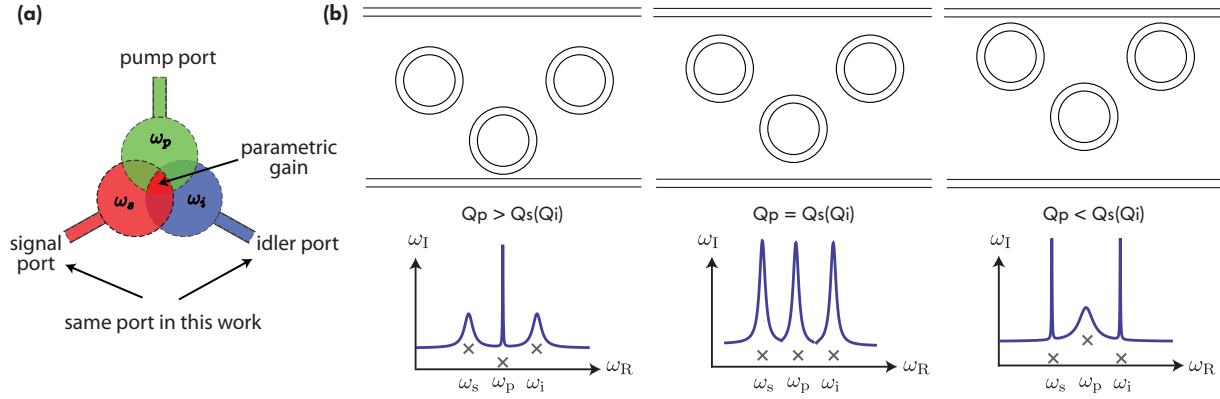


Figure 2.6: (a) Schematic illustrating mode-selective coupling to ports; (b) effect of choices of the “pump bus” and “signal bus” gaps, in the proposed orthogonal supermode linewidth engineering scheme.

couples equally to the two outer cavities via two coupling points (see point A and B in Fig. 2.4(a)). The phase difference of the pump mode field at these two coupling points are shifted by π relative to that of the signal/idler mode ($\Delta\phi_{AB}^p - \Delta\phi_{AB}^{s/i} = \pi$). Then the length of the section of “pump bus” between these two coupling points can be designed so that the “pump bus” couples destructively to the signal and idler resonances, while coupling optimally to the pump resonance. As a result, the external couplings for the pump and signal/idler resonances are entirely isolated to separate waveguides, with a “pump bus” waveguide solely for pump resonance excitation and a “signal bus” waveguide solely for signal/idler resonance coupling. The device in the linear regime is an all-pass filter on each bus – the only source of power transfer from the pump bus to the signal/idler bus is the nonlinear (FWM) coupling. This allows control of geometric gaps to independently control the pump and signal/idler linewidths (see Fig. 2.6(b)), while intrinsically filtering the pump from the signal/idler bus in principle.

Chapter 3

Development of amorphous silicon as an efficient nonlinear material

In order to make efficient integrated nonlinear optical devices, one essential element is still missing, that is, a good nonlinear waveguide material that is compatible in the nanofabrication process. Desired properties of good nonlinear materials include large refractive index (when used as light-guiding material), large nonlinearity, and small linear and nonlinear loss. A large refractive index enables tight confinement of optical energy, thus enhancing optical intensity for large optical nonlinear effects. The combination of large nonlinearity and small loss mitigates the requirement for large on-chip optical power. Most low-cost materials used to fabricate on-chip waveguides, and for which fabrication techniques have been developed that support very low optical propagation losses, have no second-order optical nonlinearity due to centrosymmetry. Thus their lowest optical nonlinearity is third-order nonlinearity, which is often characterized by a nonlinear figure of merit (FOM) defined as $\text{FOM} \equiv \frac{n_2}{\lambda \beta_{\text{TPA}}}$, where λ is the optical wavelength, n_2 is the Kerr coefficient with units of m^2/W and β_{TPA} is the two-photon absorption (TPA) coefficient with units of m/W . A larger FOM means smaller nonlinear absorption for a given nonlinear phase shift.

Common nonlinear materials based on Kerr nonlinearity in integrated optics include crystalline silicon, silicon nitride, chalcogenide glass and amorphous silicon. Although crystalline silicon is a native CMOS process material used in the transistor device layers, and has a large refractive index and Kerr coefficient, it suffers a large nonlinear loss at the telecom wavelength range due to TPA, as well as dispersion and loss due to free carriers generated by TPA. Both silicon nitride and chalcogenide materials have no TPA in the telecom wavelength range, however, they both have

small Kerr coefficients by comparison with silicon. In addition, they both have smaller refractive index contrast and thus require a larger waveguide cross-section to confine optical mode (on the order of $2 \times 1 \mu\text{m}$ for SiN for telecom wavelengths, similar for chalcogenide). As a result, thick films need to be deposited to form waveguides which might suffer from strain-induced film cracking [30]. Larger device size also means smaller integration density on chip. The optical intensity is also reduced due to larger mode area.

Amorphous silicon has large linear index and nonlinear Kerr coefficient, however, it suffers from large optical absorption associated with dangling bonds. Incorporation of hydrogen into amorphous silicon can passivate dangling bonds, and the resulting hydrogenated amorphous silicon (a-Si:H) is one promising nonlinear waveguide material. By engineering its growth conditions, its linear refractive index and Kerr coefficient can both be greater than those of crystalline silicon. Most importantly, it has a quasi-bandgap energy of approximately 1.7 eV, thus it should have negligible two-photon absorption at telecom wavelength around 1550 nm whose photon energy is smaller than half of the bandgap energy of a-Si:H. However, unlike crystalline silicon which has sharp band edges and no electronic states in the bandgap, hydrogenated amorphous silicon has electronic states in its bandgap. These states include Urbach tail states starting from the band edges associated with disorders and defect states deep in the bandgap associated with unsaturated silicon dangling bonds (see Fig. 3.1). In fact, the bandgap of an amorphous material (called “mobility gap”) only separates extended states in the valence and conduction bands. Two-photon absorption in a-Si:H that involves electronic transitions from or/and to local states can still occur, although the probabilities of such transitions are greatly reduced. By optimizing the deposition process TPA in a-Si:H can even be eliminated [31]. Therefore a-Si:H materials usually have values of FOM in the range 0.32–4.9 [32] near 1550 nm by comparison with the range 0.34–0.69 for crystalline silicon [33, 32].

However, one should note that the FOM defined above is related only to the instantaneous nonlinear properties. Although some work observed zero non-instantaneous nonlinear absorption and refraction in a-Si:H samples [32], there have been various reports on the delayed nonlinearity of a-Si:H [31, 34]. Non-instantaneous nonlinearity can significantly impair the performance

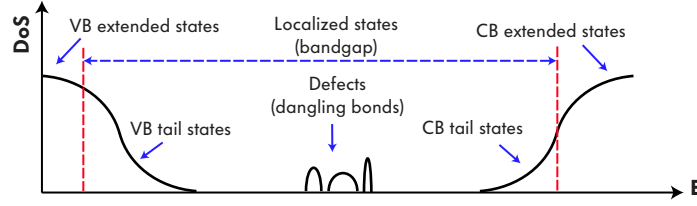


Figure 3.1: A schematic illustration of the electronic density of states in hydrogenated amorphous silicon. VB: valence band; CB: conduction band. The red dashed line denotes the mobility edges.

of a nonlinear device, especially when CW light or high duty cycle, high repetition rate pulsed light is used. However, the findings and interpretations of the non-instantaneous nonlinearity of hydrogenated amorphous silicon vary significantly in the literature [31]. Some studies attributed non-instantaneous nonlinear absorption to free carriers generated by two-photon absorption as in crystalline silicon [35], whereas some studies found no instantaneous two-photon absorption in some wide-bandgap a-Si:H samples [36], and others argued that free carriers could also be generated at an enhanced rate via two-state absorption (TSA) where sequential one-photon absorptions events are facilitated by mid-gap electronic states [34]. In addition, recent pump-probe measurements by Wa-then et.al [31] found in their samples a non-instantaneous absorption rate that scales in proportion to the applied pump power, and a non-instantaneous nonlinear refraction with the same sign as the instantaneous Kerr effect but opposite to the dispersive effect of free carriers, therefore concluding the delayed nonlinearity can be treated as an effective third-order nonlinearity rather than TPA combined with FCA. Nevertheless, it is generally accepted that the nonlinear characteristics of a given sample of a-Si:H depend strongly on the fabrication conditions. Therefore it is important to understand the origin of the delayed nonlinear absorption in a-Si:H, and improve the material fabrication recipe to reduce the nonlinear absorption.

In this chapter, the fabrication of a-Si:H film and characterization of both their linear and nonlinear optical properties are described. The work presented in this chapter was done at Hewlett Packard Laboratories during the course of a summer internship under the supervision of Dr. Jason Pelc..

3.1 Growth of hydrogenated amorphous silicon material

Low-loss hydrogenated amorphous silicon can be deposited using plasma enhanced chemical vapour deposition (PECVD). In the PECVD chamber, a plasma causes the precursor gas silane (SiH_4) to dissociate. The resulting reactive species then react and deposit on a heated substrate. Compared with other deposition methods such as sputtering and evaporation, one main advantage of growing amorphous silicon in PECVD is its low substrate temperature (i.e., can be less than 300°C), which enables back-end-of-line electronic-photonics integration in the standard complementary-metal-oxide-semiconductor (CMOS) fabrication process. Another advantage of a-Si:H growth in PECVD is the introduction of hydrogen atoms dissociated from the precursor gas into the amorphous film [37], because hydrogen plays a few key roles in improving the quality of amorphous silicon film. First, hydrogen can passivate dangling silicon bonds and thus reduce electronic states in the bandgap, which mitigates both linear and nonlinear absorption. Also, the extent of disorder in the amorphous silicon is reduced as hydrogen diffuses into the silicon network to break and remove weak Si-Si bonds, thus lowering the top edge of the valence band formed by those weak Si-Si bonds. As a result, the bandgap of a-Si:H is widened and optical absorption is further reduced. However, inclusion of too many hydrogen atoms in amorphous silicon can introduce extra scattering loss by forming poly-hydride bonds. Thus it is crucial to control both the concentration and diffusion dynamics of hydrogen atoms in the film during growth. The hydrogen quantity and dynamics in a-Si:H is affected by a few growth conditions, such as substrate temperature. At much lower temperatures, the diffusion coefficient of hydrogen in the silicon network is too small to allow structural equilibration, whereas at much higher temperatures, the chemical potential is lower and it is harder for hydrogen to remain in the film.

In summary, both linear and nonlinear optical properties of hydrogenated amorphous silicon depend on its microstructure and dynamics during growth such as the quantity and diffusion speed of incorporated hydrogen, which are controlled by growth conditions in the PECVD chamber. Therefore, it is critical to tune the deposition conditions for the best growth recipe. We investigated

Table 3.1: Growth conditions of a-Si:H in PECVD

Parameter	Range	Nominal setting
Temperature ($^{\circ}\text{C}$)	{250, 300, 350}	250
RF power (W)	{10, 20, 50}	10
Pressure (Torr)	{1.0, 1.5, 1.9}	1.5
Silane flow (sccm)	{10, 20, 25}	20
Helium flow (sccm)	{50, 100, 275, 475}	100

effects of temperature of substrate wafer, power of RF source that excites plasma, flow rates of precursor and dilution gases and chamber pressure on the film quality, and arrived at a recipe for growing a-Si:H with good nonlinear figure of merit. Table 3.1 summarizes the experimental conditions of the deposition process used in our experiments.

Additional benefits of growing a-Si:H in PECVD: It is feasible to deposit multiple layers of a-Si:H sandwiched with silicon oxide using PECVD. When the cladding layer thickness is large, there is little coupling between adjacent amorphous silicon layer, enabling three-dimensional high-density integrated optics platform. On the other hand when the cladding layer thickness is small, one can design multilayer photonic devices; for example, in a two-layer such device comprising a pair of microring resonators [38], strong coupling occurs between microrings on adjacent layers with reduced coupler loss (i.e., radiation loss due to coupling), whereas adjacent microrings on the same layer have comparatively weak coupling for a similar coupling gap but large loss due to short coupling length and propagation constant mismatch. As described in previous sections, strongly coupled microrings can enable efficient nonlinear devices. In addition, by selectively etching away cladding material, micro-structures on one layer can move relative to its adjacent layers, leading to large opto-mechanical coefficients due to strong optical coupling [38].

3.2 Characterization of a-Si:H

We performed a series of characterizations on the hydrogenated amorphous silicon films deposited in PECVD, as shown in the flow chart in Fig. 3.2. First the complex refractive index and thickness of deposited films are measured with a spectroscopic ellipsometer. Then the microstructure of the films are investigated by measuring wavelength-dependent absorption using Fourier transform infrared spectroscopy (FTIR). After these two steps, films with large bandgap (fitted from ellipsometry data) and good microstructure are patterned and etched to form optical waveguides, where material Kerr coefficients are calculated from optical pulse linewidth broadening due to self-phase modulation, and material nonlinear absorption coefficients are derived from transient absorption in pump-probe measurements. In the end the relative magnitudes of Kerr nonlinearity and nonlinear absorption is compared using an effective nonlinear figure of merit.

3.2.1 Linear refractive index, absorption and microstructure

Ellipsometry is a common tool for measuring thin film refractive index and thickness. Because it measures the change of polarization of light upon reflection or transmission from a stack of thin films, it is insensitive to incident light intensity and polarization and thus gives accurate measurement. From the measured film thickness and wavelength-dependent complex refractive index, a Tauc-Lorentz physical model [39] was constructed to fit the bandgap energy of the deposited a-Si:H material. Fig. 3.3 (a) shows measured complex refractive index of an a-Si:H sample. At 1550 nm, a-Si:H has an index of approximately 3.56, greater than that of crystalline silicon. The

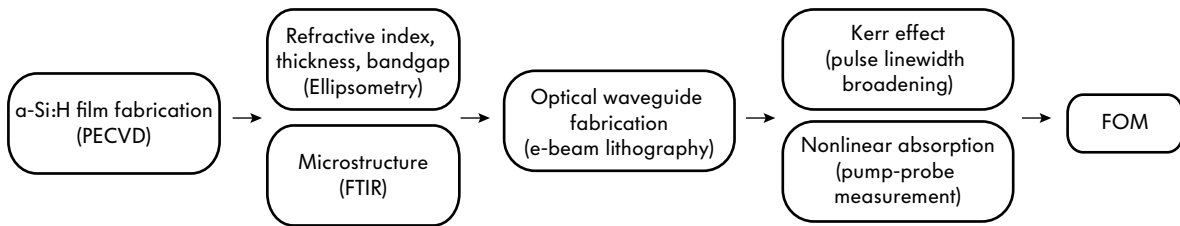


Figure 3.2: Hydrogenated amorphous silicon fabrication and characterization procedure.

extinction coefficient vanishes at approximately 710 nm, consistent with the fitted bandgap energy of 1.69 eV.

Fourier transform infrared spectroscopy is an effective way to study the microstructure of thin films. Atomic bonds have characteristic vibrational and rotational modes which have distinctive resonance frequencies, corresponding to characteristic absorption peaks. For example, Si-H and H-Si-H bonds have stretching vibration modes at 2000 cm^{-1} and 2090 cm^{-1} , respectively. By measuring the relative absorption strength at these two frequencies, the hydrogen content and hydrogen bonding information in the samples can be inferred. In the experiment, the sample is mounted against a germanium prism which has higher refractive index than amorphous silicon. When light passes the germanium prism with a total internal reflection at the interface between Ge and a-Si:H, the evanescent field is partially absorbed by the a-Si:H film, causing a dip in the spectrum of transmitted light at the characteristic frequencies. Fig. 3.3 (b) shows a typical absorption spectrum in a FTIR measurement, where the a-Si:H sample has a much larger absorption at 2000 cm^{-1} due to Si-H bonds than that at 2090 cm^{-1} due to H-Si-H bonds. A frequently used parameter called microstructure R, defined as the relative magnitude of the integrated intensities (I) at the two peaks, $R \equiv \frac{\int I_{2090}}{\int I_{2000} + \int I_{2090}}$, is calculated to be only 0.12. This value is smaller than the typical range of 0.15–0.42 [37], showing that excessive hydrogen in the sample is reduced.

Summary of a-Si:H films properties with varying deposition conditions: first, as the RF power increases, the deposition rate increases as the precursor gas dissociates fast, but the microstructure ratio R increases as a result of large amount of $-\text{SiH}_2$ radicals in the chamber. The substrate temperature affects the kinetics of radicals on the amorphous network, and an optimum temperature around $250\text{ }^\circ\text{C}$ exists. We did not observe a large effect of gas pressure and flow rates in the range of values explored in Table 3.1 on the bandgap and microstructure R of the deposited films, although these parameters have been reported to affect the film qualities[37]. We also find that the film parameters, such as the fitted bandgap energy and microstructure ratio, depend on the film thickness, as reported in [40]. We argue that this dependence comes from the difference in absorption of bulk and surface states in the amorphous silicon films. Finally we arrive at a few

good recipes that lead to a-Si:H films with a combination of large bandgap of approximately 1.7 eV and small microstructure ratio R around 0.1. Their optical refractive indexes are in the range of 3.55–3.59. Then we proceed to fabricate optical devices on these films using e-beam lithography followed by dry etching. In the next section, we study the linear optical loss, Kerr effect and nonlinear absorption in these waveguides, and find out the recipe that gives the best a-Si:H films with the highest nonlinear figure of merit.

3.2.1.1 Linear optical loss

The linear optical loss in an optical waveguide includes loss due to material absorption, field scattering, and radiation. Waveguides of different lengths are laid out on the same chip, and power transmission losses through them at an optical wavelength of 1550 nm are plotted versus their length. Fig. 3.3(c) shows measurement in one sample, where the total linear optical loss in the waveguides is fitted to be approximately 2.1 dB/cm, although the measurement error is not negligible due to large sensitivity of grating coupler efficiency on fiber position. Over all fabricated waveguides, a large range of 2.1–7.5 dB/cm is measured for the linear absorption at 1550 nm.

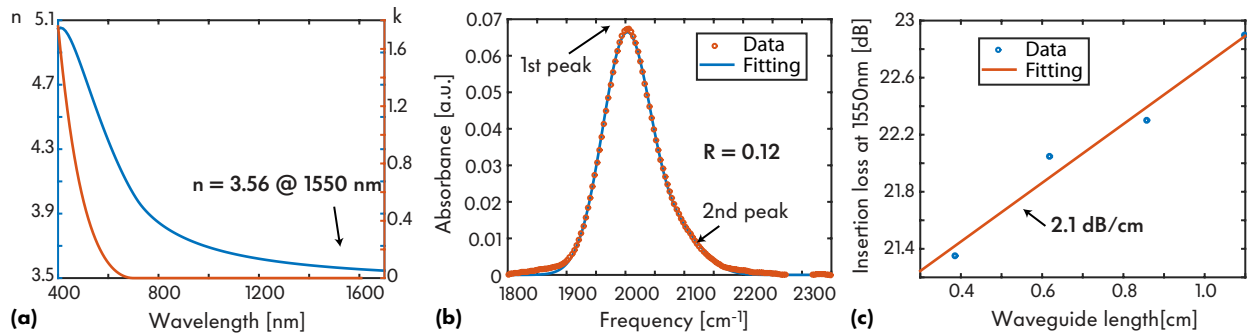


Figure 3.3: Linear optical properties of hydrogenated amorphous silicon (a-Si:H). (a) Real (n) and imaginary (k) parts of the complex refractive index of an a-Si:H film measured by spectral ellipsometry; (b) Absorption spectrum of an a-Si:H film characterized by Fourier transform infrared spectroscopy. The relative absorption strength at different characteristic frequencies reveals the microstructure of a-Si:H films; (c) Linear optical loss versus lengths of a-Si:H waveguides.

3.2.2 Kerr coefficient

In this section the measurement of the Kerr coefficient, n_2 of the deposited a-Si:H is described. Despite the fact that many approaches can be employed to measure n_2 of a nonlinear material, including the most frequently used Z-scan technique [41], four-wave mixing (see Appendix A), and nonlinear interferometry [42], in a micro-scale cross-section waveguide it is convenient to utilize the spectral broadening of an optical pulse associated with self-phase modulation (SPM). Specifically, a short pulse has time-varying intensity. Due to the Kerr effect, the pulse obtains a time-varying nonlinear phase ($\phi(t)$) proportional to the instantaneous intensity. The instantaneous optical frequency is given by $\omega = \frac{d\phi(t)}{dt}$, and thus new optical frequency components are generated. Especially for an ultra short pulse with duration down to a few picoseconds, the optical spectrum broadening due to SPM can be substantial.

According to Agrawal[43], the spectral broadening factor for a Gaussian pulse is

$$\frac{\Delta\omega_{\text{rms}}}{\Delta\omega_0} = \left(1 + \frac{4}{3\sqrt{3}}\phi_{\text{max}}^2\right)^{1/2} \quad (3.1)$$

where $\Delta\omega_0$ and $\Delta\omega_{\text{rms}}$ are the initial and final RMS spectral width of the pulse, and ϕ_{max} is the maximum nonlinear phase change

$$\phi_{\text{max}} = \gamma P_{\text{p0}} L_{\text{eff}}. \quad (3.2)$$

where γ is a nonlinear parameter proportional to n_2 as $\gamma = \frac{\omega n_2}{c A_{\text{eff}}}$ (see Appendix A), P_{p0} is the peak power, and $L_{\text{eff}} \equiv (1 - e^{-\alpha L})/\alpha$ is the effective waveguide length with the effect of optical power decay due to linear absorption included.

We measured the spectrum broadening of Gaussian pulses in optical waveguides using a setup shown in Fig. 3.4. Short optical pulses are generated from a mode-locked laser, and then go through a tunable bandpass filter (TBPF) to obtain the right Gaussian shape and narrow its spectral width. Then an erbium-doped fiber amplifier (EDFA) amplifies the narrowed pump pulse since large optical power is needed to investigate nonlinear optical effects. The actual pulse power is adjusted by a variable attenuator, and the amplified spontaneous emission (ASE) from the EDFA

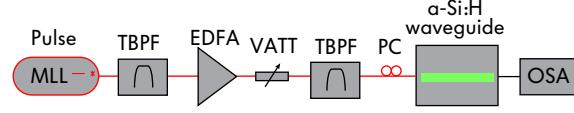


Figure 3.4: Experimental setup for measuring Kerr coefficient based on picosecond pulse linewidth broadening in an a-Si:H waveguide. Abbreviations: MLL, mode-locked laser; TBPF, tunable band-pass filter; EDFA, erbium-doped fiber amplifier; VATT, variable optical attenuator; PC, polarization controller; OSA, optical spectrum analyzer.

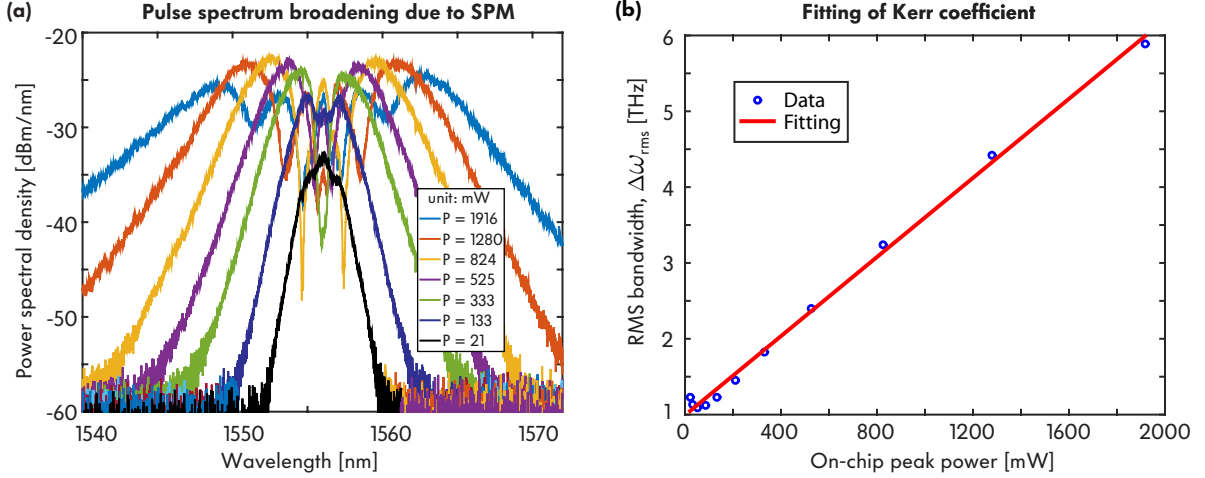


Figure 3.5: Pulse spectrum broadening due to self-phase modulation. (a) Power spectral density at different pulse peak power as measured by OSA; (b) Root-mean-square (RMS) of the angular frequency components of the pulse ($\Delta\omega_{\text{rms}}$) versus on-chip peak power. The slope of the fitted line is proportional to the Kerr coefficient n_2 .

is filtered out by a second TBPF. The light polarization is also adjusted to maximize its coupling to the fundamental transverse electric (TE) mode of the optical waveguides. At this stage, the optical field can be modelled by a Gaussian pulse with time-dependent electrical field amplitude $E_p(t) = \sqrt{P_{p0}} e^{-\frac{t^2}{2\tau_p^2}}$, where τ_p is the pulse duration defined at $1/e$ power radius. The optical pulses are then coupled to the chip via grating couplers. Their spectral linewidth are broaden due to Kerr nonlinearity in the optical waveguides, and then measured by an optical spectrum analyzer (OSA).

Fig. 3.5 (a) shows a typical measured pulse spectrum broadening in an a-Si:H waveguide. As the peak power of the pulse increases, the maximum phase change (ϕ_{max}) due to self-phase modulation also increases, and the pulse spectrum broadens with increased number of peaks as

shown in the OSA spectrum. Fig. 3.5 (b) shows the root-mean-square (RMS) value of the angular frequency components of the pulse ($\Delta\omega_{\text{rms}}$) scales linearly with on-chip peak power of the pulse when ϕ_{max} is much greater than 1, and converges to the initial pulse bandwidth when the peak power is small, matching well with the theoretical formula Eq. 3.1 for a Gaussian pulse. The slope of the fitted line is directly proportional to the value of the material Kerr coefficient n_2 as shown in Eq. 3.1 and Eq. 3.2. The values of τ_p can be derived from the measured pulse spectral width $\Delta\omega_0$ as $\tau_p = \frac{1}{\sqrt{2}\Delta\omega_0}$ by assuming a Fourier transform-limited Gaussian pulse and, together with measured average power (P_{avg}) and pulse repetition rate (r_{rp}), can be used to calculate the peak power as $P_{p0} = \frac{P_{\text{avg}}}{\sqrt{\pi r_{\text{rp}} \tau_p}}$. The mode area A_{eff} is solved using the fundamental TE mode fields. Finally the Kerr coefficient n_2 is calculated to be in the range of $[1.5\text{--}2.5] \cdot 10^{-17} \frac{\text{m}^2}{\text{W}}$ in measured a-Si:H samples.

3.2.3 Nonlinear absorption

Next we study nonlinear absorption in optical waveguides fabricated on the a-Si:H films. As described earlier in this section, there could be instantaneous two-photon absorption, as well as delayed free carrier absorption and two-state absorption in a-Si:H, and their magnitudes depend on the specific material micro structures which are affected by the fabrication conditions. To find out the time-dependent nonlinear absorption in the fabricated samples, we performed pump-probe experiments to measure the transient absorption of a continuous-wave (CW) probe light upon the incidence of a pico-second pump pulse.

Fig. 3.6 shows the experimental setup for measuring the transient absorption in an a-Si:H waveguide. The strong pump pulse is generated by a mode-locked laser and goes through a similar path as that in the experiment for measuring Kerr nonlinearity (see Fig. 3.4). In fact, the pump pulse spectrum broadening can be simultaneously measured while the nonlinear loss rate is characterized in the pump-probe setup. Therefore the measured ratios of Kerr coefficients and nonlinear loss coefficients are independent on the pump power used, leading to higher accuracy in calculating FOM. The CW probe light comes from an external-cavity diode laser, and its wavelength

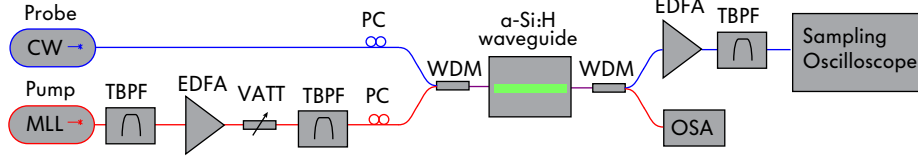


Figure 3.6: Experimental setup for pump-probe measurements of transient nonlinear absorption in an a-Si:H waveguide. Abbreviations: MLL, mode-locked laser; TBPF, tunable band-pass filter; EDFA, erbium-doped fiber amplifier; VATT, variable optical attenuator; PC, polarization controller; WDM, wavelength-division multiplexer; OSA, optical spectrum analyzer. The pump light and probe light travel in different channels of WDM.

is shifted outside of the spectral range of the pump light. The probe light is combined with the pump light via a WDM before being coupled to an optical waveguide through the grating coupler. The polarization of pump and probe light can be separately adjusted to maximize coupling to the fundamental transverse electric (TE) mode of the optical waveguides. After going through various linear and nonlinear optical processes in the waveguide, the transmitted light is coupled out of the chip to a single-mode fiber via an output grating coupler. Another WDM splits the output light again, and the transmitted probe light is amplified by a second EDFA and filtered to clean ASE noise, before it is detected by a fast sampling oscilloscope that is triggered by the pump laser.

A typical transient absorption data is shown in Fig. 3.7(a), where the fractional absorption of the probe normalized to their average value prior to the arrival of the pump (i.e., $1 - P_s(t)/P_s(0)$ where $P_s(t)$ is detected probe power), is plot versus time at a few pump pulse peak power levels. When the pump pulse arrives at approximately $t = 200$ ps, a sudden increase of absorption of the probe light occurs within a few picoseconds (limited by the pump pulse width and oscilloscope bandwidth). Such a large instantaneous absorption is probably due to two-photon absorption. Then the fractional absorption of the probe light undergoes a few oscillations for approximately 200 ps, the reason of which is still unclear. Next the absorption rate decay exponentially with a fitted lifetime of approximately 3 ps. Besides, both the instantaneous and non-instantaneous absorption rate increase with the pump pulse peak power, showing the parametric gain (if any) is weaker than the nonlinear loss. Most importantly, it seems that the delayed absorption scales

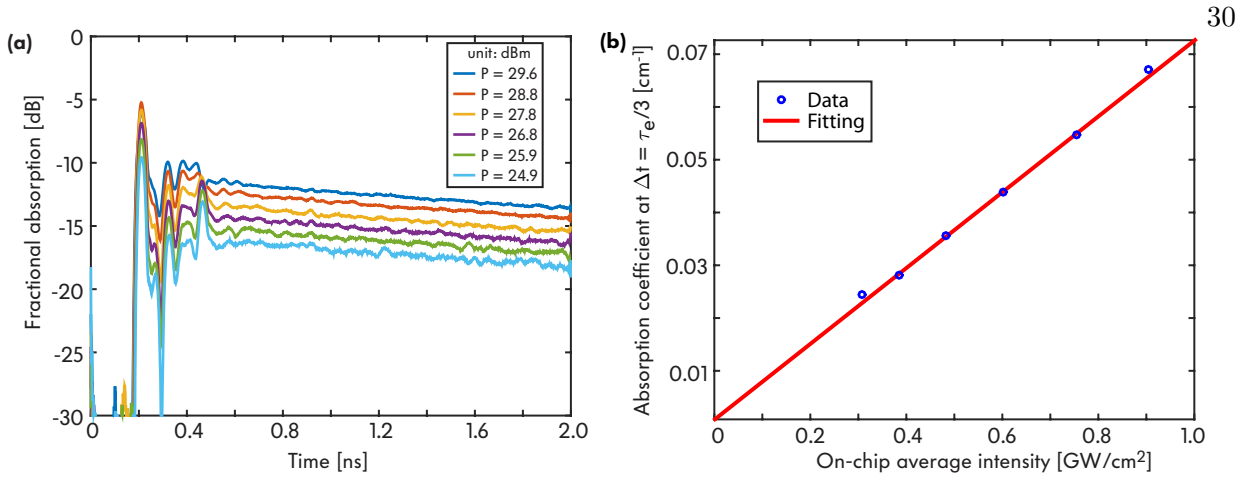


Figure 3.7: Transient absorption of the probe light in the pump-probe experiment. (a) Fractional absorption of the probe light versus time at different pump pulse peak power. The fitted τ_e is about 3.0 ps.; (b) Absorption coefficient at pump-probe delay (Δt) of a third of fitted decay time (τ_e) of the in-gap states, versus pump pulse peak intensity.

linearly with the pump pulse power (see detailed discussion on Fig. 3.7(b) later), demonstrating that the non-instantaneous absorption is not induced by free carriers absorption which scales with the square of pump pulse power.

The linear dependence of delayed absorption of the probe light on the pump pulse power might be explained by a two-state absorption model[34, 31]. Upon incidence of strong pump pulse, many electrons transit from the top of valence band to the mid-gap states by absorbing one pump photon. Electrons in these metastable mid-gap states then act as stronger absorber to the probe light. Due to the large bandgap (i.e., mobility gap) in a-Si:H, electrons fail to absorb enough photon energy to reach extended states in the conduction band, resulting in no free carriers for further absorption. This is in contrast with the original TSA model proposed in [34]. Instead electrons can transition to the localized Urbach tail states in the conduction band, from which electrons can decay back to the metastable mid-gap states and further back to the valence band. Therefore the mid-gap states not only cause linear absorption but also bridge two-state nonlinear absorption. Apparently it's favorable to further improve the a-Si:H film growth conditions to eliminate mid-gap states.

Next, a nonlinear TSA coefficient is described according to the TSA model above. When the

pump pulse travels through the waveguide, the density of in-gap electronic states evolve as

$$\frac{\partial N(\vec{r}, t)}{\partial t} = -\frac{N}{\tau_e} + c_1 \frac{I_p}{v_g} \quad (3.3)$$

where τ_e is the average lifetime of in-gap states, c_1 is the in-gap states generation rate versus optical energy density and I_p is pump light intensity, $I_p = I_{p0} e^{-\alpha_p z - (t-z/v_g)^2/\tau_p^2}$. The decay rate for the pump, α_p includes all linear loss terms. Since the pump pulse lifetime is much shorter than the in-gap electronic states lifetime, i.e., $\tau_p \ll \tau_e$, the equation above can be solved by integrating the generation term first, thus

$$N(\vec{r}, t) = \frac{\sqrt{\pi} c_1 \tau_p I_{p0}}{v_g} e^{-\alpha_p z - \frac{t}{\tau_e}} \quad (3.4)$$

One should note that if a continuous-wave pump is used, the steady-state density of in-gap electronic states is

$$N_{\text{cw}}(\vec{r}) = \frac{c_1 \tau_e I_{\text{p,cw}}}{v_g} e^{-\alpha_p z} \quad (3.5)$$

where τ_e is the lifetime of in-gap states and $I_{\text{p,cw}}$ is the CW pump power. Electrons in the in-gap states then act as absorber for the probe light, and the probe light power, noted as P_s , evolves as

$$\frac{dP_s}{dz} = -\alpha_s P_s - \int^{\text{NL}} c_2 N I_s dx dy \quad (3.6)$$

where α_s is the linear absorption of probe light when the pump light is absent, c_2 is the linear absorption rate of the probe light versus the density of the in-gap electronic states, and the integration is performed over the nonlinear material region. Combining Eq. 3.4 and Eq. 3.6 leads to

$$\frac{dP_s}{dz} = -\left(\alpha_s + \frac{\sqrt{\pi} c_1 c_2 \tau_p I_{p0} e^{-\alpha_p z - \frac{t}{\tau_e}}}{v_g A_{\text{eff}}}\right) P_s \quad (3.7)$$

where the effective area is defined as

$$A_{\text{eff}} = \frac{P_s P_p}{\int^{\text{NL}} I_s I_p dx dy} \quad (3.8)$$

The total power transmission of the probe light in the nonlinear waveguide is given by

$$T_s = e^{-\int_0^L \left(\alpha_s + \frac{\sqrt{\pi} c_1 c_2 \tau_p P_{p0} e^{-\alpha_p z - \frac{t}{\tau_e}}}{v_g A_{\text{eff}}} \right) dz} = e^{-\alpha_s L} e^{-\frac{\sqrt{\pi} c_1 c_2 \tau_p P_{p0} L_{\text{eff,p}}}{v_g A_{\text{eff}}} e^{-\frac{t}{\tau_e}}} \quad (3.9)$$

and the fractional absorption of the probe light due to the pump pulse is

$$\text{FA}(t) = 1 - \frac{T_s}{T_s(P_{p0} = 0)} \approx \frac{\sqrt{\pi} c_1 c_2 \tau_p P_{p0} L_{\text{p,eff}}}{v_g A_{\text{eff}}} e^{-\frac{t}{\tau_e}} \quad (3.10)$$

where $L_{\text{p,eff}} = \frac{1 - e^{-\alpha_p L}}{\alpha_p}$. Notably the nonlinear loss associated with TSA is proportional to the pump pulse energy ($\sqrt{\pi} \tau_p P_{p0}$) rather than its peak power only. This is because the total number of electrons in the in-gap electronic states is dependent on the total pump pulse energy. Similarly, the fractional absorption of the probe light due to a CW pump light can be derived using Eq. 3.5 instead of Eq. 3.4

$$\text{FA} \approx \frac{c_1 c_2 \tau_e P_{\text{cw,p}} L_{\text{p,eff}}}{v_g A_{\text{eff}}} \quad (3.11)$$

An effective TSA coefficient β_{TSA} can be defined by analogy with the two-photon absorption coefficient ($dI/dz = -\alpha I - \beta_{\text{TPA}} I^2$):

$$dI_s/dz = -\alpha_s I_s - 2\beta_{\text{TSA}} I_p I_s \quad (3.12)$$

where $I_p(I_s)$ is the pump (probe) light intensity. Note that there is a factor of 2 before the TSA coefficient β_{TSA} by analogy with cross TPA since the pump and probe are two different light. Thus the fractional absorption of the probe light defined in Eq. 3.10 is also given by

$$\text{FA} \approx 2\beta_{\text{TSA}} \frac{P_p L_{\text{p,eff}}}{A_{\text{eff}}} \quad (3.13)$$

By comparing Eq. 3.10, Eq. 3.11 and Eq. 3.13, the TSA coefficient, β_{TSA} is given by

$$\beta_{\text{TSA}} = \begin{cases} \frac{\text{FA}/L_{\text{p,eff}}}{2P_p/A_{\text{eff}}} = \left(\frac{c_1 c_2 \tau_e}{2v_g} \right) & \text{(CW pump)} \\ \frac{\text{FA}(t=0)/L_{\text{p,eff}}}{2P_{p0}/A_{\text{eff}}} = \left(\frac{c_1 c_2 \tau_e}{2v_g} \right) \cdot \left(\frac{\sqrt{\pi} \tau_p}{\tau_e} \right) & \text{(pulsed pump)} \end{cases} \quad (3.14)$$

Fig. 3.7 (b) shows the fractional absorption rate ($\frac{\text{FA}(t=\tau_e/3)}{L_{\text{p,eff}}}$) at a pump-probe delay of $\tau_e/3$, i.e., a third of the lifetime of in-gap electronic states, versus the on-chip peak intensity of the

pump pulse ($\frac{P_{p0}}{A_{\text{eff}}}$). All data points can be fitted very well with a straight line, proving that the non-instantaneous loss of the probe light is dominant by TSA, rather than free-carrier absorption that scales quadratically with the pump power. The slope of the fitting curve is used to calculate the TSA coefficient β_{TSA} based on Eq. 3.14. For the a-Si:H sample shown in Fig. 3.7, a TSA coefficient of 0.05 cm/GW is obtained for the case of pulsed pump with full-width-half-maximum (FWHM) bandwidth of 0.5 nm. Such a small nonlinear loss demonstrates the potential of employing a-Si:H for nonlinear devices where strong but short optical pulses are used, for example fast optical switching[11]. In addition, because the two-state absorption is proportional to the total pulse energy, the effective TSA coefficient decreases with pulse duration. However, a TSA coefficient of 20 cm/GW is obtained when CW pump light is used. Such a large TSA coefficient puts severe constraints on using it in nonlinear optical devices employing continuous wave light or long pulses with large repetition rates. Because TSA increases with the lifetime and density of states of the in-gap electronic states, it is critical to further improve the fabrication conditions to eliminate unsaturated dangling bonds in a-Si:H.

Photon detector based on TSA: an efficient photon detector can be designed taking advantage of nonlinear TSA in hydrogenated amorphous silicon. By modifying the growth conditions of a-Si:H, electronic states in the bandgap can be intentionally constructed. These mid-gap states can be possibly engineered to be closer to the top of the valence band than to the bottom of the conduction band. An assistant long-wavelength CW pump light is applied, which has enough energy to excite electrons from the valence band to mid-gap states, but not enough energy to excite electrons further up to the conduction band. Therefore the dark current due to pump light is negligible. When short-wavelength signal light is coincident at the detector, it has enough energy to excite electrons from in-gap states up to extended states in the conduction band, resulting in electric current to be amplified and detected. For example, when the bandgap energy is 1.7–1.8 eV, the pump and signal light can be chosen at 1550 nm and 1180 nm, respectively. Since electronic states in amorphous material have no definite momentum due to the absence of long-range periodicity, no phonons are required in the electronic transitions. Therefore the nonlinear two-state absorption

rate in a-Si:H in CW pump mode is larger than that of two-photon absorption in crystalline silicon.

3.2.3.1 Nonlinear figure of merit

In summary, our investigation on hydrogenated amorphous silicon showed that there is substantial non-instantaneous absorption in our samples [44]. Its magnitude scales linearly with the applied pump light power in accordance with [31], which implies that free carriers generated by two-photon absorption are not the main reason of the delayed nonlinear absorption. Instead we argue that an improved model with two-state absorption via metastable intermediate electronic states in the bandgap can explain the observed delayed absorption in a-Si:H. Because TSA involves mid-gap states that are mainly induced by defects in the amorphous material, the TSA in a-Si:H can possibly be reduced by further improving its fabrication conditions to eliminate defects.

Since the delayed two-state absorption involves two photons and thus is effectively a third-order nonlinear effect like two-photon absorption, an equivalent nonlinear figure of merit can be defined as $\text{FOM} = \frac{n_2}{\lambda \beta_{\text{TSA}}}$. For the a-Si:H sample shown in Fig. 3.7, we obtained a nonlinear FOM of approximately 0.05 if CW pump is used, and a FOM of approximately 20 if a pump pulse with 0.5 nm FWHM bandwidth is used. Since the Kerr coefficients and the TSA coefficients are measured simultaneously using the same experiment setup, and only the relative absorption of the probe light is used, any uncertainty in power measurement does not affect the calculation of the nonlinear FOM.

Chapter 4

Theory of coupled-cavity four-wave mixing and a generalized nonlinear figure of merit

4.1 A nonlinear optics model based on coupled-mode theory

The temporal coupled-mode theory (CMT) [45, 29] has been used to describe the dynamics of an optical resonance mode when perturbation to the original cavity is small (quantitatively, the relative change of resonance frequency due to the perturbation is much smaller than 1, i.e., $\delta\omega/\omega \ll 1$). Such perturbations include the existence of a bus waveguide or another cavity next to the original cavity where the resonance mode has decayed exponentially, as well as optical loss due to small absorption in the guiding or/and cladding material or scattering due to waveguide sidewall roughness. The CMT model also applies to nonlinear optical cavity with strong optical field in it, as long as the perturbation introduced by the optical nonlinearity is small, for example, the relative change of refractive index due to Kerr nonlinearity is small, i.e., $\Delta n = n_2 \cdot I \ll n_o$. A lot of nonlinear optical devices work in this weak-nonlinearity regime, especially when continuous-wave light with moderate optical power is used [46].

In this section we describe the equations from CMT model that govern the dynamics of optical modes in a micro-resonator with linear and nonlinear optical processes included, and use them as basis for designing nonlinear devices in coupled-cavity resonators. Specifically, we consider only three resonantly-enhanced modes interacting via third-order nonlinearity, $\overline{\chi}^{(3)}$. This is because most nonlinear material have centrosymmetry and thus no second-order nonlinearity, and third-order effect is therefore the strongest nonlinear optical effect. Also, many optical devices rely on

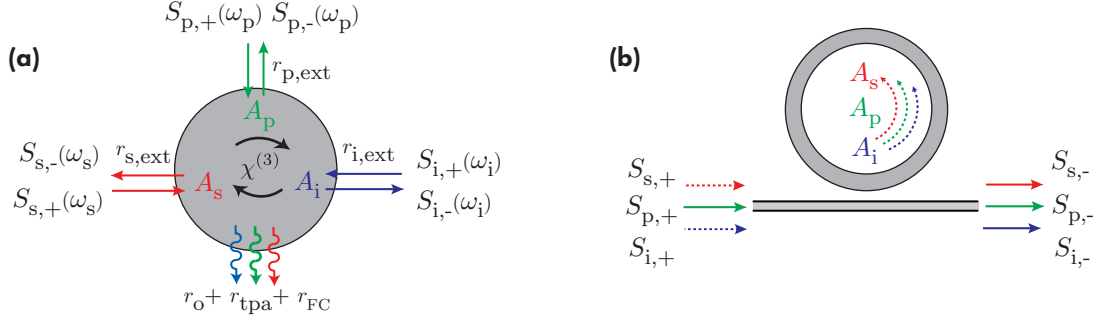


Figure 4.1: (a) Cartoon of a general triply-resonant resonator system with third-order nonlinearity. It has three resonance modes interacting via $\overline{\chi}^{(3)}$ -based effect, including four-wave mixing, cross-phase modulation and cross two-photon absorption. Each resonance mode also couples to an external waveguide mode, represented by an excitation field $S_{k,+}$ ($k \in \{p, s, i\}$) and field decay rate of $r_{k,ext}$ ($k \in \{p, s, i\}$). Besides, all resonance modes decay due to a combination of linear and nonlinear loss; (b) An example triply-resonant resonator system has a microring cavity with three travelling-wave resonance modes and a single bus waveguide coupled to the ring cavity.

four-wave mixing for generating light of new frequencies, where a minimum of three modes (one signal, a degenerate pump and one idler light)¹ are involved. It applies to any resonator with three interacting resonance modes, including but not limit to a single microring cavity with three longitudinal modes and a triple-ring resonator with three supermodes with the same longitudinal order. This three-mode formalism described here can be readily extended to cases such as ultrafast optical switches[11] where only two optical modes are involved, and cases such as optical combs[47] that involve many modes. The model also applies easily to other nonlinear optical processes such as second-order nonlinearity [46] and acousto-optics [48].

For a general three-resonance system illustrated in Fig. 4.1, each resonant mode evolves over

¹ There is some ambiguity on the definitions of signal, pump and idler light in four-wave mixing. In this thesis, signal, pump, and idler light are defined to have the lowest, middle and largest frequency, respectively.

time according to the CMT model as

$$\begin{aligned}
\frac{dA_s}{dt} &= (j\omega_{s0} + j\delta\omega_s - j\omega_s - r_{s,\text{tot}})A_s - j\omega_s\beta_{\text{fwm},s}A_p^2A_i^* - j\sqrt{2r_{s,\text{ext}}}S_{s,+} \\
\frac{dA_p}{dt} &= (j\omega_{p0} + j\delta\omega_p - j\omega_p - r_{p,\text{tot}})A_p - 2j\omega_p\beta_{\text{fwm},p}A_p^*A_sA_i - j\sqrt{2r_{p,\text{ext}}}S_{p,+} \\
\frac{dA_i}{dt} &= (j\omega_{i0} + j\delta\omega_i - j\omega_i - r_{i,\text{tot}})A_i - j\omega_i\beta_{\text{fwm},i}A_p^2A_s^* - j\sqrt{2r_{i,\text{ext}}}S_{i,+} \\
S_{k,-} &= S_{k,+} - j\sqrt{2r_{k,\text{ext}}}A_k, \quad (k \in \{s, p, i\}).
\end{aligned} \tag{4.1}$$

where $A_k(t)$, $k \in \{s, p, i\}$, are the cavity energy-amplitude envelopes for light at signal, pump and idler frequencies; $S_{k,+}$ ($S_{k,-}$) is the power-amplitude envelope in the input (output) port for each resonant mode. By “envelope”, we mean that $A_k(t)$ is related to the usual CMT amplitude [29] $a_k(t)$ by $a_k(t) \equiv A_k(t)e^{j\omega_k t}$. For simplicity, we normalize mode field patterns to unity energy or power, such that $|A_k|^2$ is the energy of resonant mode k and $|S_{k,+}|^2$ ($|S_{k,-}|^2$) is the inbound (outbound) power in guided mode k .

Next, ω_{k0} are the “cold-cavity” resonance frequencies when no light is present in the cavity; $\delta\omega_{k0}$ are the resonance frequency shift due to self- and cross- phase modulation from third-order nonlinearity; ω_k are the angular frequencies of the interacting modes, and they are determined from the input light frequencies and energy conservation condition $\omega_s + \omega_i = 2\omega_p$. The field enhancement in the cavity, thus the nonlinear effect, is maximized when all three light (signal, pump and idler) are resonant, that is,

$$\omega_k = \omega_{k0} + \delta\omega_k, \quad (k \in \{s, p, i\}). \tag{4.2}$$

One should note that the nonlinear frequency shift $\delta\omega_k$ is power-dependent

$$\begin{aligned}
\delta\omega_s &= -\omega_{s0}(\beta_{\text{pm},ss}|A_s|^2 + 2\beta_{\text{pm},sp}|A_p|^2 + 2\beta_{\text{pm},si}|A_i|^2) + \delta\omega_{s,\text{FC}} \\
\delta\omega_p &= -\omega_{p0}(2\beta_{\text{pm},ps}|A_s|^2 + \beta_{\text{pm},pp}|A_p|^2 + 2\beta_{\text{pm},pi}|A_i|^2) + \delta\omega_{p,\text{FC}} \\
\delta\omega_i &= -\omega_{i0}(2\beta_{\text{pm},is}|A_s|^2 + 2\beta_{\text{pm},ip}|A_p|^2 + \beta_{\text{pm},ii}|A_i|^2) + \delta\omega_{i,\text{FC}}
\end{aligned} \tag{4.3}$$

where $\beta_{\text{pm},mn}$, $(m, n) \in \{s, p, i\}$ are phase modulation coefficients (see Appendix A.1), $\delta\omega_{k,\text{FC}}$, $k \in \{s, p, i\}$ are resonance frequency blue shift due to free carrier dispersion. In general, the

frequency shift of the three light are different. For example, when the pump light is dominant, $\delta\omega_s$ and $\delta\omega_i$ are twice as large as $\delta\omega_p$ because of the factor of two between cross phase modulation and self phase modulation coefficients. In cases when the in-cavity light energy is small and thus $\delta\omega_k$ is negligible, the resonant condition Eq. 4.2 demands the frequency mismatch (defined as $\Delta\omega_o = \omega_{so} + \omega_{io} - 2\omega_{po}$) to be 0. However, this is generally not true for a cavity with dispersion. Various dispersion engineering methods have been used to bring down $\Delta\omega_o$, including engineering waveguide cross section dimensions to find optimal spots with close-to-zero group velocity dispersion [15], alternatively optimizing waveguide cross section dimensions to reduce resonance frequency mismatch across discrete resonant modes in a microcavity and allow for all-order dispersions [49], and cavity resonance frequency splitting based on mode-selective coupling to an assistant cavity [28]. Notably, the triple coupled cavity resonator proposed in Chapter 2 automatically have reduced $\Delta\omega_o$ induced by cavity dispersion (see Sec. 2.3.1.1 for more details).

$\beta_{\text{fwm},k}$ are the four-wave mixing coefficients (see Appendix A.1). From Eqs. 4.1 one can derive the energy conservation law $2\omega_p\beta_{\text{fwm},p}^* = \omega_s\beta_{\text{fwm},s} + \omega_i\beta_{\text{fwm},i}$. As discussed in Appendix A.1, the coefficients $\beta_{\text{fwm},s}$, $\beta_{\text{fwm},p}^*$, and $\beta_{\text{fwm},i}$ are identical except for the tensor element of $\overline{\chi}^{(3)}$ that they contain. Under the assumption of full permutation symmetry [50], these tensor elements and hence the foregoing coefficients, are equal. Thus we define a single β_{fwm} as

$$\beta_{\text{fwm},s} = \beta_{\text{fwm},p}^* = \beta_{\text{fwm},i} \equiv \beta_{\text{fwm}}. \quad (4.4)$$

Decay rate $r_{k,\text{tot}}$ is the total energy amplitude decay rate for mode k (due to both loss and coupling to external ports), where [51]

$$\begin{aligned} r_{s,\text{tot}} &= r_{s,o} + r_{s,\text{ext}} + r_{\text{FC}} + \omega_{so} (\beta_{\text{tpa},ss}|A_s|^2 + 2\beta_{\text{tpa},sp}|A_p|^2 + 2\beta_{\text{tpa},si}|A_i|^2) \\ r_{p,\text{tot}} &= r_{p,o} + r_{p,\text{ext}} + r_{\text{FC}} + \omega_{po} (2\beta_{\text{tpa},sp}|A_s|^2 + \beta_{\text{tpa},pp}|A_p|^2 + 2\beta_{\text{tpa},ip}|A_i|^2) \\ r_{i,\text{tot}} &= r_{i,o} + r_{i,\text{ext}} + r_{\text{FC}} + \omega_{io} (2\beta_{\text{tpa},si}|A_s|^2 + 2\beta_{\text{tpa},ip}|A_p|^2 + \beta_{\text{tpa},ii}|A_i|^2). \end{aligned} \quad (4.5)$$

Here, $r_{k,o}$, $k \in \{s, p, i\}$ is the linear loss rate of mode k due to linear absorption, scattering and radiation, $r_{k,\text{ext}}$ is the coupling rate to an external port (e.g. waveguide, see Fig. 4.1) and $\beta_{\text{tpa},mn}$

is the two-photon absorption coefficient due to absorption of a photon each from modes m and n ($m, n \in \{s, p, i\}$). $\beta_{\text{tpa},mn}$ should not be confused with the coefficient β_{TPA} typically used in the nonlinear optics literature, which is a bulk (plane wave) value, is defined through $dI/dz = -\beta_{\text{TPA}}I^2$ and represents ‘nonlinear loss’ per unit length; $\beta_{\text{tpa},mn}$ here has units of ‘nonlinear loss’ per unit time (for a resonant mode), and includes a spatial mode overlap integral (similar to $\beta_{\text{pm},mn}$ and $\beta_{\text{fwm},k}$) to account for the spatial inhomogeneity of the field and lump it into a single effective factor (defined in Appendix A.1). Note that three photon absorption is not included in the CMT model since it is usually negligible in many materials.

Finally, the decay rate includes a contribution due to free-carrier absorption (FCA). The FCA loss rate, r_{FC} , is not a constant like the other rates and coefficients $r_{k,o}$, $r_{k,\text{ext}}$ and $\beta_{\text{tpa},mn}$ in Eq. (4.5), but depends on intensities. It is important in cavities with nonlinear loss such as silicon-core resonators, and is given by (see Appendix A.5)

$$r_{\text{FC}} = \frac{\tau_{\text{FC}}\sigma_a v_g}{2\hbar V_{\text{eff}}} (\beta_{\text{tpa},ss}|A_s|^4 + \beta_{\text{tpa},pp}|A_p|^4 + \beta_{\text{tpa},ii}|A_i|^4 + 4\beta_{\text{tpa},sp}|A_s|^2|A_p|^2 + 4\beta_{\text{tpa},ip}|A_i|^2|A_p|^2 + 4\beta_{\text{tpa},si}|A_s|^2|A_i|^2) \quad (4.6)$$

where τ_{FC} is the free carrier lifetime, σ_a is the free carrier absorption cross section area per electron-hole pair, and v_g is group velocity. V_{eff} is an effective volume of the resonant mode, as defined in Appendix A.1.

Without loss of generality, we have assumed that there is only one S_- (output) and one S_+ (input) port in the system in Fig. 4.1, and the above $S_{k,\pm}$ are respective parts of the spectrum of S_{\pm} . We are making the approximation, relevant to four-wave mixing analysis, that the wavelength spacing of the pump, signal and idler resonances is larger than their linewidth, and that we have continuous-wave (CW) operation or nearly so, so that e.g. the signal input wave, $S_{s,+}$, affects only the signal resonance, and does not excite the other two directly, etc. Then, the three spectral components can be treated as separate ports. In the general case, there could be multiple ports coupled to each resonance mode, and a coupling matrix would replace $-j\sqrt{2r_{k,\text{ext}}}$ in Eqs. 4.1.

4.2 Cavity mode topology and effective nonlinear figure of merit

As Sec. 4.1 shows, the third-order nonlinear interaction coefficients in a microcavity ($\beta_{\text{pm,mn}}$, $\beta_{\text{tpa,mn}}$ and $\beta_{\text{fwm,k}}$ defined in Eqs. 4.1) all depend on the $\overline{\overline{\chi}}^{(3)}$ tensor and modal field overlap (see Appendix A.1). In general, the resonance modes interacting in four-wave mixing can have very different intensity distribution in the cavity, and the overlap of four interacting waves varies from one set to another. Besides, the signal, pump and idler resonance modes can have different polarizations, leading to different contributions in the nonlinear interaction coefficients by various tensor elements of $\overline{\overline{\chi}}^{(3)}$. As a result, there are usually 6 different nonlinear phase modulation coefficients $\beta_{\text{tpa,mn}}$ and 6 different two-photon absorption coefficients $\beta_{\text{tpa,mn}}$ (e.g. absorption of two pump photons differs with absorption of a signal and an idler photon), and the relative magnitudes of the four-wave mixing and two-photon absorption coefficients, can no longer be sufficiently represented by the single conventional material nonlinear figure of merit (defined as $\text{NFOM} = \frac{n_2}{\lambda\beta_{\text{TPA}}} = \frac{\Re[\overline{\overline{\chi}}^{(3)}]}{4\pi\Im[\overline{\overline{\chi}}^{(3)}_s]}$) that works well for plane wave nonlinear interaction in bulk materials. Instead, a vector of coefficients is required to characterize the third-order nonlinearity in a microcavity. We call this effect as “cavity mode topology”, and it calls for a generalization of the concept of material NFOM to a mode-dependent NFOM **vector** as a metric for performance in integrated nonlinear photonic systems. Using the generalized NFOM, we compare single cavity to multicavity geometries, as well as traveling wave to standing wave mode excitation. The latter are both possible excitations in a traveling wave cavity like a microring resonator, while only standing wave excitation is possible in a standing-wave single-mode cavity like a photonic crystal microcavity. It should also be noted that when both waveguide core and cladding materials have comparable nonlinearity, even if all interacting modes have similar field profile, the effective nonlinear FOM in a micro waveguide or micro cavity, is still an averaged material NFOM weighted by field energy in all nonlinear materials. In this section, we assume a dominant nonlinear material in the micro waveguide, and focus on the dependence of NFOM vector on the cavity mode topology.

First we take a look at the most common case of a microring cavity with travelling-wave

excitations. The resonance mode has uniform intensity along the cavity length, and its field in the cavity can be represented by $\mathbf{E} = A\mathbf{e}_0(\omega, x, y)e^{-j(\gamma\theta - \omega t)}$, which consists of field amplitude A , transverse waveguide mode $\mathbf{e}_0(\omega, x, y)$ and longitudinal and temporal dependence $e^{-j(\gamma\theta - \omega t)}$. We assume the interacting waves have small differences in frequencies ($\omega_p \approx \omega_s \approx \omega_i$) and similar transverse waveguide confinement. Thus the difference in $\mathbf{e}_0(\omega, x, y)$ between the signal, pump and idler can be neglected. The remaining part in the mode field, $e^{-j(\gamma\theta - \omega t)}$, differs in ω and angular propagation constant γ . However, the product of any 4 such factors of fields that come out of the set of signal, pump and idler fields and interact via $\overline{\chi}^{(3)}$, with the energy conservation ($\omega_1 + \omega_2 = \omega_3 + \omega_4$) and phase matching ($\gamma_1 + \gamma_2 = \gamma_3 + \gamma_4$) conditions satisfied, unanimously reduces to 1

$$e^{-j(\gamma_1\theta - \omega_1 t)} \cdot e^{-j(\gamma_2\theta - \omega_2 t)} \cdot e^{j(\gamma_3\theta - \omega_3 t)} \cdot e^{j(\gamma_4\theta - \omega_4 t)} = 1 \quad (4.7)$$

for $\mathbf{E}_k \in \{\mathbf{E}_s, \mathbf{E}_p, \mathbf{E}_i\}$, $k \in \{1, 2, 3, 4\}$. As a result, all third-order nonlinear interaction coefficients ($\beta_{\text{pm, mn}}$, $\beta_{\text{tpa, mn}}$ and $\beta_{\text{fwm, k}}$ have the same overlap integral (see Appendix A.1). All 6 two-photon absorption coefficients ($\beta_{\text{tpa, mn}}$) and all 6 phase modulation coefficients ($\beta_{\text{pm, mn}}$) converge to the same value, respectively. Furthermore, they all have fixed relative magnitudes compared to the four-wave mixing coefficient (β_{fwm}) independent on the actual mode profile

$$\frac{\beta_{\text{tpa}}}{\beta_{\text{fwm}}} = \frac{\Im[\chi_{\text{eff}}^{(3)}]}{|\chi_{\text{eff}}^{(3)}|} \quad (4.8)$$

$$\frac{\beta_{\text{pm}}}{\beta_{\text{fwm}}} = \frac{\Re[\chi_{\text{eff}}^{(3)}]}{|\chi_{\text{eff}}^{(3)}|} \quad (4.9)$$

$$\frac{\beta_{\text{pm}}}{\beta_{\text{tpa}}} = \frac{\Re[\chi_{\text{eff}}^{(3)}]}{\Im[\chi_{\text{eff}}^{(3)}]} = 4\pi(\text{FOM}) \quad (4.10)$$

where $\chi_{\text{eff}}^{(3)}$ takes into account of the polarization effect. Note that the integrated nonlinear FOM in a microring cavity with traveling-wave mode is unchanged from the conventional bulk material value, because all nonlinear coefficients have the same dependence on mode field overlap.

For devices based on nonlinear phase modulation such as nonlinear optical switching, it is convenient to use the conventional nonlinear FOM. However, in the context of nonlinear four-wave

Table 4.1: Third-order nonlinear properties of some common on-chip nonlinear material

Material	$\lambda(\mu\text{m})$	$n_2(10^{-5}\frac{\text{cm}^2}{\text{GW}})^a$	$\beta_{\text{TPA}}(\frac{\text{cm}}{\text{GW}})^a$	NFOM	σ_3
c-Si	1.55 [33]	2.41	0.48	0.34	0.23
c-Si	2.3 [33]	1.0	≈ 0	∞	≈ 0
a-Si:H	1.55 [35]	16.6 ^b	0.49 ^b	2.2	0.036
Si ₃ N ₄	1.55 [52]	0.24	≈ 0	∞	≈ 0

^a The Kerr coefficient n_2 and TPA coefficient β_{TPA} are related to the third-order susceptibilities of the nonlinear material $\bar{\chi}^{(3)}$ (see [53]): $\frac{\omega}{c}n_2 + \frac{i}{2}\beta_{\text{TPA}} = \frac{3\omega}{4\epsilon_0 c^2 n_{\text{nl}}^2} \bar{\chi}_{1111}^{(3)}$.

^b For amorphous silicon (a-Si:H), n_2 and β_{TPA} are calculated from [35]. $\beta_{\text{TPA}} = 2A_{\text{eff}}\gamma_I$, $n_2 = A_{\text{eff}}\gamma_R/k_0$, where A_{eff} is mode overlap area, and the nonlinearity parameter in waveguide $\gamma = 770 - j28W^{-1}m^{-1}$.

mixing, we find it easier to work with a different nonlinear loss parameter, σ_3 , that represents the relative magnitudes of four-wave mixing and two-photon absorption. We call σ_3 the **nonlinear loss sine** (drawing analogy to the linear loss tangent in electromagnetics) and define it as

$$\sigma_3 \equiv \frac{\Im[\chi_{\text{eff}}^{(3)}]}{|\chi_{\text{eff}}^{(3)}|} \quad (4.11)$$

We note that σ_3 depends only on material parameters and is inversely related to the conventional FOM by $\text{FOM} = \sqrt{1 - \sigma_3^2}/(4\pi\sigma_3)$, and β_{tpa} is related to β_{fwm} by

$$\beta_{\text{tpa}} = \sigma_3\beta_{\text{fwm}} \quad (4.12)$$

In Table 4.1, we show third-order optical nonlinearity parameters for some nonlinear materials commonly used in integrated photonics.

Next, we discuss the effective nonlinear FOM in a general cavity where the signal, pump and idler resonance have different field profiles, and introduce a \vec{d} -vector to describe the topological mode structure aspects that give rise to differences in, say, the six TPA coefficients. The material NFOM together with the vector \vec{d} can then be thought of as a generalized NFOM in integrated nonlinear devices. To be specific, we generalize the relationship between two-photon absorption

and four-wave mixing coefficients from Eq. 4.12 to

$$\beta_{\text{tpa},mn} = d_{mn}\sigma_3\beta_{\text{fwm}} \quad (4.13)$$

where $m, n \in \{s, p, i\}$. The nonlinear loss sine σ_3 depends only on material parameters, and the topological \vec{d} -vector accounts for mode overlap. Different nonlinear resonators based on the same nonlinear material could have different effective nonlinearity due to their difference in \vec{d} . As an example, in Fig. 4.2 we show resonators consisting of a single ring cavity or triple coupled ring cavities, each with either traveling-wave mode or standing-wave mode excitation. The three resonance modes interacting via $\bar{\chi}^{(3)}$ in these resonators are shown in Fig. 4.3 accordingly. Fig. 4.4 shows different parametric gain due to FWM and loss due to TPA in these resonators. While all three resonance modes with different longitudinal orders in a travelling-wave microring resonator have azimuthally uniform field intensity, their counterparts in a standing-wave microring resonator have nonuniform intensity and offset peaks and valleys. Therefore a standing-wave mode has larger overlap with itself and with other modes, leading to larger d_{ii} than d_{ij} ($i \neq j$). Also, a triple-cavity microresonator has distributed modes with non-equal energies in each constituent cavity. It turns out that, for example, the ratio of signal-idler TPA to parametric gain (i.e. $\sigma_3 d_{\text{si}}$) is larger in a triple-ring resonator than in a single-ring resonator, with a traveling-wave mode excitation. This means that the effective figure of merit of the triple-ring resonator is smaller than that of the single-ring cavity. A complete summary of various FWM coefficients and \vec{d} -vectors is shown in Table 4.2 and detailed calculations are given in Sec. A.4.

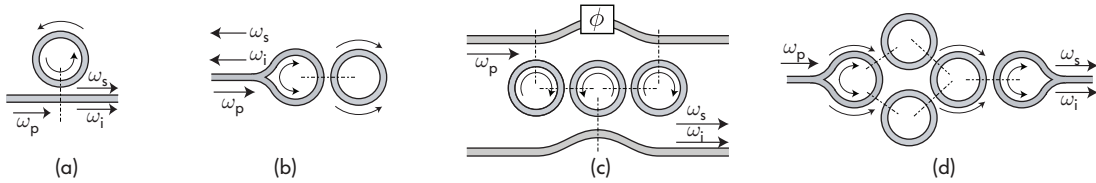


Figure 4.2: Example microring cavity topology for illustration of effective figure of merit: (a) single-ring cavity with traveling-wave mode; (b) single-ring cavity with standing-wave mode; (c) triple-ring cavity with traveling-wave mode; (d) triple-ring cavity with standing-wave mode.

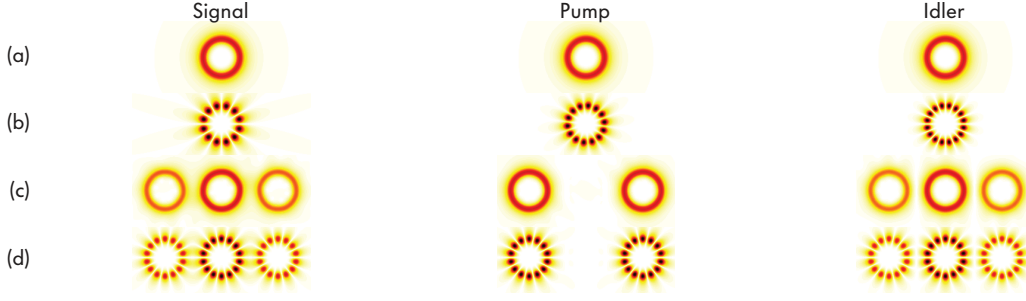


Figure 4.3: Mode fields of the pump, signal and idler resonances for the configurations (a)–(d) in Fig. 4.2 (color-coded intensity scales are different in single and triple-cavity cases in order to show the mode features clearly).

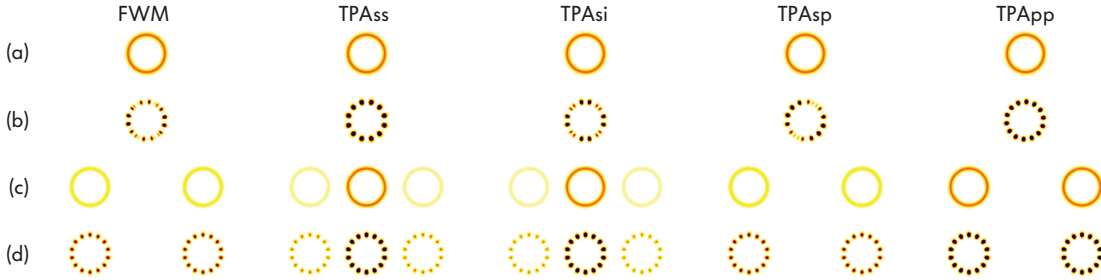


Figure 4.4: Mode overlap integrand for the FWM and various TPA coefficients for configurations (a)–(d) in Fig. 4.2. It shows that a vector of FOM is needed to account for the ratio of FWM relative to various TPA terms. Besides, different cavity topologies have different FOM (see Table 4.2).

An important conclusion from the study on effective nonlinear FOM is that the resonator mode **envelope** matters, i.e. the distribution of the field across parts of the compound resonator, as well as standing-wave vs. traveling-wave excitation. Specifically, standing-wave excitation is very “efficient” for self-TPA loss terms, such as absorption of two signal photons or two pump photons. On the other hand, because of differences in longitudinal mode order, the parametric gain is a bit suppressed. Thus, standing wave excitation in general loses to traveling-wave excitation in the presence of TPA. Likewise, the single-ring configuration is more efficient than triple ring with traveling-wave excitation. However, with standing-wave excitation, the single-ring resonator has a larger FWM coefficient but at the same time larger TPA loss (\vec{d} coefficients). It should be kept in

Table 4.2: Comparison of FWM and TPA coefficients in various cavity topologies

Cavity Type ^a	$\frac{\beta_{\text{fwm}}}{\beta_{\text{fwm}}(\text{1-ring, TW})}$ ^b	d_{ss}	d_{ii}	d_{pp}	d_{sp}	d_{ip}	d_{si}
1-ring (TW ^c)	1	1	1	1	1	1	1
3-ring (TW ^c)	$\frac{1}{4}$	$\frac{3}{2}$	$\frac{3}{2}$	2	1	1	$\frac{3}{2}$
1-ring (SW ^c)	$\frac{1}{2}$	3	3	3	2	2	2
3-ring (SW ^c)	$\frac{3}{8}$	$\frac{3}{2}$	$\frac{3}{2}$	2	1	1	$\frac{3}{2}$

^a Each constituent ring of the triple-ring cavity is identical to the single-ring cavity.

^b Four wave mixing coefficients are normalized to that of a single-ring cavity with traveling-wave modes.

^c TW: traveling-wave, SW: standing-wave.

mind that this comparison is for microring cavities with equal sizes. The triple ring design may be able to use much smaller ring cavities than a single ring design, however, as it is not limited by dispersion. Therefore, either a single-ring or a triple-ring cavity might be more efficient, depending on specific implementation and target wavelengths.

Chapter 5

Optical parametric wavelength conversion

This chapter describes both theoretical and experimental studies on optical parametric wavelength conversion (OPWC) based on degenerate four-wave mixing (FWM) in triply-resonant cavities. Efficient parametric wavelength conversion occurs with stimulated FWM, where two pump photons are converted to a pair of signal and idler photons under the excitation of a seeding signal light. The generated signal and idler light further act as seeding light, leading to enhanced wavelength conversion efficiency. Parametric wavelength conversion facilitates many useful on-chip optical functionalities. First, since parametric optical processes do not rely on atomic transitions, the OPWC is broadband and can be used to generate coherent light at wavelengths where conventional laser gain media are underdeveloped. For example, with the assistance of well-developed semiconductor lasers at wavelengths in the visible and telecom bands, OPWC enables on-chip light sources of wavelength at mid-IR where many interesting gas absorption lines exist [10]. Besides, OPWC increases the number of oscillating lines in optical frequency comb generation by allowing the interaction of any set of four lines with frequency and momentum matching [16, 17]. In fact, OPWC is the main process in an optical parametric oscillator once significant seeding light is generated. In addition, OPWC provides direct gain for all-optical data stream wavelength conversion and amplification in optical communication [14]. Furthermore, an optical parametric amplifier is essentially an OPWC device with large parametric gain, and thus the study on OPWC can shed light on the design of optical parametric amplifiers. Last but not least, a quantum device with spontaneous FWM can be understood as a classical device with stimulated FWM fed by an un-

depleted pump and a classical seed light with effective power that is dependent on the photon energy and density of states. Therefore the same optical devices with good classical stimulated FWM efficiency can also work as efficient sources for generating quantum photons using spontaneous four-wave mixing[54], because both spontaneous FWM and stimulated FWM have the same Hamiltonian operator. The linear relationship between spontaneous FWM and stimulated FWM coefficients is analogous to the linear relationship between the Einstein coefficients for spontaneous emission (absorption) and stimulated emission.

5.1 Theoretical efficiency and optimum designs

This section presents the conversion efficiency of OPWC based on degenerate FWM. Emphasis is put on microresonators where all the three interacting light modes (signal, pump and idler) can be simultaneously resonantly enhanced. The nonlinear interaction in such resonators is enhanced as a result of enhanced optical power or interaction length compared to that in waveguides. In general, no simple analytical expression for the OPWC efficiency can be derived, except in the simplest case of negligible nonlinear loss and undepleted input light. However, numerical solutions can always be achieved using a coupled-mode theory for nonlinear interaction summarized in Sec. 4.1. In the end, optimum designs of optical resonators for various nonlinear optical applications are described.

The parametric wavelength conversion efficiency by degenerate four-wave mixing, defined as the ratio of converted light power and input seed light power, $\eta = \frac{P_{i,\text{out}}}{P_{s,\text{in}}}$, can be calculated using the coupled-mode theory equations 4.1 presented in Sec. 4.1, with no input light at the idler frequency (i.e., $S_{i,+} = 0$)

$$\begin{aligned}
\frac{dA_s}{dt} &= (j\omega_{s0} + j\delta\omega_s - j\omega_s - r_{s,\text{tot}})A_s - j\omega_s\beta_{\text{fwm},s}A_p^2A_i^* - j\sqrt{2r_{s,\text{ext}}}S_{s,+} \\
\frac{dA_p}{dt} &= (j\omega_{p0} + j\delta\omega_p - j\omega_p - r_{p,\text{tot}})A_p - 2j\omega_p\beta_{\text{fwm},p}A_p^*A_sA_i - j\sqrt{2r_{p,\text{ext}}}S_{p,+} \\
\frac{dA_i}{dt} &= (j\omega_{i0} + j\delta\omega_i - j\omega_i - r_{i,\text{tot}})A_i - j\omega_i\beta_{\text{fwm},i}A_p^2A_s^* - j\sqrt{2r_{i,\text{ext}}}S_{i,+} \\
S_{k,-} &= S_{k,+} - j\sqrt{2r_{k,\text{ext}}}A_k, \quad (k \in \{s, p, i\}).
\end{aligned} \tag{5.1}$$

In general, these nonlinear equations don't have simple solutions. However, at certain circumstances there equations can be simplified. For example, when the nonlinear loss is negligible, nonlinear conversion is small and thus both the pump and seed light are undepleted in the resonator, the steady-state in-cavity energies of the pump and seed light, $|A_k|^2$, are given by

$$|A_k|^2 = \frac{2r_{k,\text{in}}}{\Delta\omega_k^2 + r_{k,\text{tot}}^2} P_{k,\text{in}} \quad (5.2)$$

where $k \in \{s, p\}$, $r_{k,\text{tot}} = r_{k,\text{o}} + r_{k,\text{in}} + r_{k,\text{out}}$ is the total linear loss, $\Delta\omega_k = \omega_{k\text{o}} + \delta\omega_k - \omega_k$ is the resonance frequency detuning, $P_{k,\text{in}} = |S_{k,+}|^2$ is the on-chip light power in the input waveguide.

Then the conversion efficiency is obtained by inserting Eq. 5.2 to Eqs. 5.1

$$\eta = \frac{P_{i,\text{out}}}{P_{s,\text{in}}} = |\omega\beta_{\text{fwm}}P_{p,\text{in}}|^2 \frac{2r_{i,\text{out}}}{\Delta\omega_i^2 + r_{i,\text{tot}}^2} \frac{2r_{s,\text{in}}}{\Delta\omega_s^2 + r_{s,\text{tot}}^2} \left(\frac{2r_{p,\text{in}}}{\Delta\omega_p^2 + r_{p,\text{tot}}^2} \right)^2 \quad (5.3)$$

The above expression for FWM conversion efficiency is consistent with that obtained using wave propagation method [55]

$$\eta = \frac{P_{i,\text{out}}}{P_{s,\text{in}}} = |\gamma P_{p,\text{in}} L_{\text{eff}}|^2 F E_p^4 F E_s^2 F E_i^2 e^{-\alpha L_{\text{cav}}} \quad (5.4)$$

where the third-order nonlinear coefficient in the waveguide, γ , is related to β_{fwm} as $\gamma = \frac{\omega\beta_{\text{fwm}}n_{\text{nl}}^2 L_{\text{eff}}}{c^2}$ (see Eq. A.19), $L_{\text{eff}} = \left| \frac{e^{-(\alpha-j\Delta\beta)L_{\text{cav}}} - 1}{\alpha-j\Delta\beta} \right|$ is the effective nonlinear interaction length in the cavity with the effects of linear loss and phase mismatch included, L_{cav} is the propagation length in the microcavity, α is linear loss rate of optical power due to absorption, scattering and radiation in the cavity, $\Delta\beta = 2\beta_p - \beta_s - \beta_i$ is the propagation constant mismatch, and $F E_k$, $k \in \{s, p, i\}$, is the field enhancement factor in the cavity, and is given by $F E_k = \frac{-j\kappa}{1 - t e^{(-\alpha/2 + j\beta)L_{\text{cav}}}} \approx \left(\frac{2r_{k,\text{ext}} \text{FSR}}{\Delta\omega_k^2 + r_{k,\text{tot}}^2} \right)^{1/2}$. In addition, note that the expression for FWM efficiency, Eq. 5.4 also works for compound resonators with resonance modes of longitudinally nonuniform intensity, such as the triple-ring resonator presented in Sec. 2.3.1, where L_{cav} is the sum of the circumferences of the two outer ring cavities. Therefore the resonant enhancement of nonlinear interaction in a resonator can be interpreted in two different ways – it results from either enhanced optical power for all four interacting light with the interaction length equal to the optical propagation length of the cavity, or largely extended nonlinear interaction length with the same optical power and quasi-phase matching (such that the

phase mismatch term contains L_{cav} rather than an extended length). However, it's not valid to claim that there is simultaneous enhancement of optical power and interaction length.

Eqs. 5.3 and 5.4 show that the OPWC efficiency increases with reduced frequency detuning $\Delta\omega_k = \omega_{k0} + \delta\omega_k - \omega_k$, $k \in \{s, p, i\}$. Because the frequency shift ($\delta\omega_k$) depends on a combination of thermal optical effect, phase modulation and free-carrier dispersion with different shifting directions, and varies with optical power, it is critical to pre-shift the ‘‘cold-cavity’’ resonance frequencies (ω_{k0}) in design according to an estimate of frequency shift at work. Besides, electrical heaters can be employed to tune a resonator after fabrication.

In addition, if the resonance frequencies of the three light modes (signal, pump and idler) do not satisfy the energy conservation condition, i.e., $\omega_{s0} + \delta\omega_s + \omega_{i0} + \delta\omega_i - 2(\omega_{p0} + \delta\omega_p) = 0$, the frequency detuning cannot be simultaneously reduced to 0. Although device temperature change often results in equal shift of the resonance frequencies of the three interacting light in four-wave mixing (excluding cases of nonuniform temperature change in a resonator with nonuniform mode intensity), nonlinear optical effects such as Kerr effect and free carrier dispersion always lead to unequal changes of resonance frequencies. For example, when a strong pump light is dominant in the resonator, the frequency shifts due to cross phase modulation at the signal and idler resonances are twice as large as that at the pump resonance due to self-phase modulation. Therefore in the case of negligible free carrier dispersion, a slight anomaly dispersive resonator (i.e., $\omega_{s0} + \omega_{i0} - 2\omega_{p0} > 0$) is required to per-compensate resonance shift due to phase modulation.

Besides, Eq. 5.4 shows that the OPWC efficiency decreases with phase mismatch $\Delta\beta L_{\text{cav}}$, because idler light generated at different locations in the resonator does not add up with the same phase. However, this dependence is missing in Eq. 5.3 derived from coupled-mode theory (CMT). This is because CMT intrinsically uses lumped mode energy and ignores the field propagation aspect in the resonator. However, the effect of phase mismatch on the OPWC efficiency in a resonator is much weaker than that of resonance frequency detuning, and thus Eq. 5.3 is still valid in practice.

It should also be noted that when calculating the field enhancement factor for the interacting light, the input port is relevant to the signal and pump light while the output port is relevant

to the generated idler light, and each light can have different field enhancement factor in the same resonator due to different external couplings. This fact is important in cases where multiple waveguides couple to the resonator with different coupling rates at different resonant modes (for mode-dependent coupling, see Sec. 2.3.1.2), and in fact can be employed for optimum design of various nonlinear devices. For example, in order to maximize the OPWC efficiency, critical coupling is desired for all three light. However, for parametric data bit conversion, the external coupling rates of the signal and idler resonances need to accommodate the data bandwidth, while the pump light is critically coupled to maximize the parametric gain. Another example is laser linewidth narrowing based on optical parametric processes [56, 57], where the signal resonance has large bandwidth to allow more low-coherence input light to be loaded into the resonator, and the coupling for the idler light is reduced to force a high coherence in the converted light.

5.1.0.1 “Eigenmode” picture of four-wave mixing:

It should be noted that the evolution of the energies of the three interacting light via FWM in the resonator ($|A_k|^2$, $k \in \{s, p, i\}$) depends on the relative phases among them. Specifically, four-wave mixing is a reversible process —while two pump photons are converted to a pair of signal and idler photon, the latter are also annihilated to generate pump photons simultaneously. Before arriving at an equilibrium state where the two opposite interactions cancel each other, the net energy flow depends on not only the relative magnitudes of the three light, but also their relative phases. In fact, the coupled-mode theory equations 5.1 can be transformed onto the basis of “eigenmodes” of four-wave mixing

$$\frac{dA_{\pm}}{dt} = (j\Delta\omega_s - r_{s,\text{tot}})A_s \pm \omega_s |\beta_{\text{fwm}} A_p^2| A_{\pm} - j\sqrt{r_{s,\text{ext}}} S_{s,+} \quad (5.5)$$

$$\frac{dA_p}{dt} = (j\Delta\omega_p - r_{p,\text{tot}})A_p + \omega_p \beta_{\text{fwm}}^* A_p^* (-|A_+|^2 + |A_-|^2 + A_+ A_-^* - A_+^* A_-) - j\sqrt{2r_{p,\text{in}}} S_{p,+} \quad (5.6)$$

where $A_{\pm} = \frac{1}{\sqrt{2}}(A_s \mp jA_i^*)$, and A_+ (A_-) represents a pair of signal and idler light with parametric gain (loss) in degenerate-pump four wave mixing. Also the pump light loses (gains) energy by interacting with A_- (A_+). Note that a few assumptions have been made in writing down Eqs. 5.5 for

simplicity. First, the signal and idler light are assumed to have equal resonance frequency detuning ($\Delta\omega_s = \Delta\omega_i$), loss rates ($r_{s,\text{tot}} = r_{i,\text{tot}}$) and external coupling rates ($r_{s,\text{in}} = r_{i,\text{in}}$, $r_{s,\text{out}} = r_{i,\text{out}}$). Otherwise the ‘‘eigenmodes’’ would be $A_{\pm} \propto [(\Delta\omega_i + jr_{i,\text{tot}})A_s \mp j(\Delta\omega_s + jr_{s,\text{tot}})A_i^*]$. Besides, there are in total three degrees of freedom in the phases of the three light, and their common phase is fixed by setting the phase of the product $\beta_{\text{fwm}}A_p^2$ to be 0. Also the differences between ω_s and ω_i is neglected. These assumption don't affect the generality of the ‘‘eigenmodes’’ picture of four-wave mixing.

The two eigenmodes A_{\pm} evolves together with A_p and the steady-state solutions are

$$A_{\pm} = \frac{-j\sqrt{r_{s,\text{ext}}}S_{s,+}}{-j\Delta\omega_s + r_{s,\text{tot}} \mp \omega_s|\beta_{\text{fwm}}A_p^2|} \quad (5.7)$$

$$|A_p|^2 = \frac{2r_{p,\text{in}}P_{p,\text{in}}}{(\Delta\omega_p + 2\Im[A_+A_-^*])^2 + [r_{p,\text{tot}} + \omega_p|\beta_{\text{fwm}}(|A_+|^2 - |A_-|^2)]^2} \quad (5.8)$$

where $r_g \equiv \omega_s|\beta_{\text{fwm}}A_p^2|$ is the parametric gain (loss) coefficient for $A_+(A_-)$. Because of the parametric gain (loss), the effective critical coupling conditions for A_{\pm} are different from those of A_s and A_i . For example, to maximize $|A_+|^2$ the optimum input coupling $r_{s,\text{in}}$ should decrease by r_g . In general, the two equations above need to be solved together to find out the OPWC efficiency in steady-state. When the pump light is undepleted from the four-wave mixing process, the eigenmodes A_{\pm} evolves separately, and the in-cavity pump light energy is given by

$$|A_p|^2 = \frac{2r_{p,\text{in}}P_{p,\text{in}}}{\Delta\omega_p^2 + r_{p,\text{tot}}^2}. \quad (5.9)$$

The generated idler light A_i and amplified signal light A_s are obtained as a combination of A_{\pm}

$$A_s = \frac{1}{\sqrt{2}}(A_+ + A_-) = \frac{-j\sqrt{2r_{s,\text{ext}}}S_{s,+}(-j\Delta\omega_s + r_{s,\text{tot}})}{(-j\Delta\omega_s + r_{s,\text{tot}})^2 - (\omega_s|\beta_{\text{fwm}}A_p^2|)^2} \quad (5.10)$$

$$A_i = \frac{j}{\sqrt{2}}(A_-^* - A_+^*) = \frac{-j\sqrt{2r_{s,\text{ext}}}S_{s,+}\omega_s|\beta_{\text{fwm}}A_p^2|}{(j\Delta\omega_s + r_{s,\text{tot}})^2 - (\omega_s|\beta_{\text{fwm}}A_p^2|)^2}. \quad (5.11)$$

Therefore the expression for OPWC efficiency is

$$\eta = \frac{2r_{i,\text{ext}}|A_i|^2}{P_{s,\text{in}}} = \frac{(2r_{s,\text{in}}\omega|\beta_{\text{fwm}}A_p^2|)^2}{|(j\Delta\omega_s + r_{s,\text{tot}})^2 - (\omega_s|\beta_{\text{fwm}}A_p^2|)^2|^2} \quad (5.12)$$

The above expression for OPWC efficiency reduces to Eq. 5.3 when the parametric gain r_g is small compared to linear loss and coupling rates and thus signal light is also undepleted in the resonator. In this scenario, the phases of the pump and signal light are determined by their input light phases, and not affected by the nonlinear interaction. The phase of the converted idler light is unambiguously determined by the phases of the pump and signal light in the resonator and corresponds to only parametric gain.

5.2 Experiment demonstration: four-wave mixing in silicon coupled-cavity resonators with port-selective, orthogonal supermode excitation

In this section¹, we propose coupled-cavity triply-resonant systems for degenerate-pump four-wave mixing (FWM) applications that support strong nonlinear interaction between distributed pump, signal and idler modes, and allow independent coupling of the pump mode and signal/idler modes to separate ports based on non-uniform supermode profile. We demonstrate seeded FWM with wavelength conversion efficiency of -54 dB at input pump power of 3.5 dBm, and discuss applications of such orthogonal supermode coupling.

Nonlinear optical interaction can be resonantly enhanced in microcavities with small mode volumes and high field enhancements. Degenerate-pump four-wave mixing (FWM), for example, favors triply-resonant cavities [59]. A single microring cavity used for FWM, with three interacting waves at different longitudinal order resonances, has a trade-off between mitigating dispersion by using a large ring and enhancing nonlinear interaction with small mode volume [28]. The design also constrains the choice of pump, signal and idler wavelengths.

Since the minimum number of modes required for FWM is three, one can avoid the constraints imposed by using multiple longitudinal modes of a single cavity by, instead, coupling three cavities together where the interacting signal, pump and idler wavelengths each excite a compound resonance of the coupled-cavity resonator. Both stimulated and spontaneous FWM have been demonstrated in a triple-cavity resonator [60, 27]. In these devices, however, the external ports

¹ This section is reproduced nearly verbatim from my paper[58]

(bus waveguides) couple to all resonance modes with fixed ratio of coupling rates, leading to undesirable crosstalk or reduced efficiency. The use of more than three coupled resonators has also been investigated in coupled-resonator optical waveguides (CROW) [61, 62, 63] taking advantage of reduced group velocity and broad passband.

A desirable quality of a resonant four-wave mixing device is separate and independent waveguide coupling to the three interacting modes in order to both engineer the linewidths/decay rates (and therefore field enhancement) of each resonant mode along with intrinsic isolation between the input pump and generated signal/idler light. Optimum design of an optical parametric oscillator calls for unequal coupling of the waveguide(s) to the three resonances that interact via FWM [2, 1]. Also, in parametric wavelength conversion and/or amplification of an optical data stream, to maximally utilize a CW pump, we suggest that a narrow-linewidth pump resonance should be used to minimize the needed pump power, while high bit-rate data streams require wide-linewidth signal and idler resonances to accommodate the modulated signals. It is also advantageous in a photon pair generator to critically couple the pump mode while the signal/idler mode are over-coupled to promote both efficiency and photon time correlation. While controllable mode-selective coupling was recently proposed [2] and partially demonstrated [27], the latter work still couples two modes to one port and all three to another port resulting in the generated correlated photons being randomly and uncontrollably routed to two different output ports.

In this section we demonstrate orthogonal coupling of supermodes in a triple-cavity resonator to two separate bus waveguides, show stimulated FWM in such a device and propose broad applications based on it. In general, independent orthogonal excitation of all three resonances would require three separate bus waveguides, with each coupled exclusively to one of the three resonances. Here we present a more restricted design where the pump is independently controlled from the signal and idler. This design is suitable to degenerate FWM because signal and idler physics are symmetric. The device enables breaking the trade-off between increasing parametric gain (by reducing volume) and mitigating dispersion, as well as the choice of wavelengths by design, with independently designable coupling to the resonances. We demonstrate four-wave mixing for the

first time in such a device, and discuss potential applications.

To demonstrate the concept, triple-ring resonators were fabricated on SOI wafers with a 220 nm device layer through the ePIXfab foundry service[64]. A ring radius of $3.5 \mu\text{m}$ was chosen to minimize mode volume without compromising the quality factor (Q) through bending loss. Due to lithographic and device layer thickness variations, the three rings can have different resonance frequencies, resulting in unequal frequency spacing between the supermodes ($2\omega_p \neq \omega_s + \omega_i$). In addition, coupling-induced frequency shifts can also cause unequal frequency spacing when the coupling gaps are small since light in the middle ring sees a different environment than that in the outer rings [65]. To compensate for any frequency mismatch, resistive metal microheaters were fabricated on top of the oxide top cladding to thermally tune the compound resonator elements. Each ring was tuned independently to restore the designed supermode, and the interferometric phase in the “pump bus” was tuned to control its coupling to each supermode. Fabricated triple-ring cavities with microheaters are shown in Fig. 5.1(a). The heaters were fabricated in a two-step procedure involving scanning electron-beam lithography to enable fine features, and contact photolithography for the larger pads.

Fig. 5.1(b) shows passive spectra of a triple-ring resonator, where the insertion loss is plotted against swept laser wavelength. The notation “ps” denotes the case when the input fiber is coupled to the “pump bus” and the output fiber is coupled to the “signal bus”, etc. The free spectral range (FSR) is non-uniform due to dispersion. However, the compound resonator has three modes with nearly equal frequency spacing within one FSR, enabling degenerate-pump FWM near 1550 nm. The spectra verified the port-selective coupling of the three supermodes. In the through port transmission of the “pump bus” (i.e. the “pp” curve), there are no substantial transmission dips at the signal/idler resonance frequency (see “A” and “C” in Fig. 5.1(b)), showing that coupling of the “pump bus” to the signal/idler resonance of the triple-ring cavity is frustrated, per design. Similarly the “signal bus” couples weakly to the pump resonance as indicated by the little dip at “B”. Therefore, the linewidth of the signal/idler (pump) resonance is controlled entirely via its coupling to the “signal (pump) bus” and intrinsic cavity loss, and can be engineered independently

through the respective ring-bus coupling gap. The “pump bus” (“signal bus”) was designed to be critically coupled to the pump (signal/idler) resonance assuming an unloaded Q (loss Q) of around 150,000. However, we extracted an unloaded Q of only 50,000 from the passive spectrum (as evidenced by the small dips “D”, “F” (“B”) at signal/idler (pump) wavelength in the “signal (pump) bus” through port transmission), showing that all three resonances are under-coupled.

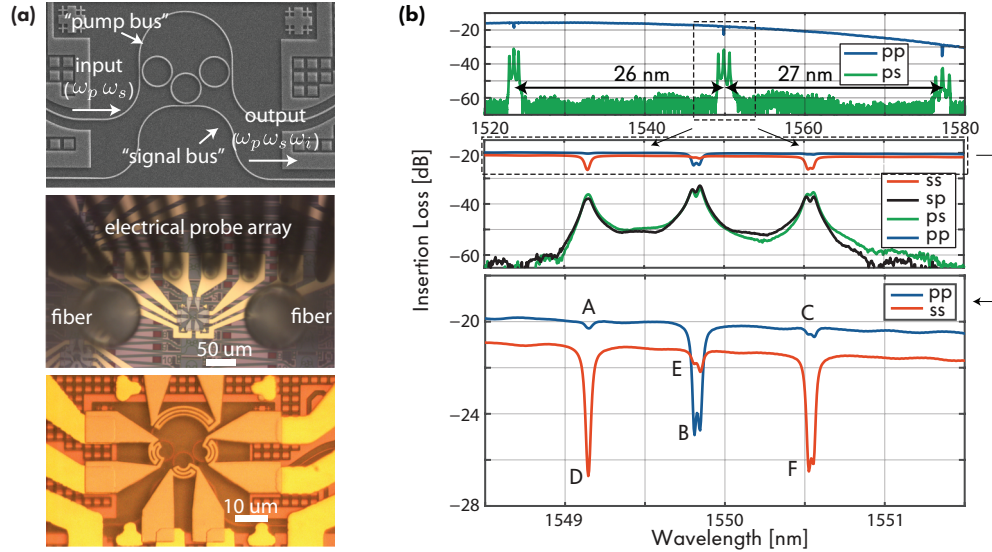


Figure 5.1: (a) Micrographs of device under test with heaters; (b) optical transmission spectra of four port combinations (legend: “ps”=“pump bus” input, “signal bus” output). The little transmission dips E (A,C) show that “signal (pump) bus” couples weakly to pump (signal/idler) resonance.

In the experiment, we thermally tuned the individual rings and interferometric bus to enable equally-spaced supermodes, and coupled the pump and seed light resonant with the compound cavity both via the “pump” bus (the seed should enter via the signal bus and this non-ideal excitation was governed by experimental constraints). Parametric wavelength conversion via FWM was observed at an input pump power of 3.5 dBm and seed power of -7.3 dBm in the input “pump bus”. Fig. 5.2(a) shows the power spectrum of output light at drop port in “signal bus” measured with an optical spectrum analyzer (OSA); the apparent wide linewidths are due to the filter response

of the OSA. The generated idler light power exiting in the “signal bus” at the device was estimated to be -61.3 dBm after taking into consideration the insertion loss of fiber-chip couplers. Thus the measured FWM conversion efficiency from signal light at input “pump bus” to generated idler light at the “signal bus” is approximately -54 dB at in-waveguide pump power of 3.5 dBm. Since the pump light coupling from the triple-ring cavity to the “signal bus” is frustrated by design [see Fig. 5.1(b), with a rejection of 13 dB], the demonstrated device works as an effective filter for the strong pump light when detecting generated signal at the “signal bus”.

To understand the limitations, efficiency scaling and potential of this device, we study the theoretical FWM conversion efficiency taking into account the two-photon absorption (TPA) and free-carrier absorption (FCA). We assume resonant excitation of pump and seed light, as well as perfect phase matching and critical coupling for the three modes. In Fig. 5.2(b) we show the simulated wavelength conversion efficiency (from signal to idler light) in silicon microresonator based on degenerate-pump FWM as a function of normalized pump power [1], which is the in-bus pump power normalized to the oscillation threshold power with optimum coupling when nonlinear loss can be neglected. This oscillation threshold power scales quadratically with intrinsic cavity loss rate and linearly with nonlinear interaction mode volume. The parametric wavelength conversion efficiency decreases with the ratio of free-carrier lifetime and intrinsic cavity photon lifetime (defined as $\tau_{\text{ph}} \equiv 1/r_o$, where r_o is intrinsic cavity loss). The under-coupled configuration in our fabricated device leads to lower cavity enhancement lowering both parametric conversion and free carrier generation via TPA. With normalized pump power of only -12.3 dB (i.e. 3.5 dBm actual power in bus) and assuming free carrier lifetime of 1 ns, we can therefore predict that the nonlinear loss only slightly decreases the FWM efficiency in our device.

When the TPA can be neglected and conversion efficiency is small, the pump and seed are not depleted and the FWM efficiency has a simple expression [1, 28]:

$$\eta = (\omega\beta_{\text{fwm}}P_{\text{p,in}})^2 \frac{2r_{\text{i,out}}}{\Delta\omega_{\text{i}}^2 + r_{\text{i,t}}^2} \frac{2r_{\text{s,in}}}{\Delta\omega_{\text{s}}^2 + r_{\text{s,t}}^2} \left(\frac{2r_{\text{p,in}}}{\Delta\omega_{\text{p}}^2 + r_{\text{p,t}}^2} \right)^2 \quad (5.13)$$

where β_{fwm} is the FWM coefficient in the resonator which is inversely proportional to the nonlinear

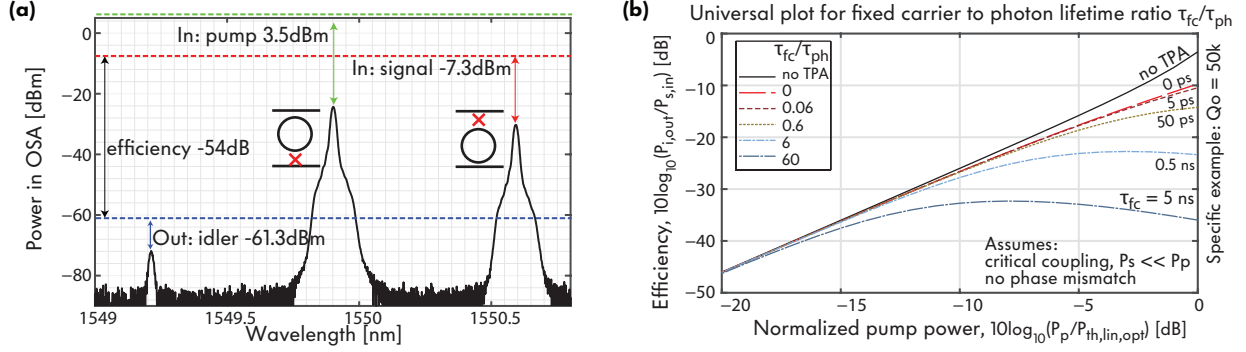


Figure 5.2: (a) Seeded FWM in silicon triple-ring resonator with conversion efficiency of -54 dB. (b) Degenerate-pump FWM wavelength conversion efficiency vs. normalized pump power [1] in a silicon microcavity with nonlinear loss included. Critical coupling and perfect phase matching are assumed. A few ratios of free carrier and photon lifetime are used.

interaction mode volumes, $P_{p,in}$ is the input pump power in the “pump bus”, $r_{k,t}$ ($k \in \{s, p, i\}$) is total loss rate for resonance ω_k , and $\Delta\omega_k$ is the frequency detuning of the excitation from the corresponding resonance. $r_{p,in}$ and $r_{s,in}$ are coupling rates from the “pump bus” to the resonator at the pump and signal frequencies, and $r_{i,out}$ is the coupling rate from the resonator to the “signal bus” at the idler frequency. Maximum efficiency is achieved with critical coupling at the input bus for the pump and seed light, and at the output bus for the idler light. However, as Fig. 5.1(b) shows our device is under-coupled, with measured unloaded Q of 50,000 and external Q of 120,000-170,000. Furthermore, the signal light was inserted via the “pump bus” due to experimental constraints (using the same input fiber as the pump), **not** in the “signal bus” as is optimal. Therefore, the signal light is very poorly coupled into the resonator. With the actual weak external couplings, the theory predicts a conversion efficiency of -47.3 dB, which is 6.7 dB higher than the measured -54 dB. The remaining difference, we believe, is due to excitation of non-ideal supermodes, resonance splitting due to the coupling of two counter-propagating travelling-wave in the rings, FCA, phase mismatch and inaccuracy in the estimating external couplings.

When the nonlinear loss can be neglected, the stimulated FWM conversion efficiency from signal light to idler light is proportional to the square of pump power, and the ratio η/P_p^2 , pump-normalized conversion efficiency (PNCE), should be used as a figure of merit for wavelength conver-

sion efficiency of a nonlinear mixer based on degenerate-pump FWM. This ratio was measured to be $8 \times 10^{-7} (\text{mW})^{-2}$ in our triple-ring device. Although the presently demonstrated FWM efficiency in our triple-ring device is smaller than those of the coupled resonator [60] and microring resonator with active carrier removal [66], we have demonstrated here the feasibility of performing FWM in a triple-ring resonator with separate bus waveguides coupling to the pump and signal/idler modes, enabling different linewidths for these modes. By launching the pump and seed light into separate input ports as intended, and ensuring critical coupling, we expect the efficiency in this device to increase by 20 dB to around -34 dB. This can be accomplished by providing separate grating couplers into the pump bus and signal bus input ports, in a geometry accessible by two separate input fibers carrying the pump and seed signal. Alternatively a 2D grating coupler could take the pump and signal from orthogonal polarizations in the input fiber into the two bus waveguides. Last, a co-polarized pump and signal in a single fiber can be separated into the pump and signal bus by a wavelength filter on chip. By increasing the unloaded quality factor from 50,000 to 500,000, and sweeping out free carriers, net gain could be within reach. The unloaded Q in the present devices is limited by larger than expected sidewall roughness on the ring cavities, and coupler radiation loss [67]. These factors are being currently addressed in revised designs and pose no fundamental limitation.

In summary, we have proposed and demonstrated coupled-cavity structures for resonantly enhanced four-wave mixing that enable independent coupling of pump, signal and idler resonances to separate ports. We expect it to enable an array of applications including optimum designs for parametric amplifiers, oscillators, squeezing, and photon pair generation including engineering of the biphoton joint spectral distribution.

5.3 Estimate of energy cost for data bit conversion based on four-wave mixing

In this section, the cost of optical energy per data bit in parametric wavelength conversion based on four-wave mixing in triple-cavity resonator systems is discussed. We take advantage of

the wavelength-dependent coupling of triple-cavity resonator, and choose a weak, critical coupling for pump resonance to maximize parametric gain ($r_{p,\text{ext}} = r_0$), and a strong, equal coupling for the signal and idler light ($r_{s,\text{ext}} = r_{i,\text{ext}} \gg r_0$). The incoming data rate is chosen at the half-width-half-maximum of the signal resonance frequency of the resonator. Assuming amplitude-modulated data signal with equal probabilities of 0s and 1s. A continuous-wave pump light is used to maintain a constant parametric gain for the incoming data signal in the resonator. For simplicity, we assume the in-cavity light energy is undepleted from nonlinear interaction loss. According to Eq. 5.9 and Eq. 5.12, the OPWC efficiency is maximized when all light (data signal, pump and generated idler) are resonant in the cavity

$$\eta = \left(\frac{2r_{s,\text{in}}\omega|\beta_{\text{fwm}}|\frac{P_p}{2r_0}}{r_{s,\text{tot}}^2 - (\omega_s|\beta_{\text{fwm}}|\frac{P_p}{2r_0})^2} \right)^2. \quad (5.14)$$

In practise, an OPWC efficiency of 0 dB (i.e., $\eta = 1$, no power loss from original data to converted data) is desired. According to Eq. 5.14, the pump light power and data rate is related

$$P_p = \frac{2r_0}{\omega|\beta_{\text{fwm}}|} \left(\sqrt{r_{s,\text{tot}}^2 + (r_{s,\text{tot}} - r_0)^2} - r_{s,\text{tot}} + r_0 \right) \quad (5.15)$$

Since the data signal power is usually much smaller than the pump light power, the data signal energy is neglected in calculating the total optical energy per bit (EPB)

$$\text{EPB} = \frac{P_p}{r_{s,\text{tot}}} = \frac{1}{Q_0|\beta_{\text{fwm}}|} \left(\sqrt{1 + \left(1 - \frac{r_0}{r_{s,\text{tot}}}\right)^2} - 1 + \frac{r_0}{r_{s,\text{tot}}} \right) \quad (5.16)$$

where $Q_0 = \frac{\omega}{2r_0}$ is the intrinsic cavity quality factor, β_{fwm} is the four-wave mixing coefficient in the resonator. For a chosen data rate ($r_{s,\text{tot}}$), the optical energy cost per data bit in OPWC decreases with intrinsic cavity loss (r_0). And for a given intrinsic cavity quality factor (Q_0), EPB decreases as the incoming data rate goes up. In reality, the intrinsic cavity quality factor is limited by light absorption, scattering and radiation, and the data rate is limited by the modulation speed.

Next we use some practical parameters to estimate the energy cost per data bit. Assuming an intrinsic cavity quality factor of 10^5 at the wavelength of 1550 nm ($r_0 \approx 6.1 \times 10^9$ Hz) and a data rate of 10 Gbps, Eq. 5.16 gives EPB of 950 fJ/bit and 150 fJ/bit for the crystalline silicon and a-Si:H triple-ring resonators shown in Table. 6.2 near 1550 nm, respectively.

Chapter 6

Optimum design of optical parametric oscillators

6.1 Introduction

This chapter¹ focuses on a theoretical study on triply-resonant optical parametric oscillators (OPOs) based on degenerate four-wave mixing (FWM) that includes physics and degrees of freedom relevant to microphotonic (on-chip) device implementations. As previous chapters show, the third-order optical nonlinearity ($\overline{\chi}^{(3)}$) is strong in semiconductors like silicon as well as a number of nonlinear glasses, and can be greatly enhanced in a microcavity due to strong transverse spatial confinement and large effective interaction length [14]. With high enough parametric gain, OPO is possible, where a single input pump wavelength enables oscillation at two other wavelengths resonant in the microcavity, with substantial energy conversion. OPO enables coherent light generation for many classical photonics applications, including light sources at wavelengths where gain media are underdeveloped, and optical frequency comb generation [16, 17].

Previous demonstrations include optical parametric oscillation based on four-wave mixing in silica microtoroids [68], silica [69] and silicon nitride (Si_3N_4) microring resonators [52], where nonlinear loss due to two-photon-absorption (TPA) is negligible. It is of interest to investigate the fundamental limits of micro-OPO performance, and find designs that achieve the best possible performance for given material parameters. This is important because on-chip microphotonic cavity geometries have access to greater degrees of freedom in design than either bulk optics or thin film optics [70], as previously shown in optimal filters [71, 72], modulators [73, 74], light trapping [75, 76].

¹ This chapter is reproduced nearly verbatim from my paper [1].

Also, a first-principles look is important because on-chip implementations in semiconductors may have substantial nonlinear losses in addition to linear loss, including two-photon absorption (TPA), and TPA-induced free-carrier absorption [77, 9]. Finally, even the typical scaling of resonator quality factor due to the linear losses – the linear unloaded or loss Q – is different in e.g. tabletop cavities, where it is normally limited by lumped mirror loss, and integrated microring or photonic crystal cavities, where it is normally dominated by a distributed loss (per unit length) that may be due to waveguide surface roughness, material absorption, or bulk scattering. This has an impact on scaling of designs.

In this chapter, we present a general design approach for optical parametric oscillators based on degenerate-pump FWM to achieve the maximum possible conversion efficiency. Previously, temporal coupled-mode theory (CMT) has been used successfully to analyze resonant nonlinear systems [29], including ones with four-wave mixing [59]. We develop a temporal coupled mode theory (CMT) model of the parametric oscillator in Fig. 6.1, and normalize it with respect to linear losses, giving a very general representation of the OPO design problem, in terms of normalized pump power and the material nonlinear figure of merit (NFOM). We also address free carrier losses by a normalized parameter. The optimum design solutions to this model are thus broadly applicable across a wide parameter space, and we are able to draw general conclusions about oscillation thresholds, conversion efficiency, and optimum coupling independent of the particular device geometry.

Our model bears out some fundamental limitations of conventional (including integrated photonic) OPO implementations, and suggests the synthetic “photonic molecule”-like, coupled-cavity systems proposed in Chapter 2 are capable of realizing these optimum OPO designs. In particular, different external-coupling linewidths are desirable for the pump, signal and idler wavelength resonances. Besides, dispersion engineering is separated from control of resonant wavelengths, and can be accomplished in part using interferometric cavity and coupled-cavity configurations in addition to design of the waveguide cross-section. These amount to resonant “photonic molecules” that allow effective engineering of both resonance frequencies (states) and linewidths (lifetimes)

independently.

The study also leads to a couple of general conclusions. First, we find that the maximum achievable conversion efficiency is bound to an upper limit by nonlinear and free-carrier losses independent of pump power, while linear losses only increase the pump power required to achieve a certain conversion efficiency. Specifically, we show that there is a critical value of the nonlinear figure of merit in materials beyond which parametric oscillation is not possible in a certain cavity mode structure. On the other hand, we show, for example, that crystalline silicon structures can oscillate in principle, even in the telecom band where nonlinear losses are present. Second, we provide a general oscillation threshold formula for OPOs that includes both two-photon absorption (TPA) and free-carrier absorption (FCA) losses in a normalized way.

We also provide some practical examples of experimental relevance, to give the reader some orientation. For example, 0.21 mW of pump light at $1.55 \mu\text{m}$ in silicon microrings ($R=3 \mu\text{m}$) with intrinsic quality factor (Q_o) of 10^6 and a free-carrier-lifetime of 60 ps can produce parametric oscillation with about 0.1% conversion efficiency (free-carrier-lifetime of 12.2 ps has been demonstrated [78]), and the efficiency can reach 2% as free-carrier-lifetime approaches zero (e.g. via active car-

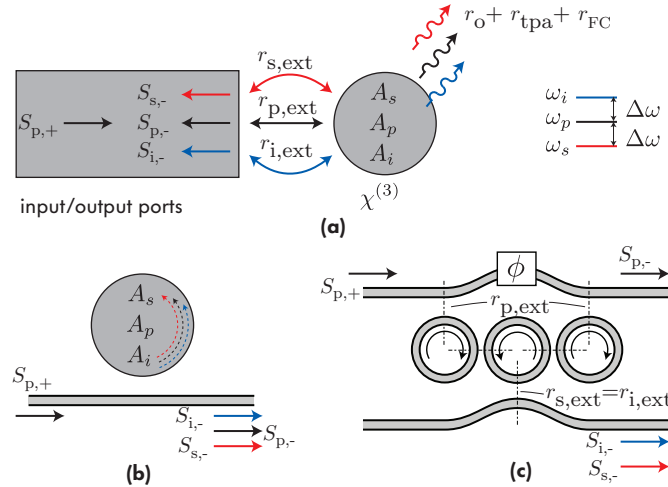


Figure 6.1: (a) Illustration of the micro-OPO model including a multimode resonator; (b) a traveling-wave resonant structure enables separated input and output ports; (c) example proposed multimode resonator based on 3 coupled microring cavities, showing an approach to unequal pump and signal/idler external coupling [2].

rier sweepout [77, 9, 19]). In general, an OPO based on silicon as the source of parametric gain cannot produce oscillation with conversion efficiencies on the order of 1 at 1550 nm due to TPA, but we show that they can achieve oscillation at up to a few percent conversion in principle. At wavelengths above around $2.2 \mu\text{m}$ (i.e. below the half bandgap energy of silicon), efficiency close to 17% is achievable in a microring ($R=7 \mu\text{m}$) with a pump power of 1 mW and a cavity intrinsic Q of 10^6 . In Si_3N_4 microrings ($R=15 \mu\text{m}$), a weaker nonlinearity but absence of TPA in the telecom band enables conversion efficiencies approaching 10% at about 9 mW pump power with a Q_o of 10^6 , where the maximum possible is 50% to each of the signal and idler (details in Section 6.3.2.1).

This chapter is organized as follows. In Section 6.2, we provide our CMT model of the general parametric oscillator, and discuss approximations and assumptions. In Section 6.2.1, we normalize the model with respect to linear and nonlinear loss, so that the results of computations are universally applicable across various microcavity systems. In Section 6.3, we explain the approach for finding the optimum design, and in Sections 6.3.1–6.3.3 we solve the problem of optimum OPO design approximately and exactly, and provide universal design curves for situations with and without TPA and FCA losses.

6.2 Physical model of a parametric oscillator

We begin with the coupled mode theory in time (CMT) model summarized in Chapter 4 to describe the dynamics of linear and nonlinear phenomena in microcavities for optical parametric oscillation. We focus on a triple-resonant cavity that can resonantly enhance one single, a degenerate pump and one idler light. This three-mode model is a valid assumption if the optical resonator is dispersion engineered to allow phase matching to the pump for only one pair of output signal and idler wavelengths. This is unlike a periodic comb generator [68] which produces many output wavelengths, but can be accomplished with appropriate resonator and dispersion engineering [79] and, we expect, is the optimal way to use the parametric gain when the objective is efficient generation of a single pair of signal/idler output wavelengths. We focus on this case here because it is the simplest, but much of the intuition provided by our conclusions will apply more broadly.

The CMT model for the three-resonance system illustrated in Fig. 6.1 is

$$\frac{dA_s}{dt} = -r_{s,\text{tot}}A_s - j\omega_s\beta_{\text{fwm},s}A_p^2A_i^* \quad (6.1a)$$

$$\frac{dA_p}{dt} = -r_{p,\text{tot}}A_p - 2j\omega_p\beta_{\text{fwm},p}A_p^*A_sA_i - j\sqrt{2r_{p,\text{ext}}}S_{p,+} \quad (6.1b)$$

$$\frac{dA_i}{dt} = -r_{i,\text{tot}}A_i - j\omega_i\beta_{\text{fwm},i}A_p^2A_s^* \quad (6.1c)$$

$$S_{s,-} = -j\sqrt{2r_{s,\text{ext}}}A_s \quad (6.1d)$$

$$S_{p,-} = S_{p,+} - j\sqrt{2r_{p,\text{ext}}}A_p \quad (6.1e)$$

$$S_{i,-} = -j\sqrt{2r_{i,\text{ext}}}A_i \quad (6.1f)$$

where the definitions of $A_k(t)$, $S_{k,+}$ ($S_{k,-}$), ω_k , $\beta_{\text{fwm},k}$, $r_{k,\text{ext}}$ and $r_{k,\text{ext}}$ ($k \in \{p, s, i\}$) are the same as those in Chapter 4.

Approximations and assumptions: Without loss of generality, we make a few simplifying approximations and assumptions, as follows. First of all, we assume the resonant condition Eq. 4.2 is satisfied. In other words, we assume that the wavelengths of pump input, $S_{p,+}$, and signal/idler output match the “hot cavity” resonances after all resonance frequency shift is included. This is the most efficient case for OPO operation, and is a reasonable assumption because any frequency mismatch induced by self- and cross-phase modulation as well as free-carrier induced index change, can be compensated in principle by pre-shifting the “cold cavity” (no excitation) resonance frequencies by dispersion engineering of the cavity modes, or by actively tuning (e.g. thermally) the cavities during operation [80]. We also consider here unseeded operation of an OPO, i.e. free oscillation. In this case, there is no input power at the signal and idler frequencies beyond noise that is needed to start the FWM process.

Next, Sec. 4.2 shows there are six unique $\beta_{\text{tpa},mn}$ coefficients. To simplify the analysis and arrive at a single TPA coefficient, $\beta_{\text{tpa},mn} \equiv \beta_{\text{tpa}}$, we assume the transverse field profile dispersion is negligible (valid when $\omega_p \approx \omega_s \approx \omega_i$), and assume a single, traveling-wave cavity configuration, with traveling wave excitation. In this case, the TPA coefficient β_{tpa} also contains the same field overlap integral as β_{fwm} (see Sec. 4.2), and their ratio is given by the nonlinear loss sine σ_3 ,

defined as $\Im[\overline{\chi}_{\text{eff}}^{(3)}]/|\overline{\chi}_{\text{eff}}^{(3)}|$ of the dominating nonlinear material (see Sec. 4.2). The scalar $\overline{\chi}_{\text{eff}}^{(3)}$ takes into account of the tensor character of $\overline{\chi}^{(3)}$ and polarization of light. In the case where multiple nonlinear materials are present in the cavity, or the three light interacting in FWM have very different mode profile, the general expressions with mode overlap integrals are needed to represent $\beta_{\text{tpa,mn}}$ and β_{fwm} . We analyze the simplest case in this chapter to find out qualitative behaviour of on-chip optical parametric oscillators.

We also assume that each resonance has the same linear loss, $r_{\text{k,o}} = r_o$. Last, due to the symmetry of our model in the regime of $\Delta\omega/\omega_p \ll 1$, where $\Delta\omega = \omega_p - \omega_s = \omega_i - \omega_p$ (sufficiently that the signal, idler and pump mode fields confinement is similar), we assume that $\omega_s \approx \omega_i \equiv \omega$, and equal external coupling for the signal and idler resonances, $r_{\text{s,ext}} = r_{\text{i,ext}}$.

6.2.1 Normalized model of a parametric oscillator

To enable an analysis with more general conclusions, we can rewrite the CMT model in a normalized form:

$$\frac{dB_s}{d\tau} = -\rho_{\text{s,tot}}B_s - j2B_p^2B_i^* \quad (6.2a)$$

$$\frac{dB_p}{d\tau} = -\rho_{\text{p,tot}}B_p - j4B_p^*B_sB_i - j\sqrt{2\rho_{\text{p,ext}}}T_{p,+} \quad (6.2b)$$

$$\frac{dB_i}{d\tau} = -\rho_{\text{i,tot}}B_i - j2B_p^2B_s^* \quad (6.2c)$$

$$T_{s,-} = -j\sqrt{2\rho_{\text{s,ext}}}B_s \quad (6.2d)$$

$$T_{p,-} = T_{p,+} - j\sqrt{2\rho_{\text{p,ext}}}B_p \quad (6.2e)$$

$$T_{i,-} = -j\sqrt{2\rho_{\text{i,ext}}}B_i. \quad (6.2f)$$

The normalized variables are defined by

$$\tau \equiv r_o t \quad (6.3a)$$

$$B_k \equiv \frac{A_k}{A_o}, \text{ with } A_o \equiv \sqrt{\frac{2r_o}{\omega\beta_{\text{fwm}}}} \quad (6.3b)$$

$$T_{k,\pm} \equiv \frac{S_{k,\pm}}{S_o}, \text{ with } S_o \equiv \sqrt{\frac{2r_o^2}{\omega\beta_{\text{fwm}}}} \quad (6.3c)$$

$$\rho_{s,\text{tot}} \equiv 1 + \rho_{s,\text{ext}} + 2\sigma_3 (d_{\text{ss}}|B_s|^2 + 2d_{\text{sp}}|B_p|^2 + 2d_{\text{si}}|B_i|^2) + \rho_{\text{FC}} \quad (6.3d)$$

$$\rho_{p,\text{tot}} \equiv 1 + \rho_{p,\text{ext}} + 2\sigma_3 (2d_{\text{sp}}|B_s|^2 + d_{\text{pp}}|B_p|^2 + 2d_{\text{ip}}|B_i|^2) + \rho_{\text{FC}} \quad (6.3e)$$

$$\rho_{i,\text{tot}} \equiv 1 + \rho_{i,\text{ext}} + 2\sigma_3 (2d_{\text{si}}|B_s|^2 + 2d_{\text{ip}}|B_p|^2 + d_{\text{ii}}|B_i|^2) + \rho_{\text{FC}}. \quad (6.3f)$$

We arrive at normalized energy amplitudes B_k and wave amplitudes $T_{k,+}$, $T_{k,-}$ by normalizing out the linear loss rate r_o , parametric coupling β_{fwm} and nonlinear loss β_{tpa} from the problem. Note in Eq. (6.3c) that the input/output wave power, $|S_{k,\pm}|^2$, is normalized to $|S_o|^2$ which is the linear-loss oscillation threshold, i.e. the oscillation threshold in the absence of nonlinear losses, as shown later.

The terms $\rho_{k,\text{tot}} \equiv \frac{r_{k,\text{tot}}}{r_o}$ and $\rho_{k,\text{ext}} \equiv \frac{r_{k,\text{ext}}}{r_o}$, $k \in \{s, p, i\}$ are normalized decay rates. In order to arrive at an economical formalism to account fully for nonlinear loss, we use the nonlinear figure of merit (NFOM), or, more precisely our nonlinear loss sine σ_3 . In order to preserve the generality required by the six independent $\beta_{\text{tpa},mn}$ terms, we have introduced In Section 4.2 the coefficients d_{mn} , defined as

$$d_{mn} \equiv \frac{\beta_{\text{tpa},mn}}{\sigma_3\beta_{\text{fwm}}} \quad (6.4)$$

which serve as prefactors to the overlap integral ($\beta_{\text{tpa}} = \sigma_3\beta_{\text{fwm}}$) of the reference case (i.e. single-cavity with traveling-wave mode). These six coefficients are a property of the particular resonator topology, and excitation (standing vs. traveling wave), and they together with the NFOM (or σ_3) completely characterize a device's nonlinear performance merits related to TPA.

With the model reduced to a minimum number of coefficients, we last look at the normalized

free-carrier absorption rate, given by

$$\rho_{\text{FC}} \equiv \frac{r_{\text{FC}}}{r_o} = \sigma_3 \rho'_{\text{FC}} (d_{\text{ss}} |B_s|^4 + d_{\text{pp}} |B_p|^4 + d_{\text{ii}} |B_i|^4 + 4d_{\text{sp}} |B_s|^2 |B_p|^2 + 4d_{\text{ip}} |B_i|^2 |B_p|^2 + 4d_{\text{si}} |B_s|^2 |B_i|^2) \quad (6.5)$$

where we define a normalized FCA coefficient

$$\rho'_{\text{FC}} \equiv \frac{\tau_{\text{FC}} \sigma_a v_g \beta_{\text{fwm}}}{V_{\text{eff}} 2\hbar} \frac{4r_o}{(\omega \beta_{\text{fwm}})^2} = \left(\frac{\sigma_a n_{\text{nl}}^2}{\hbar \omega n_g n_2} \right) \frac{\tau_{\text{FC}}}{Q_o}.$$

The normalized FCA rate, ρ_{FC} , depends on nonlinear loss sine σ_3 (i.e. conventional NFOM), the topological d coefficients, the normalized mode energies ($|B_k|^2$), and a remaining set of parameters lumped into ρ'_{FC} . From the last expression, we can see that the FCA effect can be characterized by only one parameter, ρ'_{FC} , dependent on material nonlinearity, cavity properties and the ratio of free carrier lifetime, τ_{FC} , and linear loss Q , Q_o . The last conclusion is interesting even if not entirely surprising – that free carrier loss depends only on the ratio of free carrier lifetime to the cavity photon lifetime, τ_o , where $Q_o \equiv \omega_o \tau_o / 2$. The larger τ_{FC} / Q_o , i.e., $\tau_{\text{FC}} / \tau_o$, the higher the FCA losses.

The simplifications introduced by this normalized model permit us to numerically solve the optimal synthesis problem for an OPO, which does not have a simple analytical solution, and to arrive at solutions that are universal in the sense that they apply across an array of possible designs. The model also provides a simple approach to solving similar problems, if certain restrictions we have applied here are removed. Examples include frequency-mismatched OPO, optical parametric amplifiers and wavelength conversion driven by CW or modulated sources, and parametric spontaneous emission and photon-pair generation.

6.3 Approach to finding the optimum OPO design

Now, we are ready to tackle the “synthesis” problem, i.e. the problem of finding the optimum OPO design given certain material parameters. We define the optimum design of an OPO as the one that, for a given input pump power, provides the maximum output signal (idler) power that

can be generated through FWM, i.e. has maximum conversion efficiency. We define the power conversion efficiency η as

$$\eta \equiv \frac{|S_{s,-}|^2}{|S_{p,+}|^2}. \quad (6.6)$$

For similar photon energies, the maximum efficiency is 50% to each of the signal and idler wavelengths, as two pump photons are converted to one signal and idler photon each (i.e. the maximum photon conversion efficiency is 50%).

To find the optimum design, the first step is to design resonances for the pump, signal and idler wavelengths that have substantial field overlap and satisfy the energy (frequency) and momentum (propagation constant) conservation conditions (the latter automatically holds for resonances with appropriate choices of resonant orders [68]). This has been done successfully in previous work [69, 52]. However, the optimum choice of external coupling and coupled cavity architectures has not been investigated. We address it here, and show that in general unequal waveguide coupling to the pump and signal/idler resonances is the optimum choice, whereas traditional tabletop OPOs typically have equal couplings, as they result from broadband mirrors (unique exceptions include optical parametric chirped pulse amplification which explicitly demands mirrors designed for very different coupling at pump and signal wavelengths [81]).

For continuous-wave operation, we begin by finding the steady state conditions of the system. At steady state ($\frac{dB_k}{dt} = 0$) we have

$$B_s = -2j\rho_{s,\text{tot}}^{-1} B_p^2 B_i^* \quad (6.7)$$

$$B_i = -2j\rho_{i,\text{tot}}^{-1} B_p^2 B_s^* \quad (6.8)$$

$$T_{p,+} = j \frac{\rho_{p,\text{tot}} B_p + 4j B_p^* B_s B_i}{\sqrt{2\rho_{p,\text{ext}}}} \quad (6.9)$$

In the following sections, these conditions will lead to the oscillation threshold, efficiency, optimum couplings and other results. Once the OPO device topology is selected, fixing the topological d -vector, the conversion efficiency in Eq. (6.6) depends only on 5 normalized parameters, $\eta = \eta(\sigma_3, |T_{p,+}|^2, \rho'_{\text{FC}}, \rho_{s,\text{ext}}, \rho_{p,\text{ext}})$. We proceed to find the design $(\rho_{s,\text{ext}}, \rho_{p,\text{ext}})$ with the maximum

efficiency η_{\max} for a given normalized input pump power $|T_{p,+}|^2$, nonlinear loss sine σ_3 , and normalized free carrier lifetime ρ'_{FC} . The conversion efficiency as a function of external coupling is solved at different levels of simplification below, and optimum couplings are chosen for the maximum efficiency designs.

6.3.1 Traveling-wave single-cavity model with pump-assisted TPA only and no FCA

As announced in Section 6.2, throughout Sections 6.3.1–6.3.3 we assume a single, traveling-wave cavity with a traveling-wave excitation. In practice, this means three resonant modes with nearly identical time-average spatial intensity patterns (and this is the case in traveling-wave resonators under our assumption of nearby resonance frequencies, which ensure similar transverse waveguide confinement). In this case, the topological d -vector is (see Section 4.2).

$$d_{\text{ss}} = d_{\text{pp}} = d_{\text{ii}} = d_{\text{sp}} = d_{\text{si}} = d_{\text{ip}} = 1. \quad (6.10)$$

First, we solve a simplified version of our model. We set the nonlinear loss to be dominated by pump-assisted TPA for all three frequencies, and ignore TPA contributions that are much weaker. That is, we drop the d_{ss} , d_{ii} and d_{si} terms from Eqs. (6.3d) and (6.3f), and drop the d_{sp} and d_{ip} terms from Eq. (6.3e). This is valid in the weak conversion regime, relevant to many practical situations, where the generated signal and idler light is much weaker than pump light in the cavity. In our analysis in this section, we solve this model in all regimes including strong conversion and up to full conversion, even though its physics are valid in the weak conversion regime only. For one, this analysis provides a useful bound on conversion efficiency. Then, we also indicate the region of validity for numerical accuracy of the model. In this section we also ignore the loss due to free carrier absorption because it may be effectively reduced by carrier sweep-out using, for example, a reverse biased p-i-n diode [9, 77, 78]. It is revisited later in this chapter.

Thus, the loss rates in Eqs. (6.3d–6.3f) have the simpler form

$$\begin{aligned}\rho_{s,\text{tot}} &= 1 + \rho_{s,\text{ext}} + 4\sigma_3|B_p|^2 \\ \rho_{p,\text{tot}} &= 1 + \rho_{p,\text{ext}} + 2\sigma_3|B_p|^2 \\ \rho_{i,\text{tot}} &= 1 + \rho_{s,\text{ext}} + 4\sigma_3|B_p|^2\end{aligned}\tag{6.11}$$

where signal and idler external coupling are equal, as already discussed. We can find the steady state operating point from Eqs. (6.7) and (6.8), which gives

$$\begin{cases} |B_s|^2 = |B_i|^2 = 0 & \text{(below threshold)} \\ |B_p|^2 = \frac{(1 + \rho_{s,\text{ext}})}{2(1 - 2\sigma_3)} & \text{(above threshold).} \end{cases}\tag{6.12}$$

These two are the classical steady-state solutions to below-threshold and above-threshold operation of the oscillator, respectively. Note that, at least in the present model that considers pump-assisted TPA only, the steady-state pump resonator-mode energy $|B_p|^2$ is independent of both the input pump power $|T_{p,+}|^2$ and the pump external coupling $\rho_{p,\text{ext}}$. This can be interpreted as clamping of the parametric gain. By combining Eq. (6.2a) and Eq. (6.8) we have the lasing equation for signal light

$$\frac{dB_s}{d\tau} = -\rho_{s,\text{tot}}B_s + 4\rho_{i,\text{tot}}^{-1}|B_p|^4B_s \equiv -\rho_{\text{loss}}B_s + \rho_{\text{gain}}B_s\tag{6.13}$$

Both the loss and gain for the signal light depend on the in-cavity pump light energy. When the loss and gain term are equal, we arrive at the expression for $|B_p|^2$ in oscillation [see Eq. (6.12)]. At the same time, the parametric gain also depends on in-cavity signal light energy, which results in gain clamping

$$\frac{dB_p}{d\tau} = -\rho_{p,\text{tot}}B_p - 8\rho_{i,\text{tot}}^{-1}|B_p|^2|B_s|^2B_p - j\sqrt{2\rho_{p,\text{ext}}}T_{p,+}.\tag{6.14}$$

This is analogous to gain clamping in a laser where, during lasing, the gain saturates to equal the round trip loss. Since the total loss rate (field decay rate) of the freely oscillating mode (signal/idler) includes the external (output) coupling and absorption/radiation losses of the signal/idler

resonances only, not those of the pump resonance, it is not surprising that the loss and external coupling of the pump play no role. The parametric gain is proportional to the cavity pump energy, hence it must stay related to the signal/idler decay rates only, i.e. unchanged when the signal/idler rates are fixed. In spite of this result, we will show later in this section that the optimum choice of external coupling (both pump and signal/idler) for maximum conversion efficiency does depend on the input pump power, $|T_{p,+}|^2$, i.e. $|S_{p,+}|^2$.

We next investigate the oscillation threshold. In general, the oscillation threshold will depend on the choice of external couplings $\rho_{p,\text{ext}}$ and $\rho_{s,\text{ext}}$. For now, to provide a useful metric for our model normalization, we will study the threshold when we choose the external couplings that **minimize** the oscillation threshold, i.e. give the minimum (optimum) threshold. This provides a useful and simpler metric that does not depend on couplings. This minimum threshold pump power, $P_{\text{th,min}}$, is derived in Sec. 6.3.3.1. It occurs for an external signal coupling of zero, and an external pump coupling set to the nonlinear equivalent of the critical coupling condition. In the context of the model in this section (without FCA), the minimum threshold is given by

$$P_{\text{th,min}} = \frac{1 - \sigma_3}{(1 - 2\sigma_3)^2} \frac{2r_o^2}{\omega\beta_{\text{fwm}}} = \frac{1 - \sigma_3}{(1 - 2\sigma_3)^2} P_{\text{th,lin,min}} \quad (6.15)$$

where $P_{\text{th,lin,min}} \equiv 2r_o^2/(\omega\beta_{\text{fwm}}) = |S_o|^2$ [see Eq. (6.3c)] is the minimum threshold pump power when nonlinear loss is negligible ($\sigma_3 = 0$), and which we'll call the **linear minimum threshold**. The threshold scales as V_{eff}/Q_o^2 [compare Eq. (6.15) with Eq. (A.10)], where Q_o is the linear loss Q (unloaded quality factor), and V_{eff} is the effective nonlinear mode interaction volume defined in Sec. A.1. The σ_3 -dependent prefactor in (6.15) shows spoiling of the threshold with nonlinear loss, and defines the nonlinear oscillation threshold curve in Fig. 6.2. Note that for each NFOM, or nonlinear loss sine σ_3 , which is largely independent of the geometry, the minimum threshold is fixed by a combination of the loss Q and nonlinear interaction volume. Note also that for $\sigma_3 > 0.5$, the threshold is infinite. This makes sense – the two-photon absorption is larger than the parametric gain at all pump powers.

Now that the minimum (optimum) threshold is established for all σ_3 , we proceed to find the

optimum design at all points above threshold. Our goal is to express the efficiency only in terms of the input pump power, σ_3 , and the external couplings, which we have control over; then to select the optimum couplings. This will produce an optimum design for any point in the two-dimensional space of all possible pump powers, and nonlinear loss sine σ_3 of the material used.

In the steady state, the FWM conversion (pump input to signal output) efficiency η in Eq. (6.6) can be expressed as

$$\eta \equiv \frac{|S_{s,-}|^2}{|S_{p,+}|^2} = \frac{2r_{s,\text{ext}}|A_s|^2}{|S_{p,+}|^2} = \frac{2\rho_{s,\text{ext}}|B_s|^2}{|T_{p,+}|^2}. \quad (6.16)$$

In this expression, $|B_s|^2$ can be replaced with an expression that depends on $|B_p|^2$ and $|T_{p,+}|^2$ using Eqs. (6.8)–(6.9). Then, using Eq. (6.12) we can express η as a function only of the input pump power ($|T_{p,+}|^2$), external couplings ($\rho_{p,\text{ext}}$ and $\rho_{s,\text{ext}}$) and the nonlinear loss sine σ_3 .

Next, the maximum efficiency design is found in two steps, first by maximizing efficiency with respect to pump external coupling, and then with respect to signal external coupling. From $\frac{\partial \eta}{\partial \rho_{p,\text{ext}}} = 0$ we find optimum solution

$$\rho_{p,\text{ext,opt}} = \frac{1 - 2\sigma_3}{1 + \rho_{s,\text{ext}}} |T_{p,+}|^2. \quad (6.17)$$

It is straightforward to verify that this choice of pump coupling $\rho_{p,\text{ext}}$ corresponds to a maximum of η for a given input pump power $|T_{p,+}|^2$ and signal/idler coupling $\rho_{s,\text{ext}}$. We can remove the dependence of η on $\rho_{p,\text{ext}}$ by inserting (6.17) into (6.16). Next, setting the derivative of this new η with respect to $\rho_{s,\text{ext}}$ (for a given $|T_{p,+}|^2$) to zero, we arrive at a cubic equation in $\rho_{s,\text{ext}}$:

$$(1 + \rho_{s,\text{ext}})^2 (2\sigma_3 \rho_{s,\text{ext}} + 1 - \sigma_3) - (1 - 2\sigma_3)^2 |T_{p,+}|^2 = 0.$$

Since the coefficients of this cubic equation are all real, it always has a real root, given by

$$\begin{aligned} \rho_{s,\text{ext,opt}} &= \frac{1}{6\sigma_3} (-1 - 3\sigma_3 + (D - E)^{1/3} + (D + E)^{1/3}) \\ D &\equiv (3\sigma_3 - 1)^3 + 54\sigma_3^2 (1 - 2\sigma_3)^2 |T_{p,+}|^2 \\ E &\equiv 3\sigma_3 (1 - 2\sigma_3) \sqrt{6|T_{p,+}|^2 [(3\sigma_3 - 1)^3 + D]} \end{aligned} \quad (6.18)$$

The above solution is only valid when the input pump power, $S_{p,+}|^2$, is above the minimum threshold power $P_{\text{th,min}}$, which corresponds to the signal coupling $\rho_{\text{s,ext,opt}}$ in Eq. (6.18) (and the efficiency η) taking on positive real values. Again, it can be verified that this solution corresponds to the maximum of η in $\rho_{\text{s,ext,opt}}$ for a given input pump power.

Thus, in Eqs. (6.18) and (6.17) we have found a unique optimum design for a parametric oscillator, in closed form, that achieves maximum efficiency η for a given “lossiness” of the 3rd-order nonlinearity being used, described by material-dependent nonlinear loss sine σ_3 , and a given input pump power, $|S_{p,+}|^2$. The design constitutes a particular choice of pump and signal resonance external coupling, providing an optimum conversion efficiency $\eta_{\text{max}}(|T_{p,+}|^2, \sigma_3) \equiv \eta(|T_{p,+}|^2, \sigma_3, \rho_{\text{p,ext,opt}}, \rho_{\text{s,ext,opt}})$. All other parameters that are included in the normalizations (r_o , S_o and A_o), such as the linear losses, four-wave mixing coefficient, confinement of the optical field, etc., simply scale the solution.

We assume that we can choose couplings freely without affecting other cavity parameters (resonance frequency, loss Q, nonlinear effective volume, etc.) – thereby separating/decoupling the “architecture” (choice of coupled-cavity topology, and coupling between cavities and to waveguide ports) and the building-block “single cavity design” (to optimize parametric gain vs. linear radiation loss, sidewall roughness scattering, etc.). Coupling can introduce coupling-strength-dependent parasitic loss [82, 83], leading to the need to jointly optimize the architecture and cavity design. These higher-order considerations will be visited in future work.

It is noteworthy that the optimum pump and signal/idler resonance coupling values are different, whereas in practice in table-top parametric oscillators they are typically equal when broadband mirrors are used to set external coupling, e.g. in a Fabry-Perot resonator.

We next study this optimum solution in some detail, starting with a few limiting cases.

6.3.1.1 Optimum designs: lossless $\bar{\chi}^{(3)}$ ($\sigma_3 = 0$)

First, we will discuss the limit with no nonlinear loss ($\sigma_3 \rightarrow 0$), and then we will examine the full solution just obtained from the pump-assisted-only TPA model.

For $\sigma_3 = 0$, we find that the optimum couplings are

$$\rho_{s,\text{ext,opt}} = \sqrt{|T_{p,+}|^2 - 1} \quad (6.19)$$

$$\rho_{p,\text{ext,opt}} = \sqrt{|T_{p,+}|^2}. \quad (6.20)$$

This result is consistent with simple physical intuition. If the pump power is near the threshold (but above it), i.e. $|T_{p,+}|^2 = 1 + \epsilon$, $\epsilon \ll 1$, then the amount of signal/idler light generated is small, and we are in the undepleted pump scenario. In this case, the optimum solution is $\rho_{p,\text{ext,opt}} = 1$, i.e. $r_{p,\text{ext,opt}} = r_o$, which means that the pump resonance is critically coupled. Critical coupling maximizes the intra-cavity pump intensity, and hence the parametric gain seen by the signal and idler light. In the case where the pump power is well above threshold, the generated signal/idler light carries significant energy away from the pump resonance (which acts as a virtual gain medium to the signal/idler light). As a result, the pump resonance sees an additional loss mechanism. The pump coupling is then larger to match the linear and nonlinear loss combined to achieve “effective critical coupling”, in which case $\rho_{p,\text{ext,opt}} > 1$ (i.e. $r_{p,\text{ext,opt}} > r_o$). For the signal/idler output coupling, near threshold $\rho_{s,\text{ext,opt}} \approx 0 \ll 1$. Since gain just above threshold exceeds loss by a small amount, the output coupling cannot be large as it would add to the cavity loss and suppress oscillation – hence, the optimal $r_{s,\text{ext}}$ is between zero and a small value there.

In the case of far-above-threshold operation, $\sqrt{|T_{p,+}|^2} \gg 1$, and thus $\rho_{s,\text{ext,opt}} \approx \rho_{p,\text{ext,opt}} = \sqrt{|T_{p,+}|^2}$. This also means that $r_{s,\text{ext,opt}} \approx r_{p,\text{ext,opt}} \gg r_o$, i.e. the output coupling rate is far above the linear-loss rate. In the high-power scenario, the optimum design is then equal coupling. This can be understood by analogy to a linear, 2-resonance (second-order) filter [84]. In our analogy, one resonance is the pump and one the signal resonance, coupled by a nonlinearity. If the pumping is strong, and thus the resonance-resonance coupling is large, there is an effective splitting in the modes beyond the intrinsic linewidth r_o (before the gain is included). With well-resolved resonances, for maximum power transfer from the pump input to signal output, symmetric coupling is optimum [85].

In the lossless nonlinearity regime, the optimum design’s efficiency (i.e. maximum achievable

efficiency) is

$$\eta_{\max}(|T_{p,+}|^2, \sigma_3 = 0) = \frac{(\sqrt{|T_{p,+}|^2} - 1)^2}{2|T_{p,+}|^2} \quad (6.21)$$

for $|T_{p,+}|^2 > 1$ (above threshold). The optimum efficiency together with the corresponding normalized coupling, Eqs. (6.19)–(6.20) provide all of the information needed to design optimum OPOs employing a lossless $\bar{\chi}^{(3)}$ nonlinearity.

The forced equal-coupling case ($\rho_{p,\text{ext}} = \rho_{s,\text{ext}} \equiv \rho_{\text{ext}}$): For device geometries where different external coupling for different resonances are not easily implemented, we can constrain the pump and signal/idler coupling to all be equal, and can still search for the optimum design in this context. For each input pump power, $|T_{p,+}^{(\text{ec})}|^2$, there is an optimum choice of coupling, $\rho_{\text{ext}} = \rho_{\text{ext,opt}}$. Above threshold, this coupling maximizes conversion efficiency. Near threshold, it equivalently minimizes the threshold power. The optimum coupling, $\rho_{\text{ext,opt}}$, is directly related to the pump power by

$$|T_{p,+}^{(\text{ec})}|^2 = \frac{(1 + \rho_{\text{ext,opt}})^3 (1 + 2\rho_{\text{ext,opt}})^2}{\rho_{\text{ext,opt}} (3 + 2\rho_{\text{ext,opt}})^2}. \quad (6.22)$$

The normalized oscillation threshold is $\left[|T_{p,+}^{(\text{ec})}|^2\right]_{\text{th}} = P_{\text{th,min}}/P_{\text{th,lin,min}} = \frac{27}{16}$ (see derivation in Sec. 6.3.3.1), and the corresponding normalized external coupling is given by (6.22) as $\rho_{\text{ext,opt}} = \frac{1}{2}$ at threshold. This result matches the minimum oscillation threshold expression in [68]. The optimum coupling is exactly half way between the optimum values of $\rho_{p,\text{ext,opt}} = 1$ and $\rho_{s,\text{ext,opt}} = 0$ at threshold in the unconstrained couplings case, described earlier in this section. At large pump power, $|T_{p,+}^{(\text{ec})}|^2 \gg 1$, Eq. (6.22) has an asymptotic form for $\rho_{\text{ext,opt}} \sim |T_{p,+}^{(\text{ec})}| - \frac{1}{2}$, which is just the mean value of the optimum couplings in the unconstrained, unequal-couplings case, $\rho_{\text{ext,opt}} = (\rho_{p,\text{ext,opt}} + \rho_{s,\text{ext,opt}})/2$.

6.3.1.2 Optimum designs: with nonlinear loss

Next, we consider the case with non-zero nonlinear loss, $\sigma_3 > 0$. In Fig. 6.2 we plot the maximum efficiency η_{\max} , and corresponding optimum external coupling rates for the pump and

signal/idler, Eqs. (6.17) and (6.18), as a function of the nonlinear loss sine σ_3 and normalized input pump power $|T_{p,+}|^2$. The plots show a few interesting features. First, the linear losses do not limit the maximum conversion efficiency, but rather merely scale the required pump power

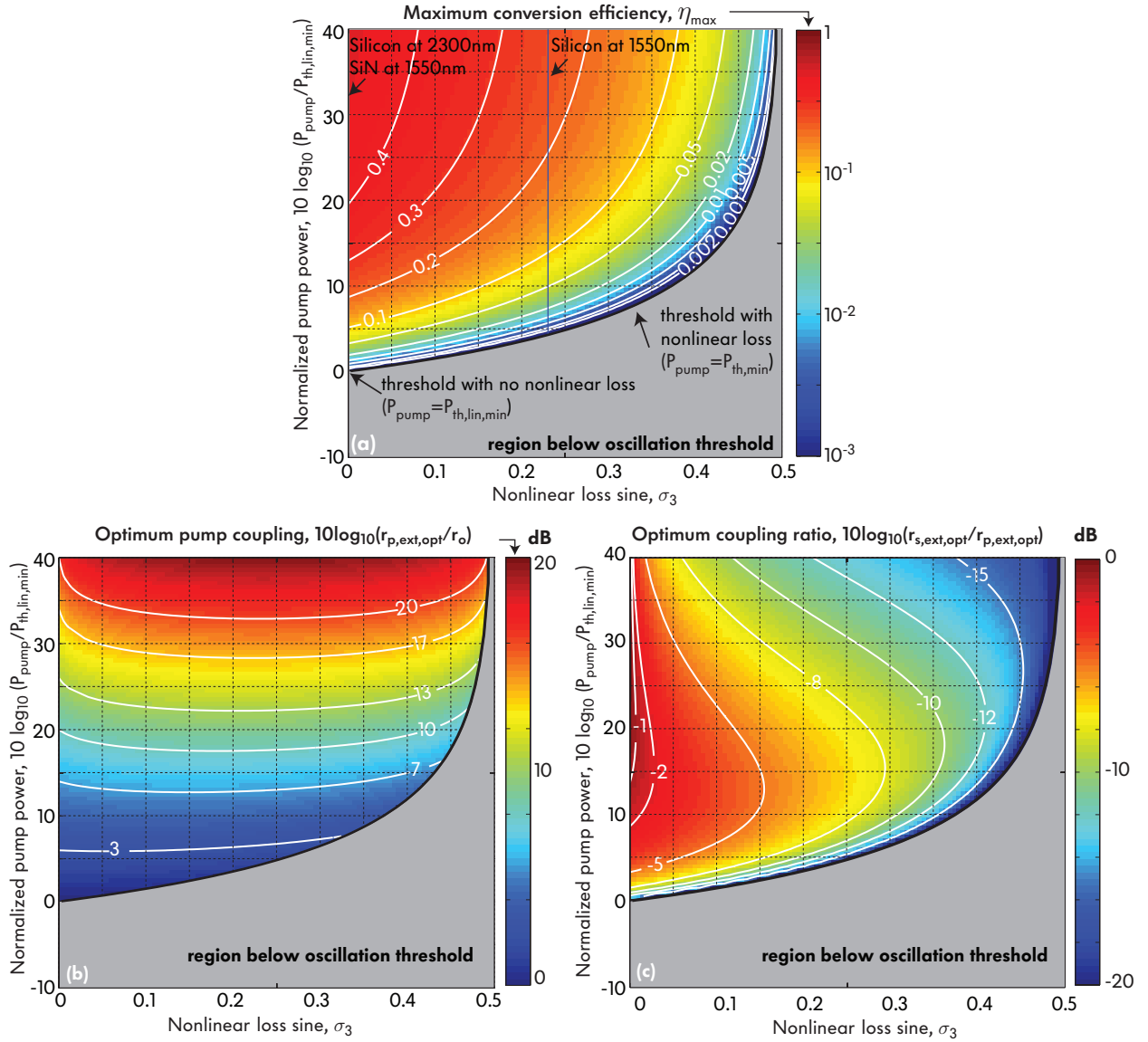


Figure 6.2: Normalized design curves for optimum OPO (using a “partial-TPA” model with pump-assisted TPA terms only and no FCA included): (a) maximum pump-to-signal/idler conversion efficiency versus pump power (normalized by oscillation threshold when loss due to TPA is ignored) and nonlinear loss sine [defined in Eq. (4.11)]; (b) corresponding optimum pump resonance coupling normalized by cavity intrinsic loss; (c) corresponding optimum ratio of signal/idler relative to pump resonance coupling.

and optimum choice of external coupling coefficients. In the lossless nonlinearity case ($\sigma_3 = 0$), 100% conversion ($\eta = 0.5$ to each of the signal and idler) can always be approached with proper design. Second, nonlinear loss σ_3 places an upper limit on the maximum conversion efficiency, increases the threshold, and increases power requirements. Furthermore, oscillation is only possible using nonlinear materials that have $\sigma_3 < 1/2$. Above this value, the two-photon absorption loss always dominates over the parametric gain, making oscillation impossible. Even for $\sigma_3 < 1/2$, the two-photon absorption losses set an upper bound on the maximum achievable conversion efficiency, given as (full derivation in Sec. 6.3.2.2)

$$\eta < \frac{1}{2} - \sigma_3. \quad (6.23)$$

Note that this is not a tight bound because it results from consideration of pump-assisted TPA only, and an analysis using all TPA contributions will further reduce the maximum conversion and can produce a tighter bound. Third, a few qualitative characteristics of optimum designs can be seen from the plots. The optimum pump external coupling is largely independent of the nonlinear loss [see Fig. 6.2(b)]. On the other hand, the ratio of the optimal signal external coupling to the optimal pump external coupling is largely independent of pump power, and scales primarily with the nonlinear loss [see Fig. 6.2(c)].

This model provides useful insight but is numerically accurate for design only for small η or for small σ_3 , as discussed later in Section 6.3.2. For appreciable output powers (and cavity energies of signal and idler light) or a high nonlinear loss material (large σ_3), an accurate model of OPO operation requires accounting of all TPA, including that due to resonant signal and idler light. We consider this more complex model in the next section.

The forced equal-coupling case ($\rho_{p,\text{ext}} = \rho_{s,\text{ext}}$): With nonlinear loss included, the equal-coupling design is again suboptimal. There is a simple expression for the minimum normalized oscillation threshold power, for the optimum choice of equal couplings (see Sec. 6.3.3.1)

$$P_{\text{th},\min}^{(ec)} = \frac{27(1 - \sigma_3)^2}{16(1 - 2\sigma_3)^3} P_{\text{th},\text{lin},\min}. \quad (6.24)$$

This expression for threshold power is valid in the $\sigma_3 = 0$ case with equal coupling, described in Section 6.3.1.1. The optimum choice of coupling at threshold is still $\rho_{p,\text{ext}} = \rho_{s,\text{ext}} \equiv \rho_{\text{ext,opt}} = \frac{1}{2}$.

To further support that the approach presented here gives the largest conversion efficiency for given input pump power, in Fig. 6.3 we compare the FWM conversion efficiency of the optimal design to one with all three resonances at the usual critical coupling condition, $\rho_{s,\text{ext}} = \rho_{p,\text{ext}} = \rho_{i,\text{ext}} = 1$. We also include the case where the couplings are all equal, but are optimized at each value of input power, as calculated above. The plots show that an unequal coupling design indeed always outperforms one with equal couplings. Furthermore, it is clear that the critical coupling condition, though it maximizes intracavity pump power and is reasonably close to the optimum design at low powers, is far from optimal for above threshold, and cannot reach maximum conversion efficiency.

6.3.2 Model with full TPA but no FCA

In this section we generalize the single-cavity, traveling wave model to include full TPA, including that involving only resonant signal/idler light photons. This is the complete TPA model needed for systems in the regime of a lossy $\overline{\chi}^{(3)}$ nonlinearity, with the exception of treatment of FCA, which is deferred to the following section (it is assumed here that the free carrier lifetime can

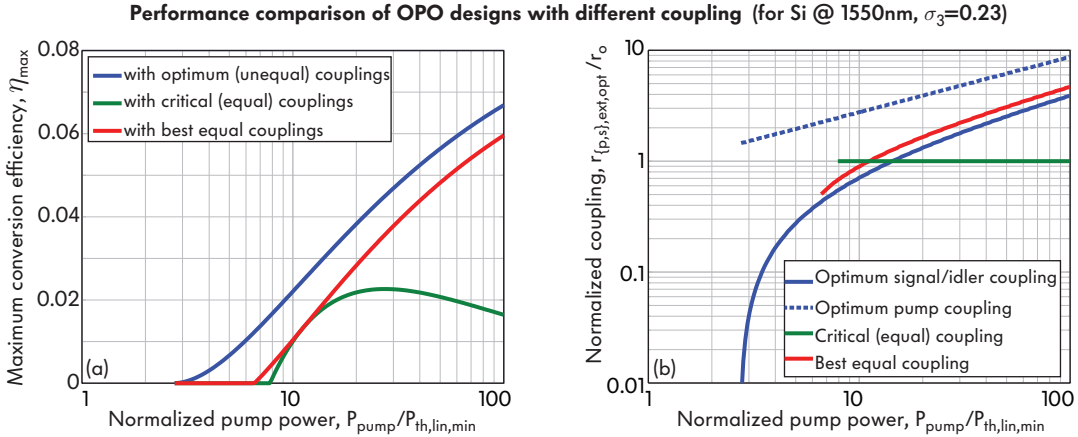


Figure 6.3: Performance comparison of OPO designs with optimum unequal pump and signal/idler couplings and with optimized equal couplings (assuming no FCA): (a) power conversion efficiency; (b) optimum coupling values.

be low enough to not be the limiting loss). The loss rates in Eq. (4.5) have the form

$$\begin{aligned}
\rho_{s,\text{tot}} &= 1 + \rho_{s,\text{ext}} + 2\sigma_3 (|B_s|^2 + 2|B_p|^2 + 2|B_i|^2) \\
\rho_{p,\text{tot}} &= 1 + \rho_{p,\text{ext}} + 2\sigma_3 (2|B_s|^2 + |B_p|^2 + 2|B_i|^2) \\
\rho_{i,\text{tot}} &= 1 + \rho_{s,\text{ext}} + 2\sigma_3 (2|B_s|^2 + 2|B_p|^2 + |B_i|^2)
\end{aligned} \tag{6.25}$$

There is no longer a simple closed-form expression for the in-cavity steady-state pump light energy as we had in Eq. (6.12) for the partial (pump-assisted-only) TPA model. Instead we have

$$|B_p|^2 = \frac{(1 + \rho_{s,\text{ext}} + 6\sigma_3|B_s|^2)}{2(1 - 2\sigma_3)} \tag{6.26}$$

which depends on the in-cavity steady state signal/idler light energy, $|B_s|^2$. It turns out that we need to solve the following cubic equation to find steady-state $|B_s|^2$:

$$\begin{aligned}
4(1 - 2\sigma_3)^3 \rho_{p,\text{ext}} |T_{p,+}|^2 &= (6\sigma_3|B_s|^2 + 1 + \rho_{s,\text{ext}}) \\
&\times [(1 - 2\sigma_3)(1 + \rho_{p,\text{ext}}) + \sigma_3(1 + \rho_{s,\text{ext}}) + 2(2 - 5\sigma_3^2)|B_s|^2]^2
\end{aligned} \tag{6.27}$$

and can only then proceed to find the optimum coupling to maximize conversion efficiency. While it is possible to find an analytical solution for B_s (e.g. with the help of symbolic mathematics software packages [86]), there is no sufficiently simple analytic expression for it, and we have not succeeded in finding manageable closed form expressions for the optimum couplings themselves in this case. Nevertheless, we can numerically sweep across values of the parameters $\rho_{p,\text{ext}}$ and $\rho_{s,\text{ext}}$ to find the maximum conversion efficiency. This is a worthwhile exercise because it is not computationally expensive, yet the problem is normalized, so a single solution set covers the entire design space. In Fig. 6.4(I), we show the normalized design curves for optimum OPO design when all TPA terms are included (but no FCA). We also show a comparison of these two cases – with partial (pump-assisted-only) TPA and full TPA included, separately – in Fig. 6.4(II), to show the region of validity of the simpler partial-TPA model. There is agreement between the partial and full TPA models in efficiency for $\sigma_3 < 0.1$, while the couplings are correct for either pump powers below about 100 times the minimum nonlinear threshold $P_{\text{th,min}}$, or for $\sigma_3 < 0.02$ or so, consistent with our comments in the previous section.

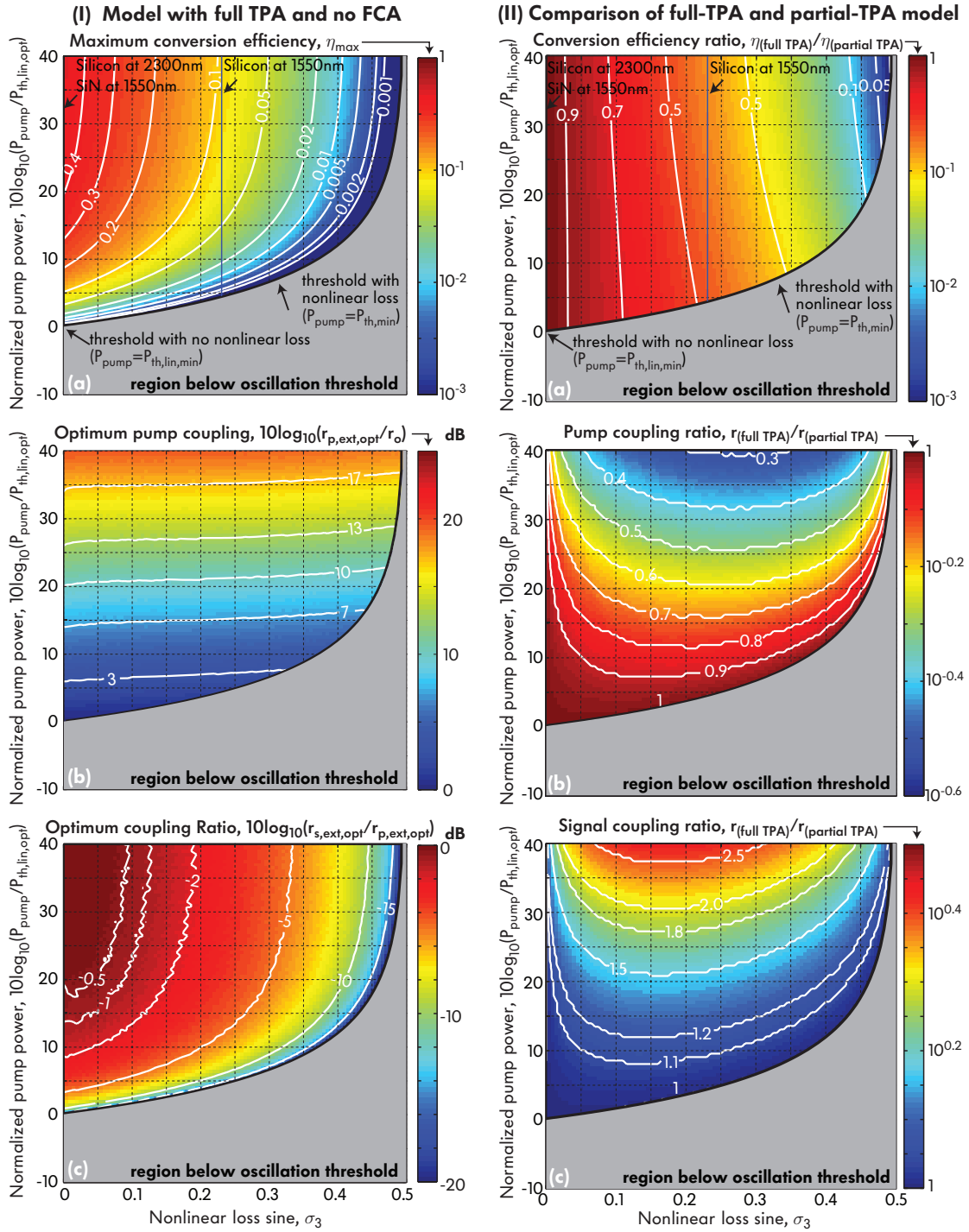


Figure 6.4: Normalized design curves for optimum OPO (I) using a “full-TPA” model (with all TPA terms but no FCA included) and (II) comparison of “partial-TPA” and “full-TPA” models (assuming no FCA): (a) maximum efficiency versus pump power and nonlinear loss sine, and corresponding (b) pump resonance coupling and (c) ratio of signal/idler relative to pump resonance coupling in (I) and signal/idler resonance coupling in (II). See Fig. 6.2 for parameter definitions.

Table 6.1: Predicted performance of optical parametric oscillators based on some common on-chip nonlinear material in a single-ring cavity with traveling-wave mode

Material ^a	$\lambda(\mu\text{m})$	$W(\text{nm}) \times H(\text{nm}) \times R_{\text{out}}(\mu\text{m})^b$	Q_o^c	$V_{\text{eff}}(\mu\text{m}^3)^d$	$\beta_{\text{fwm}}(10^6\text{J}^{-1})$	$P_{\text{th}}(\text{mW})^e$
c-Si	1.55	$460 \times 220 \times 3$	10^6	2.1	29	0.055
c-Si	2.3	$700 \times 250 \times 7$	10^6	10	2.5	0.16
a-Si:H	1.55	$460 \times 220 \times 3$	10^6	2.1	186	0.004
Si_3N_4	1.55	$1600 \times 700 \times 15$	10^6	84	0.22	2.8

^a These materials define waveguide core medium only; all devices use silica cladding ($n = 1.45$) surrounding the waveguide core. Nonlinear parameters from Table 4.1 are used in simulation.

^b The cavity dimensions in this table are not for actual designs (say, dispersion engineering). We just pick some cavity dimensions to estimate the order of magnitude of threshold power. Here W , H , and R_{out} are waveguide core width, height and ring outer radius.

^c Q_o is cavity quality factor due to linear loss only. We assume that $Q_o = 10^6$ for all example designs here.

^d V_{eff} is effective overlap volume of the signal, pump and idler modes, which are three consecutive longitudinal modes of a microring. Here we ignore waveguide dispersion (in propagation constant), which can be designed against, as well as “mode shape dispersion”, i.e. we assume these three modes have nearly identical mode profiles in the transverse direction (a more accurate approximation when the three wavelengths are nearby).

^e Assuming no FCA; for the case with FCA, see Section 6.3.3.

Note that the plots in Figs. 2–6.5 imply a **different** optimum device design for each pump power in the sense that the optimum pump and signal/idler coupling are chosen for each value of input power. In general, for a fixed design, there is an input power which has maximum conversion efficiency, and it is lower at both lower (incomplete conversion) and higher (back-conversion) powers. Hence, the optimum designs provided are in that sense pump-power specific.

6.3.2.1 Example designs and scaling

We next illustrate use of these design curves. We use the normalized optimum solution to derive the optimum performance limitations of a few experimentally relevant systems, including OPOs based on silicon and silicon nitride microcavities. The Kerr (related to parametric gain) and TPA coefficients for crystalline Si and Si_3N_4 are given in Table 6.1. In the telecom band at $1.55\ \mu\text{m}$ wavelength, Si has a large nonlinear loss due to TPA ($\sigma_3 \approx 0.23$ [53]), while Si_3N_4 has negligible TPA ($\sigma_3 \approx 0$) but an order of magnitude smaller Kerr coefficient. Another promising scenario,

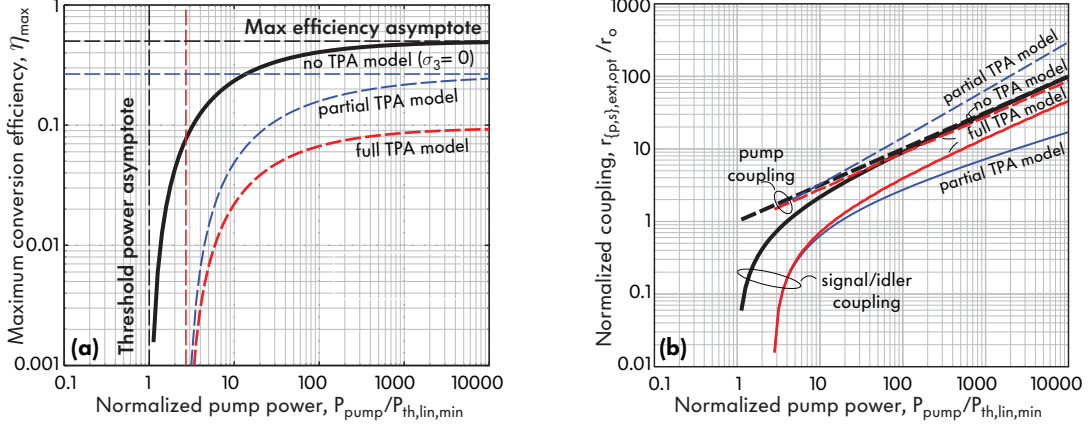


Figure 6.5: Optimum OPO design curves for nonlinear media with and without TPA loss (assuming no FCA), representative of, e.g., of silicon nitride at 1550 nm and Si at $2.3 \mu\text{m}$ (linear), and Si at 1550 nm ($\sigma_3 = 0.23$).

pumping silicon above $\lambda \sim 2.2 \mu\text{m}$ (i.e. photon energy below half the bandgap in silicon), offers both high Kerr coefficient and near zero TPA [33]. Also, hydrogenated amorphous silicon [35] has been shown to have a comparably high NFOM of 2.2 at $\lambda = 1.55 \mu\text{m}$ ($\sigma_3 \approx 0.036$).

In Fig. 6.5, we show slices through Fig. 6.2 and Fig. 6.4(I) showing the still normalized conversion efficiency and corresponding external coupling for optimum designs versus pump power for the 1550 nm silicon design. Comparing the partial and full TPA models here again shows agreement at low powers as expected.

To estimate the conversion efficiency and threshold pump power for these reference designs, and to provide some unnormalized example numbers, we assume some typical microring cavity design parameters, given in Table 6.1, and stick to a single ring cavity design. For example, for a silicon ($n = 3.48$) microring resonant near $\lambda = 1550 \text{ nm}$ with an outer radius of $3 \mu\text{m}$, a $460 \times 220 \text{ nm}^2$ waveguide core cross-section, surrounded by silica ($n = 1.45$), the quality factor of the lowest TE mode due to bending loss is 1.7×10^7 . Considering other linear losses (e.g. sidewall roughness loss), we can assume a total linear loss Q of 10^6 . The effective volume is $2.1 \mu\text{m}^3$, the FWM coefficient is $\beta_{\text{fwm}} \approx 2.9 \times 10^7 \text{ J}^{-1}$, and the minimum linear threshold power, $P_{\text{th,lin,min}}$, is $21 \mu\text{W}$, while the full minimum nonlinear threshold, with no FCA, is $55 \mu\text{W}$ (Table 6.1), and Fig. 6.6,

discussed later, shows the OPO oscillation threshold when FCA is present. Operating below half bandgap allows elimination of two-photon losses, but also requires a larger cavity to control linear radiation loss, leading to a similar order threshold in this comparison. While amorphous silicon [35], due to its higher figure of merit, suggests a much lower threshold in this table, in reality achieving linear loss Q's of 10^6 may not be practical in this material (with measured linear loss of 3.6 dB/cm). And, a:Si-H has been found to degrade over time [35]. Due to its weaker nonlinearity and lower index that leads to weaker confinement, silicon nitride suggests thresholds a couple of orders of magnitude higher than silicon. However, this comparison does not include free carrier losses, discussed in the next section.

6.3.2.2 Upper bound of FWM conversion efficiency

When TPA is the major nonlinear optical loss and FCA is negligible, there is an upper bound of FWM conversion efficiency. From Eqs. (6.8)–(6.9):

$$T_{p,+} = j \left(\sqrt{2\rho_{p,\text{ext}}} \right)^{-1} \left(\rho_{p,\text{tot}} + 8\rho_{i,\text{tot}}^{-1} |B_s|^2 |B_p|^2 \right) B_p = A + B |B_s|^2 \quad (6.28)$$

Where $A \equiv j \left(\sqrt{2\rho_{p,\text{ext}}} \right)^{-1} \rho_{p,\text{tot}} B_p$, $B \equiv j \left(\sqrt{2\rho_{p,\text{ext}}} \right)^{-1} 8\rho_{i,\text{tot}}^{-1} |B_p|^2 B_p$. For the case of pump-only TPA and no FCA, the in-cavity pump light energy has a simple form [see Eq. (6.12)], and thus A and B are independent on the input pump power. The conversion efficiency is

$$\eta = \frac{2\rho_{s,\text{ext}} |B_s|^2}{|T_{p,+}|^2} = \left(\frac{2\rho_{s,\text{ext}}}{B} \right) \frac{T_{p,+} - A}{|T_{p,+}|^2} \quad (6.29)$$

Since the phases of A , B , $T_{p,+}$ are the same, thus

$$\eta = \left(\frac{2\rho_{s,\text{ext}}}{|B|} \right) \frac{|T_{p,+}| - |A|}{|T_{p,+}|^2} \quad (6.30)$$

It's easy to see that η is a function only of the input pump power ($|T_{p,+}|^2$), external coupling ($\rho_{k,\text{ext}}$) and the nonlinear loss sine σ_3 . Now we calculate the maximum conversion efficiency at fixed external coupling from $\frac{\partial \eta}{\partial |T_{p,+}|} = 0$. Then,

$$|T_{p,+}|^2 = 4A^2 = \frac{2\rho_{p,\text{tot}}^2}{\rho_{p,\text{ext}}} |B_p|^2$$

and substituting back into (6.30), the maximum efficiency is

$$\eta_{\max} = \frac{\rho_{s,\text{ext}}}{2AB} = \frac{(1 - 2\sigma_3)^2}{2} \frac{\rho_{s,\text{ext}}\rho_{p,\text{ext}}\rho_{i,\text{tot}}}{\rho_{p,\text{tot}}(1 + \rho_{s,\text{ext}})^2} = \left(\frac{1}{2} - \sigma_3\right) \frac{\rho_{p,\text{ext}}}{\rho_{p,\text{tot}}} \frac{\rho_{s,\text{ext}}(1 + \rho_{i,\text{ext}})}{(1 + \rho_{s,\text{ext}})^2} < \frac{1}{2} - \sigma_3. \quad (6.31)$$

This puts an upper bound on the achievable conversion efficiency (to each of the signal and idler), as a function of the nonlinear loss sine σ_3 .

6.3.3 Model with full TPA and FCA

In a number of $\overline{\chi}^{(3)}$ materials, including silicon, free carrier absorption (FCA) can be a substantial contributor to optical nonlinear losses. Hence our results in Section 6.3.2 that analyze nonlinear (TPA) loss are numerically valid only when FCA can be neglected, which can occur with sufficient carrier sweepout though this requires strong applied electric fields. In general, with no or incomplete carrier sweepout FCA is present, and must be accounted for. In this section, we consider solutions to our complete model, including FCA.

To solve for the steady-state in-cavity signal light energy and therefore calculate and maximize conversion efficiency, one needs to first solve for B_s a system of two coupled equations, cubic in $|B_s|^2$ and $|B_p|^2$, respectively. These are derived from the model in Eqs. (6.2a)–(6.5). The steady-state solution for B_s satisfies

$$\sigma_3\rho'_{\text{FC}}B_p^4 + (8\sigma_3\rho'_{\text{FC}}B_s^2 + 4\sigma_3 - 2)B_p^2 = - (6\sigma_3\rho'_{\text{FC}}B_s^4 + 6\sigma_3B_s^2 + 1 + \rho_{s,\text{ext}}) \quad (6.32)$$

$$[(2 - 2\sigma_3)B_p^2 + (4 + 2\sigma_3)B_s^2 + \rho_{p,\text{ext}} - \rho_{s,\text{ext}}]^2 B_p^2 = 2\rho_{p,\text{ext,opt}}T_{p,+}^2 \quad (6.33)$$

We have found no simple closed-form analytical expression for B_s . In this case, still, one can numerically solve for each B_s and find the optimum coupling for maximum conversion efficiency by sweeping the parameter space. Because the problem is normalized this is still useful to do, computationally inexpensive and provides a great deal of information. As can be noted from Eq. (6.5), the loss due to free carrier absorption (FCA), which affects the efficiency η , scales only with the ratio $\frac{\tau_{\text{FC}}}{Q_o}$, i.e. the ratio of free carrier lifetime to cavity photon lifetime. This again simplifies exploration of the design space.

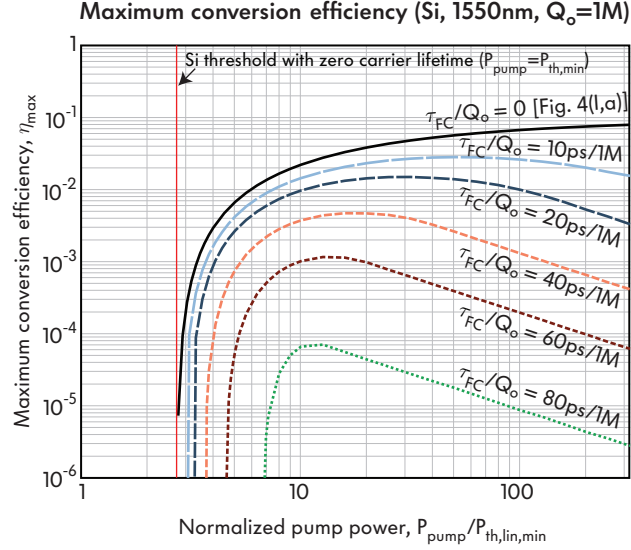


Figure 6.6: Performance of silicon microcavity at 1550 nm resonance with various free-carrier lifetime and intrinsic cavity quality factors.

In Fig. 6.6, we show simulation results for the silicon microcavity at 1550 nm in Table 6.1 with an example set of free carrier lifetimes and cavity loss Q values. The plot shows that, with FCA present, the optimum design's conversion efficiency, η_{\max} , does not monotonically increase with input pump power, as was the case with all of the models in the previous sections (a simple explanation is provided in Sec. 6.3.3.2). This is because a stronger pump produces a larger steady-state carrier concentration generated by TPA and, as a result, the overall FCA and total cavity loss is higher at higher pump power. In fact, the free carrier loss increases faster (quadratically with pump power) than the parametric gain (linearly with pump power), leading to falling conversion efficiency with increasing pump power. Figure 6.6 also shows, however, that even silicon OPOs at 1550 nm, where TPA and FCA work against the nonlinear conversion process, can achieve conversion efficiencies of 0.1% with a pump power of 0.21 mW and free carrier lifetime of 60 ps, which is well within the achievable using carrier sweepout via e.g. a reverse biased p-i-n diode integrated in the optical microcavity [78]. These results and model provide some guidance for future work on efficient implementations of silicon OPOs at 1550 nm, where TPA and FCA are important.

6.3.3.1 Oscillation threshold

Although the optimum design is not provided in closed form for the model that includes full TPA and FCA, we can derive a closed form expression for the minimum oscillation threshold, which is now different, while it was the same in all previous sections (see Eq. (6.15)). From Eqs. (6.8)–(6.9):

$$T_{p,+} = j \left(\sqrt{2\rho_{p,\text{ext}}} \right)^{-1} \left(\rho_{p,\text{tot}} + 8\rho_{i,\text{tot}}^{-1} |B_s|^2 |B_p|^2 \right) B_p. \quad (6.34)$$

When the input pump power is just above threshold, the OPO starts lasing, $|B_s|^2 \approx 0$, and thus

$$|T_{p,+}|^2 = \frac{\rho_{p,\text{tot}}^2}{2\rho_{p,\text{ext}}} |B_p|^2 \quad (6.35)$$

The threshold pump power is the smallest pump power that can make the OPO oscillate. To minimize threshold, we can choose external coupling for pump, signal and idler to minimize the expression for pump power above [see Eq. (6.35)]. The pump power is minimized at

$$\rho_{p,\text{ext}} = 1 + 2\sigma_3 |B_p|^2 + \sigma_3 \rho'_{\text{FC}} |B_p|^4 \quad (6.36)$$

and

$$P_{\text{th}} = \left(2(1 + 2\sigma_3 |B_p|^2 + \sigma_3 \rho'_{\text{FC}} |B_p|^4) |B_p|^2 \right)_{\min} \quad (6.37)$$

So we need to minimize $|B_p|^2$. From Eqs. (6.7) and (6.8)

$$2|B_p|^2 = \rho_{s,\text{tot}} = 1 + \rho_{s,\text{ext}} + 4\sigma_3 |B_p|^2 + \sigma_3 \rho'_{\text{FC}} |B_p|^4 \quad (6.38)$$

By solving this quadratic equation, we have the smaller root:

$$|B_p|^2 = \frac{(1 - 2\sigma_3) - \sqrt{(1 - 2\sigma_3)^2 - \sigma_3 \rho'_{\text{FC}} (1 + \rho_{s,\text{ext}})}}{\sigma_3 \rho'_{\text{FC}}} \quad (6.39)$$

To minimize $|B_p|^2$, we have $\rho_{s,\text{ext}} = 0$. And there is an upper limit of normalized FCA loss for OPO to oscillate:

$$\rho'_{\text{FC}} \leq \frac{(1 - 2\sigma_3)^2}{\sigma_3} \quad (6.40)$$

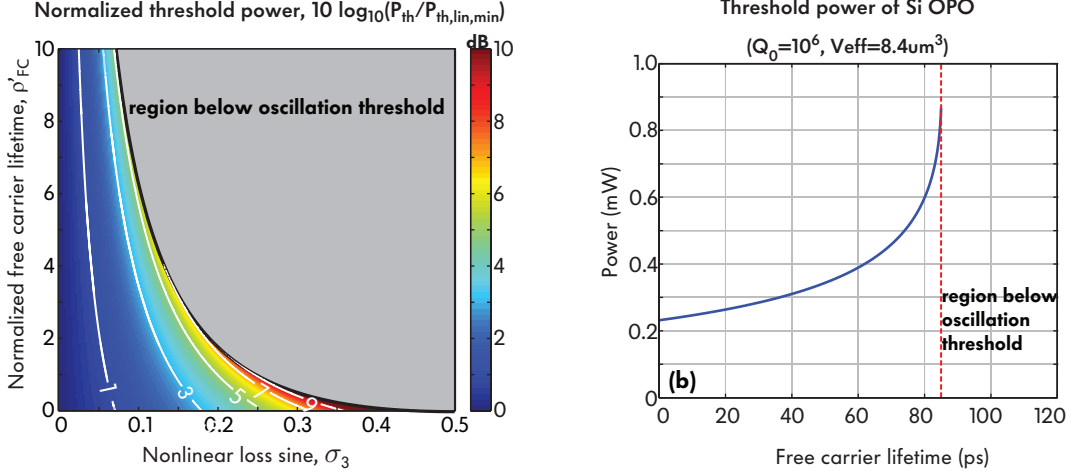


Figure 6.7: The OPO threshold vs (a) normalized free carrier lifetime and σ_3 ; (b) free carrier lifetime for silicon cavity resonant near 1550 nm with linear unloaded Q of 10^6 and effective volume of $8.4 \mu m^3$.

By putting Eq. (6.39) into Eq. (6.37) we have the threshold pump

$$P_{th} = \frac{4(1 - \sigma_3)}{((1 - 2\sigma_3) + \sqrt{(1 - 2\sigma_3)^2 - \sigma_3 \rho'_{FC}})^2} \quad (6.41)$$

which is normalized to $P_{th,lin,min}$. It is easy to prove that in the no FCA loss limit ($\rho'_{FC} \rightarrow 0$), the threshold pump power simplifies to Eq. (6.15). The minimum threshold pump power depends on only the nonlinear loss sine σ_3 , and normalized free-carrier-lifetime, ρ'_{FC} [see Eq. (6.5)]. It is consistent with the simulation results in Fig. 6.6. This choice of external coupling makes sense, as it corresponds to maximum parametric gain (the largest in-cavity pump light energy for given input pump power) and the smallest loss rate for the signal and idler light.

In Fig. 6.7(a), we plot the minimum OPO threshold versus the nonlinear loss sine σ_3 and normalized free-carrier lifetime ρ'_{FC} . We also plot the minimum OPO threshold for a silicon cavity near 1550 nm versus actual free carrier lifetime in Fig. 6.7(b), showing that there is a free-carrier lifetime above which oscillation is not possible at any pump power. We expect this general result for oscillation threshold to also be a useful tool for efficient design of integrated photonic OPOs.

For the case of equal pump and signal/idler coupling ($\rho_{p,ext} = \rho_{s,ext} = \rho_{ext}$), Eqs. (6.35) and

(6.38) can be combined to give:

$$|T_{p,+}|^2 = \frac{\rho_{p,\text{tot}}^3}{4(1-\sigma_3)\rho_{\text{ext}}} \quad (6.42)$$

where $\rho_{\text{ext}} = \rho_{p,\text{tot}} - 1 - 2\sigma_3|B_p|^2 - \rho'_{\text{FC}}|B_p|^4$, $|B_p|^2 = \frac{\rho_{s,\text{tot}}}{2} = \frac{\rho_{p,\text{tot}}}{2-2\sigma_3}$ and then the threshold pump power can be represented by a function of ρ_{ext} . This expression is complex, but can be simplified when FCA is negligible:

$$P'_{\text{th}} = \frac{(1-\sigma_3)^2}{4(1-2\sigma_3)^3} \frac{(1+\rho_{\text{ext}})^3}{\rho_{\text{ext}}} \Big|_{\text{min}} = \frac{27(1-\sigma_3)^2}{16(1-2\sigma_3)^3} \quad (6.43)$$

with $\rho_{\text{ext}} = 1/2$ at threshold.

6.3.3.2 Understanding of oscillation threshold

Here we provide a physical interpretation of the oscillation threshold when both linear and nonlinear loss are present. Figure 6.8 shows the various terms of small-signal gain and loss for the signal resonance in an optical parametric oscillator based on degenerate four wave mixing. The linear loss rate, including material absorption, scattering loss, radiation loss and external coupling etc., is independent of the in-cavity pump energy, which roughly scales with input pump power. The parametric gain from four wave mixing, and loss due to two-photon absorption, are both proportional to pump energy. However, their scaling factors vary by a factor of $2\sigma_3$, thus it is only possible to achieve oscillation for a nonlinear material with $\sigma_3 < 0.5$.

The loss due to free carrier absorption scales with the square of the pump energy, shown as parabolic curve in Fig. 6.8. When the loss due to free carrier absorption is negligible, the total net gain is greater than 0 in region 1. As the effective free carrier lifetime increases, the parabolic curve becomes steeper, and the region of positive net gain shrinks to region 2 and region 3. When the free carrier lifetime is above a certain limit, the total net gain is always negative, no matter how large the pump light energy is. This is consistent with the plot of oscillation threshold in Fig. 6.7.

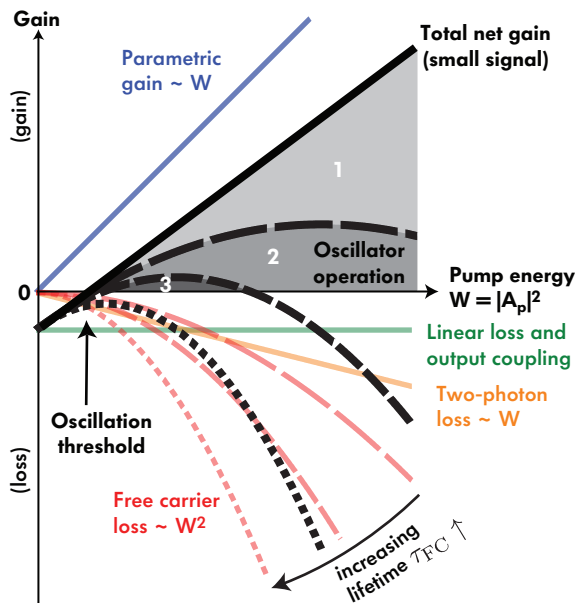


Figure 6.8: Small signal gain and loss in an optical parametric oscillator based on degenerate four wave mixing.

6.4 Extension of analysis to coupled-cavity systems with distributed resonance modes

In the introduction, coupled-mode theory model and general approach for optimum OPO design (Sections 6.1–6.3), we allowed for general mode and excitation configurations. However, in our quantitative analysis thus far, in Sections 6.3.1–6.3.3, for simplicity we chose a single-cavity traveling-wave resonant mode system, e.g. a microring resonator excited in traveling-wave mode. That analysis is strictly valid if dispersion is such that conversion to resonances adjacent to the pump resonance dominates, i.e. if the system is effectively a three resonance system, but the primary purpose is to illustrate the major parameters that influence the efficiency, optimal choices in design, and performance scaling. In this section, we address more general resonator configurations, such as that proposed in Fig. 6.1(c), and the degrees of freedom made available through engineering of coupled-cavity compound resonators and of wavelength or mode selective coupling.

First, a triple-cavity resonator such as that in Fig. 6.1(c) is one example of a resonator that explicitly provides only 3 resonant modes near each longitudinal resonance of the constituent

microring cavities (see Sec. 2.3.1). The wavelength spacing of these resonances is determined by ring-ring coupling strength, via the coupling gap [79, 2]. If the dispersion in the building-block microring cavity is sufficiently large, adjacent longitudinal resonances that are spaced 1 free spectral range (FSR) from the utilized resonance will not have proper frequency matching and will not exhibit substantial FWM as a result. Thus, the nonlinear optics can be confined to the “local” three resonances formed by ring coupling at one longitudinal order.

Next, optimum design of OPO demands different external coupling to the signal (idler) and pump resonances. Compound resonator designs can also provide substantial freedom in engineering of mode-selective coupling to the bus waveguide(s), as exemplified by the triple-cavity resonator in Sec. 2.3.1. A single-ring cavity can have wavelength-selective coupling, e.g. using a Mach-Zehnder, two-point coupler [87]. However, mode interferometry and orthogonal excitation can provide substantial control of coupling in compound resonators, such as that in Fig. 6.1(c). As Fig. 2.5 shows, the triple-cavity resonator can be engineered so that the pump resonance is coupled to only the top waveguide, and the signal/idler resonances only to the bottom waveguide. The waveguide-resonator coupling gap in each case determines the corresponding linewidth, allowing different pump and signal/idler couplings to be implemented, as is required (as shown in earlier sections) to achieve an optimal design. Besides, in the linear regime, the top and bottom waveguides are entirely uncoupled, and the only energy coupling from the top to the bottom waveguide can come from nonlinear interaction. One useful feature is that this design automatically filters the pump. In practice, with fabrication variations and loss, we would expect 10-20 dB rejection of the pump to be readily achievable, instead of complete decoupling, but this can still provide a useful function in parametric oscillators.

Last, we show how these geometries can be simply included in our analysis formalism, through the topological d -vector defined in Eq. 6.4 as the relative magnitudes of two-photon absorption and four-wave mixing. Specifically, the simple d -vector given in Eq. 6.10 for a travelling-wave single-cavity resonator is replaced with a general d -vector unique to a given cavity geometry. For example, the topological d -vectors for a triple-ring resonator with travelling-wave and standing-

Table 6.2: Predicted performance of optical parametric oscillators based on 3-ring photonic molecule with traveling-wave mode

Material	$\lambda(\mu\text{m})$	$V_{\text{eff}}(\mu\text{m}^3)^a$	$\beta_{\text{fwm}}(10^6\text{J}^{-1})$	$P_{\text{th}}(\text{mW})$
c-Si	1.55	8.3	7.2	0.29
c-Si	2.3	40	0.63	0.65
a-Si:H	1.55	8.3	46	0.015
Si_3N_4	1.55	337	0.05	11

^a Each constituent ring of the triple-ring cavity is identical to the single-ring cavity in Table 6.1.

wave excitations are summarized in Table 4.2. Then one can follow the same analysis procedure in Sections 6.3.1–6.3.3, to find out the optimum couplings, maximum efficiency and oscillation threshold for OPO in an arbitrary microcavity. This allows a generalized approach to design, that produces a normalized optimal solution for each unique geometry subspace with a given d -vector and material NFOM. Table 6.2 shows the results of Table 6.1 evaluated for a triply-coupled cavity “photonic molecule” OPO with traveling-wave excitation, based on the same ring cavity design in each case.

To summarize this section, higher-order resonator designs can provide both unique functionality, and access to degrees of freedom needed to produce an optimum design. The model presented provides a normalized solution vs. normalized pump power (that includes linear losses), nonlinear FOM σ_3 and a normalized FCA, for each resonator “topology” with a unique d -vector. This should provide a basis for exploring efficient device designs and novel applications.

6.5 Future work and conclusion

The purpose of this chapter was to lay the theoretical foundation for designing efficient parametric oscillators, and for considering the degrees of freedom made available in design by complex photonic structures such as coupled-cavity resonators. A number of details will play an important role in determining the practical utility of these designs. For example, we have here

assumed that ring-ring coupling is lossless. In practice, couplers exhibit radiation loss [82, 83] and will limit the performance of coupled-cavity designs for FWM. Design details such as this will be specific to particular implementations, and are left for future study.

Furthermore, we considered the optimal case here with perfect frequency matching. In an experimental situation, a frequency mismatch must be admitted, and this requires only a simple modification of the presented model.

More generally, the degrees of freedom available in coupled resonant structures on chip suggest that complex synthesis and designs will enable either optimal designs or ones with unique capability for other applications, such as parametric amplifiers and entangled photon sources, including design of joint spectral and temporal distribution of the bi-photons, their coincidence properties, etc.

To conclude, the results in this chapter show that efficient micro-OPOs can be designed in the presence of only linear losses, and even with limited nonlinear losses, as well as free carrier absorption. Notably, while devices without TPA call for equal optimum external coupling to all three resonances when the pump is far above threshold, we show that both in the case closer to the threshold, and in the case with substantial nonlinear losses, it is necessary to design substantially different signal/idler, and pump resonance external coupling for optimum performance. In the case where nonlinear losses are present, we have shown that a large set of practical cases can be solved by considering only pump-induced TPA. In this case, we provide an analytical solution to the design. With full (pump and signal/idler induced) TPA, and with FCA loss included, more complex models do not admit simple closed-form solutions. However, we provide a normalized set of design equations, based on which we can numerically solve for the optimum design, and provide a single set of normalized design plots relevant for design using all nonlinear materials, linear cavity losses, and pump powers.

These results have also motivated our proposal of both spatial mode and Q engineered multimode resonators, based on multiple coupled cavities, for nonlinear FWM applications [2]. The requirements of an optimum OPO design presented here, primarily the different external coupling for pump and signal/idler resonances suggested by the results, do not fit well with a simple linear

cavity such as a Fabry-Perot resonator, or a microring cavity, with broadband coupling to an external excitation port (via a mirror, or directional coupler, respectively). Yet, such designs have been common in tabletop OPOs [50] as well as on-chip OPOs in silicon and silicon nitride [52, 68]. We believe this analysis suggests further work on more advanced geometries (such as Fig. 6.1(c)) may enable more efficient designs, and may enable one to reach the performance bounds found in this chapter.

This work also suggests that complex photonic circuits may provide useful solutions not only for OPOs but also for other devices including parametric amplifiers and entangled photon sources. A large amount of research was done in the early to mid 1900's in electrical circuit linear filter synthesis using resistors, capacitors and inductors, leading to a body of sophisticated linear filter design techniques. Development of synthesis of nonlinear circuits based on resonators as building block components may yield a similarly rich array of solutions to nonlinear optics design on chip.

Chapter 7

Conclusion

7.1 Summary of major achievements

In the past decade there has been an expedited development in the field of silicon photonics. Linear integrated optical elements, such as optical filters, modulators, detectors, fiber-to-chip grating couplers, waveguide crossing and splitting structures, have been extensively studied and are being implemented in mass production. Integrated nonlinear devices, which would enable on-chip coherent light source, optical signal amplification and regeneration, all-optical logic circuits as well as quantum light sources and circuits, have been demonstrated in optical waveguides and single-cavity resonators. The work in this thesis focuses on improving the efficiency and functionality of integrated nonlinear devices, by utilizing the complex mode structures in coupled-cavity resonators, improving the effective nonlinear figure of merit of integrated waveguiding materials with fabrication optimization, and studying the fundamental nonlinear efficiency limit from first principles. It also includes experimental demonstration of optical parametric wavelength conversion in proposed novel coupled-cavity resonators, and shows optimum design of optical parametric oscillators (OPOs) with mode-dependent couplings.

Triple-cavity resonators were proposed for building efficient integrated nonlinear devices based on degenerate four-wave mixing. The three coupled resonance modes can be readily engineered to have equal frequency spacing, allowing for arbitrary choices of resonance frequencies and enhanced nonlinear efficiency (by reducing cavity size) without constraint of dispersion in microresonators. The linewidth of these three coupled modes can also be independently controlled by selective

coupling to external bus waveguides, enabling optimum design of many nonlinear devices including optical parametric oscillators and wavelength converters with easy filtering of stronger pump light out of the generated weaker output light.

The applicability of using hydrogenated amorphous silicon (a-Si:H) in integrated nonlinear optical devices was investigated. A maximum effective nonlinear figure of merit (FOM) of only 0.05 was measured in fabricated a-Si:H samples as a result of substantial non-instantaneous, nonlinear absorption. Such a small FOM in a-Si:H limits its usage in nonlinear devices employing continuous-wave pump light. However, a-Si:H is a promising nonlinear waveguiding material for integrated nonlinear applications where short pump light pulse is used (e.g., ultrafast all-optical switching). An effective nonlinear FOM of approximately 20 was measured for a pump pulse with 0.5 nm FWHM bandwidth.

Besides the nonlinear material, the mode structure of a microscopic device also affects its overall nonlinearity. The nonlinear interaction coefficients in microresonators were derived based on coupled-mode theory, and their relative magnitudes were shown to depend on the spatial overlap of interacting modes. Therefore, a FOM vector was introduced to fully calibrate the third-order optical nonlinearity in a microcavity where the signal, pump and idler resonance have distinct spatial modes. As an example, the nonlinear FOM in a microring resonator with standing-wave excitation is generally smaller than that in the same cavity with travelling-wave excitation.

Parametric wavelength conversion in silicon triple-ring resonators was experimentally demonstrated, with a measured pump-normalized conversion efficiency (i.e., ratio of conversion rate versus the square of on-chip pump light power) of $8 \times 10^{-7} (\text{mW})^{-2}$ without removing free carriers. The compound mode structures with equal frequency spacing and selective couplings to external waveguides were also confirmed experimentally. These results paved the road to more advanced nonlinear devices in coupled-cavity resonators.

The efficiency in an integrated optical parametric oscillator based on degenerate four-wave mixing is maximized by choosing different external coupling rates for the pump and signal/idler resonances, which can be readily achieved in triple-cavity resonators. Specifically, the pump resonance

demands effective critical coupling to maximize in-cavity parametric gain, while the signal/idler resonance prefers under coupling to reduce round-trip loss for efficient oscillation. Universal design curves of optimum couplings for maximum oscillation efficiency were presented, and the results are applicable to integrated OPOs built on arbitrary nonlinear material and resonator mode structures. Analytical expression of the oscillation threshold was also derived with the nonlinear two-photon absorption and free-carrier absorption effects included. For example, parametric oscillation is in-principle possible in micro-resonators made of crystalline silicon, provided that the free carrier lifetime is much smaller than the cavity photon lifetime.

7.2 Remaining challenges and future work

There are still a few challenges that can be done to further improve the performances of integrated nonlinear devices based on coupled-cavity resonator systems. These include better control of the complex mode structure of triple-cavity resonators, further enhancing the stimulated four-wave mixing wavelength conversion efficiency, demonstration of optical parametric oscillators in triple-cavity resonators made of nonlinear materials with large nonlinear figure of merit (such as silicon nitride), and employing this novel resonator system in other classical and quantum optical applications.

Coupled-cavity resonators consisting of three identical cavities in series have equally-spaced resonance frequencies in theory, however, fabricated devices tend to have non-ideal, asymmetric compound modes, as a result of fabrication imperfection and coupling-induced-frequency-splitting. To overcome this limitation, one can shift the resonance frequency of the middle cavity in design, or/and thermally tune the individual cavities post-fabrication. In either case, a systematic way of control is desired. And in general, the middle cavity can have different shape/size from the outer two cavities, as long as the three coupled cavities are simultaneously resonant at the interested wavelength. This new structure can not only make it easier to individually address each constituent cavity, but also allow for extra degree of freedom in designing low-loss cavity-cavity couplers which can dominate cavity loss when strong cavity-cavity coupling (for large resonance frequency splitting)

is required. The two outer resonant modes can be engineered to couple differently to external bus waveguides, by introducing a third bus waveguide coupled directly to two of the three cavities.

Although the non-instantaneous absorption in hydrogenated amorphous silicon samples were experimentally observed, the physical origin of this delayed nonlinear absorption has not been well understood. In addition, different research groups have reported different nonlinear properties in their a-Si:H samples fabricated in different conditions. It is therefore worthwhile to further investigate the underlying mechanism of optical nonlinearity in a-Si:H as well as its dependence on fabrication conditions.

The efficiency of parametric wavelength conversion in triple-cavity resonators can be greatly enhanced by exciting the pump and signal resonances from their preferred coupling buses rather than a common bus as demonstrated in the experiment in Chapter 5. This can be done by coupling the pump and signal light onto the two bus waveguides via two separate grating couplers. With a better fabrication process, the linear cavity loss can be reduced and the efficiency increases for given pump power. By varying the geometric gaps between the cavities and bus waveguides, critical coupling for all three interacting light (i.e., pump, signal and idler) can be realized to maximize cavity enhancement effect.

Once there is enough parametric gain in the resonator, it is then interesting to find optimum designs of optical parametric amplifiers (OPAs) for maximum amplification factor at a certain signal light bandwidth. As the pump light gets depleted and the signal light gets amplified, the optimum external coupling rates to them would be different from the intrinsic cavity loss rate, and favor an effective critical coupling state where the parametric gain and loss rate is considered (by analogy with optimum design of optical parametric oscillators). These optimum couplings would be different for the pump and signal light. Therefore it is advantageous to implement such OPAs in triple-cavity resonators compared to single-cavity resonators with equal linewidth for all resonance modes. Moreover, since large optical power is circulating in the resonators of OPAs, active free-carrier sweepout circuits [9, 78] need to be implemented in devices made of absorptive nonlinear materials .

To enable integrated coherent light source, optical parametric oscillators based on triple-cavity resonators can be fabricated on-chip using the optimum design approach presented in Chapter 6. It is also interesting to extend the theory to cases of different external couplings of the signal and idler resonances. And it can be generalized to cases of multiple oscillating modes where the parametric gain (originally provided by the pump light) is passed to other resonances in a cascaded way. Such oscillators of many oscillating modes can be designed for integrated optical combs with much higher repetition rate than those built on macroscopic resonators. One way to implement OPOs with multiple equally-spaced resonances is to use multiple-coupled cavities with carefully designed individual cavity resonance frequencies and inter-cavity couplings [88].

More integrated nonlinear devices can be built on the triple-cavity resonator systems made of nonlinear waveguide materials. For example, when operated under oscillation threshold, they can be employed to generate quantum photon pairs with strong input pump light and weak generated photons in separate bus waveguides, enabling a multitude of integrated quantum optical applications [7]. The separation of strong pump and weak signal also mitigates the requirement of on-chip filters in other nonlinear optical devices such as all-optical switches and logic gates. In addition, with the capability of independent linewidth control of the three compound resonances in triple-cavity resonators, incoherent light of large bandwidth near one resonance frequency can be parametrically converted to another resonant mode with much narrow linewidth (i.e., longer time coherence) [56].

Bibliography

- [1] X. Zeng and M. A. Popović, “Design of triply-resonant microphotonic parametric oscillators based on Kerr nonlinearity,” Optics Express, vol. 22, no. 13, p. 15837, 2014.
- [2] X. Zeng and M. A. Popović, “Optimum micro-optical parametric oscillators based on third-order nonlinearity,” Conference on Lasers and Electro-Optics (CLEO), vol. 17, no. 30230080, p. CTh1F.7, 2013.
- [3] Y. Liu, J. M. Shainline, X. Zeng, and M. A. Popović, “Ultra-low-loss CMOS-compatible waveguide crossing arrays based on multimode Bloch waves and imaginary coupling.,” Optics letters, vol. 39, no. 2, pp. 335–8, 2014.
- [4] M. T. Wade, X. Zeng, and M. A. Popović, “Wavelength conversion in modulated coupled-resonator systems and their design via an equivalent linear filter representation.,” Optics letters, vol. 40, no. 1, pp. 107–10, 2015.
- [5] F. Pavanello, X. Zeng, M. T. Wade, and M. A. Popović, “Ring modulators in standing-wave and partial standing wave operation on a matched interdigitated p-n junction for enhanced efficiency,” no. c, pp. 4–5, 2015.
- [6] C. M. Gentry and M. A. Popović, “Dark state lasers,” Optics Letters, vol. 39, no. 14, p. 4136, 2014.
- [7] C. M. Gentry, J. M. Shainline, M. T. Wade, M. J. Stevens, S. D. Dyer, X. Zeng, F. Pavanello, T. Gerrits, S. W. Nam, R. P. Mirin, and M. A. Popović, “Quantum-correlated photon pairs generated in a commercial 45 nm complementary metal-oxide semiconductor microelectronic chip,” Optica, vol. 2, no. 12, p. 1065, 2015.
- [8] C. V. Poulton, X. Zeng, M. T. Wade, J. M. Shainline, J. S. Orcutt, and M. A. Popović, “Photonic Crystal Microcavities in a Microelectronics 45-nm SOI CMOS Technology,” IEEE Photonics Technology Letters, vol. 27, no. 6, pp. 665–668, 2015.
- [9] H. Rong, R. Jones, A. Liu, O. Cohen, D. Hak, A. Fang, and M. Paniccia, “A continuous-wave raman silicon laser,” Nature, vol. 433, pp. 725–728, feb 2005.
- [10] A. G. Griffith, R. K. Lau, J. Cardenas, Y. Okawachi, A. Mohanty, R. Fain, Y. H. D. Lee, M. Yu, C. T. Phare, C. B. Poitras, A. L. Gaeta, and M. Lipson, “Silicon-chip mid-infrared frequency comb generation,” Nature Communications, vol. 6, p. 6299, 2015.

- [11] J. S. Pelc, K. Rivoire, S. Vo, C. Santori, D. A. Fattal, and R. G. Beausoleil, "Picosecond all-optical switching in hydrogenated amorphous silicon microring resonators.," Optics express, vol. 22, no. 4, pp. 3797–810, 2014.
- [12] M. Khorasaninejad and S. S. Saini, "All-optical logic gates using nonlinear effects in silicon-on-insulator waveguides.," Applied optics, vol. 48, no. 25, pp. F32–7, 2009.
- [13] J. Bravo-Abad, E. P. Ippen, and M. Soljacic, "Ultrafast photodetection in an all-silicon chip enabled by two-photon absorption," Applied Physics Letters, vol. 94, no. 24, p. 241103, 2009.
- [14] A. C. Turner, M. a. Foster, A. L. Gaeta, and M. Lipson, "Ultra-low power parametric frequency conversion in a silicon microring resonator.," Optics express, vol. 16, no. 7, pp. 4881–4887, 2008.
- [15] A. C. Turner, C. Manolatou, B. S. Schmidt, M. Lipson, M. a. Foster, J. E. Sharping, and A. L. Gaeta, "Tailored anomalous group-velocity dispersion in silicon channel waveguides.," Optics express, vol. 14, pp. 4357–62, may 2006.
- [16] P. Del'Haye, A. Schliesser, O. Arcizet, T. Wilken, R. Holzwarth, and T. J. Kippenberg, "Optical frequency comb generation from a monolithic microresonator," Nature, vol. 450, no. 7173, pp. 1214–1217, 2007.
- [17] M. A. Foster, J. S. Levy, O. Kuzucu, K. Saha, M. Lipson, A. L. Gaeta, Mark A. Foster and Jacob S. Levy and Onur Kuzucu and Kasturi Saha and Michal Lipson and Alexander L. Gaeta, M. A. Foster, J. S. Levy, O. Kuzucu, K. Saha, M. Lipson, A. L. Gaeta, and Mark A. Foster and Jacob S. Levy and Onur Kuzucu and Kasturi Saha and Michal Lipson and Alexander L. Gaeta, "Silicon-based monolithic optical frequency comb source," Optics Express, vol. 19, pp. 14233–14239, dec 2011.
- [18] M. Davanço, J. R. Ong, A. B. Shehata, A. Tosi, I. Agha, S. Assefa, F. Xia, W. M. J. Green, S. Mookherjea, K. Srinivasan, and M. Davanc, "Telecommunications-band heralded single photons from a silicon nanophotonic chip," Applied Physics Letters, vol. 100, no. 26, pp. 1–5, 2012.
- [19] E. Engin, D. Bonneau, C. M. Natarajan, A. S. Clark, M. G. Tanner, R. H. Hadfield, S. N. Dorenbos, V. Zwiller, K. Ohira, N. Suzuki, H. Yoshida, N. Iizuka, M. Ezaki, J. L. O'Brien, and M. G. Thompson, "Photon pair generation in a silicon micro-ring resonator with reverse bias enhancement.," Optics Express, vol. 21, no. 23, pp. 27826–27834, 2013.
- [20] S. Azzini, D. Grassani, M. Strain, M. Sorel, L. Helt, J. Sipe, M. Liscidini, M. Galli, and D. Bajoni, "Ultra-low power generation of twin photons in a compact silicon ring resonator," Optics Express, vol. 20, no. 21, pp. 23100–23107, 2012.
- [21] L. Wei and J. W. Y. Lit, "Compound ring resonator with double couplers," vol. 186, no. December, pp. 283–290, 2000.
- [22] M. A. Popović, T. Barwicz, M. S. Dahlem, F. Gan, C. W. Holzwarth, P. T. Rakich, M. R. Watts, H. I. Smith, F. X. Kärtner, and E. P. Ippen, "Hitless-reconfigurable and bandwidth-scalable silicon photonic circuits for telecom and interconnect applications," OFC/NFOEC 2008 - 2008 Conference on Optical Fiber Communication/National Fiber Optic Engineers Conference, pp. 11–13, feb 2008.

- [23] Q. Quan, I. B. Burgess, S. K. Y. Tang, D. L. Floyd, and M. Loncar, “Deterministic design of wavelength scale, ultra-high Q photonic crystal nanobeam cavities,” vol. 19, pp. 258–265, aug 2011.
- [24] P. B. Deotare, L. C. Kogos, I. Bulu, and M. Loncar, “Photonic Crystal Nanobeam Cavities for Tunable Filter and Router Applications,” IEEE Journal of Selected Topics in Quantum Electronics, vol. 19, pp. 3600210–3600210, mar 2013.
- [25] C. V. Poulton, X. Zeng, M. T. Wade, and M. A. Popović, “Channel add drop filter based on dual photonic crystal cavities in push pull mode,” Optics Letters, vol. 40, no. 18, pp. 4206–4209, 2015.
- [26] P. B. Deotare, M. W. McCutcheon, I. W. Frank, M. Khan, and M. Loncar, “Coupled photonic crystal nanobeam cavities,” Applied Physics Letters, vol. 95, no. 3, p. 031102, 2009.
- [27] S. Azzini, D. Grassani, M. Galli, D. Gerace, M. Patrini, M. Liscidini, P. Velha, and D. Bajoni, “Stimulated and spontaneous four-wave mixing in silicon-on-insulator coupled photonic wire nano-cavities,” Applied Physics Letters, vol. 103, no. 3, 2013.
- [28] C. M. Gentry, X. Zeng, and M. A. Popovic, “Tunable coupled-mode dispersion compensation and its application to on-chip resonant four-wave mixing,” Optics Letters, vol. 39, no. 19, pp. 5689–5692, 2014.
- [29] H. A. Haus, Waves and fields in optoelectronics. Prentice-Hall New Jersey, 1984.
- [30] K. Luke, A. Dutt, C. B. Poitras, and M. Lipson, “Overcoming Si₃N₄ film stress limitations for high quality factor ring resonators,” Optics Express, vol. 21, no. 19, p. 22829, 2013.
- [31] J. J. Wathen, V. R. Pagán, R. J. Suess, K.-Y. Wang, A. C. Foster, and T. E. Murphy, “Non-instantaneous optical nonlinearity of an a-Si:H nanowire waveguide,” Optics Express, vol. 22, no. 19, p. 22730, 2014.
- [32] J. Matres, G. C. Ballesteros, P. Gautier, J.-M. Fédéli, J. Martí, and C. J. Oton, “High nonlinear figure-of-merit amorphous silicon waveguides,” Optics express, vol. 21, no. 4, pp. 3932–40, 2013.
- [33] Q. Lin, J. Zhang, G. Piredda, R. W. Boyd, P. M. Fauchet, and G. P. Agrawal, “Dispersion of silicon nonlinearities in the near infrared region,” Applied Physics Letters, vol. 91, no. 2, pp. 2–4, 2007.
- [34] K. Ikeda, Y. Shen, and Y. Fainman, “Enhanced optical nonlinearity in amorphous silicon and its application to waveguide devices,” Opt. Express, vol. 15, no. 26, pp. 17761–17771, 2007.
- [35] B. Kuyken, H. Ji, S. Clemmen, S. K. Selvaraja, H. Hu, M. Pu, M. Galili, P. Jeppesen, G. Morthier, S. Massar, L. Oxenløwe, G. Roelkens, and R. Baets, “Nonlinear properties of and nonlinear processing in hydrogenated amorphous silicon waveguides,” Optics Express, vol. 19, no. 26, p. B146, 2011.
- [36] X. Gai, D.-Y. Choi, and B. Luther-Davies, “Negligible nonlinear absorption in hydrogenated amorphous silicon at 1.55 μm for ultra-fast nonlinear signal processing,” Optics express, vol. 22, no. 8, pp. 9948–58, 2014.

- [37] S. Kumar Selvaraja, M. Schaekers, W. Bogaerts, and D. Van Thourhout, “Deposited amorphous silicon-on-insulator technology for nano-photonics integrated circuits,” Optics Communications, vol. 313, pp. 210–216, 2014.
- [38] P. T. Rakich, M. A. Popović, M. Soljačić, and E. P. Ippen, “Trapping, corralling and spectral bonding of optical resonances through optically induced potentials,” Nature Photonics, vol. 1, no. 11, pp. 658–665, 2007.
- [39] G. E. J. Jr and F. A. Modine, “Parameterization of the optical functions of amorphous materials in the interband region,” Appl. Phys. Lett., vol. 69, no. 3, pp. 371–373, 1996.
- [40] Y. Abdurraheem, I. Gordon, T. Bearda, H. Meddeb, and J. Poortmans, “Optical bandgap of ultra-thin amorphous silicon films deposited on crystalline silicon by PECVD,” AIP Advances, vol. 4, no. 5, p. 057122, 2014.
- [41] A. A. Said, M. Sheik-Bahae, D. J. Hagan, T. H. Wei, J. Wang, J. Young, and E. W. V. Stryland, “Determination of bound-electronic and free-carrier nonlinearities in ZnSe, GaAs, CdTe, and ZnTe,” Journal of the Optical Society of America B, vol. 9, p. 405, mar 1992.
- [42] S. Santran, L. Canioni, L. Sarger, T. Cardinal, and E. Fargin, “Precise and absolute measurements of the complex third-order optical susceptibility,” Journal of the Optical Society of America B, vol. 21, no. 12, p. 2180, 2004.
- [43] G. P. AGRAWAL, Nonlinear Fiber Optics. 5th. Academic Press, 2013.
- [44] X. Zeng, T. Tran, J. S. Pelc, D. Kielinski, and R. G. Beausoleil, “Effects of non-instantaneous nonlinear absorption in hydrogenated amorphous silicon,” CLEO:2016, p. SM3R.6, 2016.
- [45] A. Yariv, “Coupled-mode theory for guided-wave optics,” IEEE Journal of Quantum Electronics, vol. 9, pp. 919–933, sep 1973.
- [46] A. Rodriguez, M. Solja, J. D. Joannopoulos, and S. G. Johnson, “ χ^2 and χ^3 harmonic generation at a critical power in inhomogeneous doublyresonant cavities,” Optics Express, vol. 15, no. 12, pp. 7303–7318, 2007.
- [47] Y. K. Chembo and N. Yu, “Modal expansion approach to optical-frequency-comb generation with monolithic whispering-gallery-mode resonators,” Physical Review A, vol. 82, p. 033801, sep 2010.
- [48] B. L. Weiss, “Acousto-optic Bragg diffraction in SiGe / Si planar waveguides,” IEE Proceedings Optoelectronics, vol. 143, no. 5, pp. 303–306, 1996.
- [49] C. M. Gentry, X. Zeng, and M. Popovic, “A Discrete Resonance, All-Order Dispersion Engineering Method for Microcavity Design for Four-wave Mixing,” Frontiers in Optics, p. FTu5D.3, 2014.
- [50] R. W. Boyd, Nonlinear optics. 3rd. Academic Press, 2008.
- [51] D. A. Fishman, C. M. Cirloganu, S. Webster, L. A. Padilha, M. Monroe, D. J. Hagan, and E. W. Van Stryland, “Sensitive mid-infrared detection in wide-bandgap semiconductors using extreme non-degenerate two-photon absorption,” Nature Photonics, vol. 5, no. 9, pp. 561–565, 2011.

- [52] J. S. Levy, A. Gondarenko, M. A. Foster, A. C. Turner-Foster, A. L. Gaeta, and M. Lipson, “CMOS-compatible multiple-wavelength oscillator for on-chip optical interconnects,” Nature Photonics, vol. 4, pp. 37–40, dec 2009.
- [53] Q. Lin, O. J. Painter, and G. P. Agrawal, “Nonlinear optical phenomena in silicon waveguides: modeling and applications,” Optics express, vol. 15, no. 25, pp. 16604–44, 2007.
- [54] L. G. Helt, M. Liscidini, and J. E. Sipe, “How does it scale? Comparing quantum and classical nonlinear optical processes in integrated devices,” Journal of the Optical Society of America B, vol. 29, no. 8, p. 2199, 2012.
- [55] P. P. Absil, J. V. Hryniewicz, B. E. Little, P. S. Cho, R. A. Wilson, L. G. Joneckis, and P. T. Ho, “Wavelength conversion in GaAs micro-ring resonators,” Optics letters, vol. 25, no. 8, pp. 554–556, 2000.
- [56] C. M. Gentry, G. T. Garces, X. Zeng, and M. A. Popović, “Passive Linewidth Narrowing Through Nondegenerate Optical Parametric Oscillation With Asymmetric Port Couplings,” Conference on Lasers and Electro-Optics, p. FF2M.6, 2016.
- [57] C. M. Gentry, G. T. Garces, X. Zeng, and M. A. Popović, “Tailoring of Individual Photon Lifetimes as a Degree of Freedom in Resonant Quantum Photonic Sources,” CLEO: 2016, p. JTu5A.17, 2016.
- [58] X. Zeng, C. M. Gentry, and M. A. Popović, “Four-wave mixing in silicon coupled-cavity resonators with port-selective , orthogonal supermode excitation,” Optics Letters, vol. 40, no. 9, pp. 2120–2123, 2015.
- [59] D. M. Ramirez, A. W. Rodriguez, H. Hashemi, J. D. Joannopoulos, M. Soljačić, and S. G. Johnson, “Degenerate four-wave mixing in triply resonant Kerr cavities,” Physical Review A, vol. 83, no. 3, p. 033834, 2011.
- [60] A. H. Atabaki and A. Adibi, “Demonstration of wavelength conversion in a reconfigurable coupled resonator in silicon,” IEEE Photonics Conference, pp. 399–400, 2011.
- [61] F. Morichetti, A. Canciamilla, C. Ferrari, A. Samarelli, M. Sorel, and A. Melloni, “Travelling-wave resonant four-wave mixing breaks the limits of cavity-enhanced all-optical wavelength conversion,” Nature communications, vol. 2, no. May, p. 296, 2011.
- [62] J. R. Ong, M. L. Cooper, G. Gupta, W. M. J. Green, S. Assefa, F. Xia, and S. Mookherjea, “Low-power continuous-wave four-wave mixing in silicon coupled-resonator optical waveguides,” Optics Letters, vol. 36, no. 15, pp. 2964–2966, 2011.
- [63] R. Kumar, J. R. Ong, J. Recchio, K. Srinivasan, and S. Mookherjea, “Spectrally multiplexed and tunable-wavelength photon pairs at 1.55 μ m from a silicon coupled-resonator optical waveguide,” Optics Letters, vol. 38, no. 16, pp. 2969–2971, 2013.
- [64] ePIXfab Multi-Project Wafer Service for Silicon Photonics. www.epixfab.eu.
- [65] M. Popovic, C. Manolatou, and M. Watts, “Coupling-induced resonance frequency shifts in coupled dielectric multi-cavity filters,” Optics Express, vol. 14, no. 3, pp. 1208–1222, 2006.

- [66] J. R. Ong, R. Kumar, R. Aguinaldo, and S. Mookherjea, "Efficient CW Four-Wave Mixing in Silicon-on-Insulator Micro-Rings With Active Carrier Removal," IEEE Photonics Technology Letters, vol. 25, no. 17, pp. 1699–1702, 2013.
- [67] M. A. Popović, "Theory and Design of High-Index-Contrast Microphotonic Circuits," 2008.
- [68] T. J. Kippenberg, S. M. Spillane, and K. J. Vahala, "Kerr-nonlinearity optical parametric oscillation in an ultrahigh-Q toroid microcavity," Physical Review Letters, vol. 93, no. 8, pp. 18–21, 2004.
- [69] L. Razzari, D. Duchesne, M. Ferrera, R. Morandotti, S. Chu, B. Little, and D. Moss, "Cmos-compatible integrated optical hyper-parametric oscillator," Nature Photonics, vol. 4, no. 1, pp. 41–45, 2009.
- [70] C. Diederichs, J. Tignon, G. Dasbach, C. Ciuti, A. Lemaître, J. Bloch, P. Roussignol, and C. Delalande, "Parametric oscillation in vertical triple microcavities," Nature, vol. 440, no. 7086, pp. 904–907, 2006.
- [71] M. A. Popović, "Sharply-defined optical filters and dispersionless delay lines based on loop-coupled resonators and "negative" coupling," Conference on Lasers and Electro-Optics (CLEO), p. CThP6, 2007.
- [72] M. A. Popović, T. Barwicz, P. T. Rakich, M. S. Dahlem, C. W. Holzwarth, F. Gan, L. Socci, M. R. Watts, H. I. Smith, F. X. Kärtner, and E. P. Ippen, "Experimental demonstration of loop-coupled microring resonators for optimally sharp optical filters," Conference on Lasers and Electro-Optics (CLEO), vol. 1, pp. 4–5, 2008.
- [73] W. D. Sacher and J. K. S. Poon, "Dynamics of microring resonator modulators.," Optics express, vol. 16, no. 20, pp. 15741–15753, 2008.
- [74] M. A. Popović, "Resonant optical modulators beyond conventional energy- efficiency and modulation frequency limitations," Integrated Photonics Research, p. IMC2, 2010.
- [75] M. F. Yanik, W. Suh, Z. Wang, and S. Fan, "Stopping light in a waveguide with an all-optical analog of electromagnetically induced transparency," Physical Review Letters, vol. 93, p. 233903, 2004.
- [76] M. Dahlem and C. Holzwarth, "Dynamical Slow Light Cell based on Controlled Far-Field Interference of Microring Resonators," Integrated Photonics Research, p. IMC4, 2010.
- [77] D. Dimitropoulos, R. Jhaveri, R. Claps, J. C. S. Woo, and B. Jalali, "Lifetime of photogenerated carriers in silicon-on-insulator rib waveguides," Applied Physics Letters, vol. 86, no. 7, p. 071115, 2005.
- [78] A. C. Turner-Foster, M. A. Foster, J. S. Levy, C. B. Poitras, R. Salem, A. L. Gaeta, and M. Lipson, "Ultrashort free-carrier lifetime in low-loss silicon nanowaveguides.," Optics express, vol. 18, no. 4, pp. 3582–3591, 2010.
- [79] A. H. Atabaki and A. Adibi, "Ultra-Compact Coupled-Resonator Device for Four-Wave-Mixing Applications," Conference on Lasers and Electro-Optics (CLEO), p. CTuS6, 2011.

- [80] H. Hashemi, A. W. Rodriguez, J. D. Joannopoulos, M. Soljačić, and S. G. Johnson, “Nonlinear harmonic generation and devices in doubly resonant Kerr cavities,” Physical Review A, vol. 79, no. 1, pp. 1–11, 2009.
- [81] F. Ö. Ilday and F. X. Kärtner, “Cavity-enhanced optical parametric chirped-pulse amplification,” Optics Letters, vol. 31, no. 5, p. 637, 2006.
- [82] M. A. Popović, M. R. Watts, T. Barwicz, P. T. Rakich, L. Socci, E. P. Ippen, F. X. Kärtner, and H. I. Smith, “High-Index-Contrast, Wide-FSR Microring-Resonator Filter Design and Realization with Frequency-Shift Compensation,” Optical Fiber Communication Conference and Exposition and The National Fiber Optic Engineers Conference, no. order 52, p. OFK1, 2005.
- [83] M. A. Popović, T. Barwicz, M. R. Watts, P. T. Rakich, L. Socci, E. P. Ippen, F. X. Kärtner, and H. I. Smith, “Multistage high-order microring-resonator add-drop filters.,” Optics letters, vol. 31, no. 17, pp. 2571–2573, 2006.
- [84] B. E. Little, S. T. Chu, H. A. Haus, J. Foresi, and J. Laine, “Microring Resonator Channel Dropping Filters.pdf,” Journal of Lightwave Technology, vol. 15, no. 6, pp. 998–1005, 1997.
- [85] M. Dašić and M. A. Popović, “Minimum drop-loss design of microphotonic microring-resonator channel add-drop filters,” in Telecommunications Forum (TELFOR), 2012 20th, no. 1, pp. 927–930, IEEE, 2012.
- [86] Wolfram Research Inc., Mathematica.
- [87] M. A. Popovic, T. Barwicz, F. Gan, M. S. Dahlem, C. W. Holzwarth, P. T. Rakich, H. I. Smith, E. P. Ippen, and F. X. Kärtner, “Transparent Wavelength Switching of Resonant Filters,” Conference on Lasers and Electro-Optics (CLEO), p. CPDA2, 2007.
- [88] O. Taussky and J. Todd, “Another Look at a Matrix of Mark Kac,” 1991.
- [89] S. M. Sze and K. K. Ng, Physics of semiconductor devices. Wiley, 2006.
- [90] A. R. Motamedi, A. H. Nejadmalayeri, A. Khilo, F. X. Kärtner, and E. P. Ippen, “Ultrafast nonlinear optical studies of silicon nanowaveguides,” Optics Express, vol. 20, no. 4, p. 4085, 2012.

Appendix A

Nonlinear coupling coefficients

In this chapter, expressions for the various nonlinear coupling coefficients defined in the coupled-mode theory for degenerate-pump four-wave mixing (see Eqs. 4.1) are derived. The formalism explained here can be readily extended to coupling coefficients in other nonlinear optical processes. Further, the approach of combining coupled-mode theory and perturbation theory also applies to linear optics, acousto-optics and electro-optics whenever the index perturbation is small.

We start with an introduction of notations used here. An optical field is usually characterized by its real electrical field component, $E(\mathbf{r}, t)$. It is convenient to represent the real field with a complex vector, $\mathbf{E}(\mathbf{r}, t)$, even though only its real part, $E(\mathbf{r}, t) = \Re[\mathbf{E}(\mathbf{r}, t)]$, has a physical meaning. In a microcavity, the electrical field consists of a summation of modes

$$\mathbf{E}(\mathbf{r}, t) = \sum_k \mathbf{E}(\omega_k) e^{j\omega_k t} = \sum_k a_k(t) \mathbf{e}_{k0}(\omega_k, \mathbf{r}) \quad (\text{A.1})$$

where k is mode number. $\mathbf{e}_{k0}(\omega_k, \mathbf{r})$ is the spatial profile of resonance mode k with a resonance frequency of ω_k , and it is usually chosen to have unit energy in the cavity so that $|a_k|^2$ is the energy in mode k . As an example, in a microring resonator it has a factor of $e^{j(-\gamma\theta + \phi)}$ for a travelling-wave mode, and $\cos(\gamma\theta + \phi)$ for a standing-wave mode, respectively. The complex mode amplitude $a_k(t)$ has a fast time dependence of $e^{j\omega_k t}$ and slow amplitude evolution $A_k(t)$, i.e., $a_k(t) = A_k(t) e^{j\omega_k t}$.

The third-order optical nonlinearity manifests itself by a nonlinear polarization

$$\mathbf{P}_i^{\text{NL}}(\omega_1 + \omega_2 + \omega_3) = \frac{1}{4} \epsilon_0 \sum_{jkl} \sum_{(\omega_1, \omega_2, \omega_3)} \bar{\chi}^{(3)}(\omega_1 + \omega_2 + \omega_3, \omega_1, \omega_2, \omega_3) \mathbf{E}_j(\omega_1) \mathbf{E}_k(\omega_2) \mathbf{E}_l(\omega_3) \quad (\text{A.2})$$

where $\overline{\overline{\chi}}^{(3)}$ is the nonlinear susceptibility ¹, $\mathbf{E}_j(\omega_1)$ denotes the j -th Cartesian component of the electric field at frequency ω_1 .

A.1 Nonlinear coupling coefficients and effective mode volume in microresonators

For linear unperturbed cavities, the coupled-mode equations take the form [29]:

$$\frac{da_k}{dt} = j\omega_k - r_{k,\text{tot}}a_k - j\sqrt{2r_{k,\text{ext}}s_{k,+}} \quad (\text{A.3})$$

where a_k is the complex amplitude of the k th resonance mode. This mode has a complex frequency of $\omega_k + jr_{k,\text{tot}}$, where the imaginary part corresponds to cavity field decay rate. When there is optical nonlinearity in the resonator, its complex resonance frequency changes as a result of change of complex refractive index characterized by nonlinear polarization[46]. According to the perturbation theory, $\delta\omega$ can be written as

$$\frac{\delta\omega_k}{\omega_k} = \frac{\int d^3\mathbf{x} \left(-\frac{1}{4}\delta\epsilon|\mathbf{E}_k|^2\right)}{\int d^3\mathbf{x} \left(\frac{1}{2}\epsilon|\mathbf{E}_k|^2\right)} = \frac{\int d^3\mathbf{x} \left(-\frac{1}{4}\mathbf{E}_k^* \cdot \mathbf{P}_k^{\text{NL}}\right)}{|a_k|^2} \quad (\text{A.4})$$

where $\mathbf{E}_k \equiv \mathbf{E}(\omega_k)$ (see Eq. A.1) is the unperturbed complex electric field profile of mode k , and \mathbf{P}^{NL} is the nonlinear polarization at frequency ω_k . We then replace ω_k in Eq. A.3 with $\omega_k + \delta\omega_k$, and compare Eq. A.3 with Eqs. 4.1 to solve for the nonlinear coupling coefficients. For example, the nonlinear complex polarization at the signal frequency ω_s is given by

$$\begin{aligned} \mathbf{P}_s^{\text{NL}} = & \frac{3}{4}\epsilon_0 \left(\overline{\overline{\chi}}^{(3)}(\omega_s; -\omega_i, \omega_p, \omega_p) : \mathbf{E}_i^* \mathbf{E}_p \mathbf{E}_p + \overline{\overline{\chi}}^{(3)}(\omega_s; -\omega_s, \omega_s, \omega_s) : \mathbf{E}_s^* \mathbf{E}_s \mathbf{E}_s \right. \\ & \left. + 2\overline{\overline{\chi}}^{(3)}(\omega_s; -\omega_p, \omega_p, \omega_s) : \mathbf{E}_p^* \mathbf{E}_p \mathbf{E}_s + 2\overline{\overline{\chi}}^{(3)}(\omega_s; -\omega_i, \omega_i, \omega_s) : \mathbf{E}_i^* \mathbf{E}_i \mathbf{E}_s \right). \quad (\text{A.5}) \end{aligned}$$

¹ Note we have chosen a definition of $\overline{\overline{\chi}}^{(3)}$ that is consistent with Boyd's book (see Eq. 1.3.20 in [50]), even though Boyd chooses $E(\mathbf{r}, t) = 2\Re[\mathbf{E}(\mathbf{r}, \mathbf{t})]$.

And the nonlinear coupling coefficients at ω_s are [46, 53]

$$\begin{aligned}\beta_{\text{fwm},s} &= \frac{\frac{3}{16}\epsilon_0 \int d^3\mathbf{x} \left(\mathbf{E}_s^* \cdot \overline{\overline{\chi}}^{(3)} : \mathbf{E}_i^* \mathbf{E}_p \mathbf{E}_p \right)}{a_s^* a_i^* a_p^2} \\ &= \frac{3\epsilon_0 \int d^3\mathbf{x} \left(\mathbf{E}_s^* \cdot \overline{\overline{\chi}}^{(3)} : \mathbf{E}_i^* \mathbf{E}_p \mathbf{E}_p \right)}{16 \sqrt{\int d^3\mathbf{x} \left(\frac{1}{2}\epsilon |\mathbf{E}_s|^2 \right)} \sqrt{\int d^3\mathbf{x} \left(\frac{1}{2}\epsilon |\mathbf{E}_i|^2 \right)} \int d^3\mathbf{x} \left(\frac{1}{2}\epsilon |\mathbf{E}_p|^2 \right)} e^{-j(\phi_s + \phi_i - 2\phi_p)}\end{aligned}\quad (\text{A.6})$$

$$\beta_{\text{pm},\text{ss}} + j\beta_{\text{tpa},\text{ss}} = \frac{3\epsilon_0 \int d^3\mathbf{x} \left(\mathbf{E}_s^* \cdot \overline{\overline{\chi}}^{(3)} : \mathbf{E}_s^* \mathbf{E}_s \mathbf{E}_s \right)}{16 \left(\int d^3\mathbf{x} \left(\frac{1}{2}\epsilon |\mathbf{E}_s|^2 \right) \right)^2} \quad (\text{A.7})$$

$$\beta_{\text{pm},\text{sp}} + j\beta_{\text{tpa},\text{sp}} = \frac{3\epsilon_0 \int d^3\mathbf{x} \left(\mathbf{E}_s^* \cdot \overline{\overline{\chi}}^{(3)} : \mathbf{E}_p \mathbf{E}_p^* \mathbf{E}_s \right)}{8 \int d^3\mathbf{x} \left(\frac{1}{2}\epsilon |\mathbf{E}_s|^2 \right) \int d^3\mathbf{x} \left(\frac{1}{2}\epsilon |\mathbf{E}_p|^2 \right)} \quad (\text{A.8})$$

$$\beta_{\text{pm},\text{si}} + j\beta_{\text{tpa},\text{si}} = \frac{3\epsilon_0 \int d^3\mathbf{x} \left(\mathbf{E}_s^* \cdot \overline{\overline{\chi}}^{(3)} : \mathbf{E}_i^* \mathbf{E}_i \mathbf{E}_s \right)}{8 \int d^3\mathbf{x} \left(\frac{1}{2}\epsilon |\mathbf{E}_s|^2 \right) \int d^3\mathbf{x} \left(\frac{1}{2}\epsilon |\mathbf{E}_i|^2 \right)} \quad (\text{A.9})$$

The phase of $\beta_{\text{fwm},s}$ relies on the choices of phase reference planes for a_k (with $a_k = |a_k|e^{j(\omega_k t - \phi)}$, $k \in \{s, i, p\}$), and we can set $(\phi_s + \phi_i - 2\phi_p) = 0$ in the CMT model without loss of generality. With the full permutation symmetry of $\overline{\overline{\chi}}^{(3)}$, we have $\beta_{\text{fwm},s} = \beta_{\text{fwm},i} = \beta_{\text{fwm},p}^*$ (the Manley-Rowe relations). The nonlinear coupling coefficients for the idler and pump light can be derived using a similar procedure. Notably all these coefficients depend on field overlap integral between interacting modes, and their relative magnitudes depend not only on the material nonlinearity parameter $\overline{\overline{\chi}}^{(3)}$ but also the resonator mode structures (see Sec. 4.2 for detailed discussion on this cavity mode topology). Besides, because $\overline{\overline{\chi}}^{(3)}$ is a tensor, the effective nonlinear coefficients depend on the polarizations of interacting optical fields. For example in a microring resonator based on anisotropic material such as crystalline silicon, the direction of the main electrical field component of the fundamental TE mode, varies azimuthally relative to the crystalline directions.

We then proceed to define an effective mode volume, V_{eff} , for four-wave mixing. For plane wave propagating in bulk nonlinear medium, the FWM coefficient, β_{fwm} , is directly related to the third-order susceptibility of the nonlinear material, $\overline{\overline{\chi}}^{(3)}$ as

$$\beta_{\text{fwm},s} = \frac{3\overline{\overline{\chi}}_{1111}^{(3)}}{4n_{\text{nl}}^4 \epsilon_0 V_{\text{nl}}} \quad (\text{A.10})$$

where n_{nl} is the refractive index of nonlinear material, ϵ_0 is vacuum permittivity, V_{nl} is the optical mode volume. In a microphotonic structure, the optical fields are tightly confined and the FWM

coefficient also depends on an overlap integral of the interacting mode fields. An effective mode volume in a microcavity, V_{eff} , can be defined as the equivalent bulk volume of nonlinear medium with the same $\overline{\overline{\chi}}^{(3)}$, in which uniform optical fields with the same energy would have equal nonlinearity (β_{fwm}). Thus we have

$$V_{\text{eff}} \equiv \frac{\overline{\overline{\chi}}_{1111}^{(3)} \sqrt{\int d^3\mathbf{x} (\epsilon|\mathbf{E}_s|^2) \int d^3\mathbf{x} (\epsilon|\mathbf{E}_i|^2) \int d^3\mathbf{x} (\epsilon|\mathbf{E}_p|^2)}}{\epsilon_0^2 n_{nl}^4 \int d^3\mathbf{x} (\mathbf{E}_s^* \cdot \overline{\overline{\chi}}^{(3)} : \mathbf{E}_p \mathbf{E}_p \mathbf{E}_i^*)}. \quad (\text{A.11})$$

A.2 Nonlinear coupling coefficients and effective mode area in waveguides

It is straightforward to derive the nonlinear interaction coefficients in an optical waveguide using the same approach as in a microcavity. For example for the signal light,

$$\begin{aligned} \frac{\partial a_s}{\partial z} = & j\beta_s [1 + (\beta_{\text{pm,ss}} + j\beta_{\text{tpa,ss}})|a_s|^2 + (\beta_{\text{pm,sp}} + j\beta_{\text{tpa,sp}})|a_p|^2 \\ & + (\beta_{\text{pm,sp}} + j\beta_{\text{tpa,sp}})|a_i|^2] a_s + j\beta_s \beta_{\text{fwm,s}} a_i^* a_p^2 \end{aligned} \quad (\text{A.12})$$

where a_s is the complex amplitude of the signal light with linear propagation constant β_s , normalized so that $|a_s|^2$ is the time-averaged optical power. All nonlinear coefficients ($\beta_{\text{pm,mn}}$, $\beta_{\text{tpa,pm}}$, and $\beta_{\text{fwm,m}}$, $m, n \in \{s, p, i\}$) in a waveguide have the unit of $[\frac{1}{\text{Watt}}]$ in contrast to $[\frac{1}{\text{Joule}}]$ in a resonator, and are given by

$$\beta_{\text{fwm,s}} = \frac{3\epsilon_0\omega_s \int d^2\mathbf{x} (\mathbf{E}_s^* \cdot \overline{\overline{\chi}}^{(3)} : \mathbf{E}_i^* \mathbf{E}_p \mathbf{E}_p)}{16\beta_s \sqrt{\int d^2\mathbf{x} \frac{1}{2} \Re(\mathbf{E}_s^* \times \mathbf{H}_s \cdot \mathbf{e}_z)} \sqrt{\int d^2\mathbf{x} \frac{1}{2} \Re(\mathbf{E}_i^* \times \mathbf{H}_i \cdot \mathbf{e}_z)} \int d^2\mathbf{x} \frac{1}{2} \Re(\mathbf{E}_p^* \times \mathbf{H}_p \cdot \mathbf{e}_z)} \quad (\text{A.13})$$

$$\beta_{\text{pm,ss}} + j\beta_{\text{tpa,ss}} = \frac{3\epsilon_0\omega_s \int d^2\mathbf{x} (\mathbf{E}_s^* \cdot \overline{\overline{\chi}}^{(3)} : \mathbf{E}_s^* \mathbf{E}_s \mathbf{E}_s)}{16\beta_s |\int d^2\mathbf{x} \frac{1}{2} \Re(\mathbf{E}_s^* \times \mathbf{H}_s \cdot \mathbf{e}_z)|^2} \quad (\text{A.14})$$

$$\beta_{\text{pm,sp}} + j\beta_{\text{tpa,sp}} = \frac{3\epsilon_0\omega_s \int d^2\mathbf{x} (\mathbf{E}_s^* \cdot \overline{\overline{\chi}}^{(3)} : \mathbf{E}_p^* \mathbf{E}_p \mathbf{E}_s)}{8\beta_s \int d^2\mathbf{x} \frac{1}{2} \Re(\mathbf{E}_s^* \times \mathbf{H}_s \cdot \mathbf{e}_z) \int d^2\mathbf{x} \frac{1}{2} \Re(\mathbf{E}_p^* \times \mathbf{H}_p \cdot \mathbf{e}_z)} \quad (\text{A.15})$$

$$\beta_{\text{pm,si}} + j\beta_{\text{tpa,si}} = \frac{3\epsilon_0\omega_s \int d^2\mathbf{x} (\mathbf{E}_s^* \cdot \overline{\overline{\chi}}^{(3)} : \mathbf{E}_i^* \mathbf{E}_i \mathbf{E}_s)}{8\beta_s \int d^2\mathbf{x} \frac{1}{2} \Re(\mathbf{E}_s^* \times \mathbf{H}_s \cdot \mathbf{e}_z) \int d^2\mathbf{x} \frac{1}{2} \Re(\mathbf{E}_i^* \times \mathbf{H}_i \cdot \mathbf{e}_z)} \quad (\text{A.16})$$

It should be noted that $\overline{\overline{\chi}}^{(3)}$ is a tensor and thus the field overlap integral in nonlinear coefficients (say β_{fwm}) depend on the orientation of optical waveguide made of anisotropic material such as

crystalline silicon. Next, an effective nonlinear mode area, A_{eff} , can be defined in a waveguide as the equivalent bulk area of nonlinear medium with the same $\overline{\overline{\chi}}^{(3)}$, in which uniform optical fields with the same power would have equal nonlinearity (β_{fwm})

$$\beta_{\text{fwm}} \equiv \frac{3\omega_s \overline{\overline{\chi}}_{1111}^3}{4\beta_s \epsilon_0 c^2 n_{\text{nl}}^2} \frac{1}{A_{\text{eff}}} \quad (\text{A.17})$$

The nonlinear mode area, A_{eff} , is different from the conventional linear mode area defined as the ratio of power and peak intensity.

A.3 Conversion formulas for nonlinear parameters

We summarize the relationship between the microscopic $\overline{\overline{\chi}}^{(3)}$ and some nonlinear parameters common in the literature. The Kerr coefficient n_2 is defined by the ratio of index change versus intensity, $\Delta n = n_2 I$, and the two-photon absorption coefficient in a bulk medium is defined by the ratio of TPA loss versus intensity, $dI/dz = -\alpha I - \beta_{\text{TPA}} I^2$, where I is light intensity in bulk medium given by $I = \frac{1}{2} \epsilon_0 n_{\text{nl}} c |\mathbf{E}|^2$, c is speed of light. Besides the nonlinear parameter γ in a waveguide is defined via $da/dz = j\gamma |a|^2 a$, where $|a|^2$ is the optical power. Using Eq. A.2 for a plane wave in uniform bulk nonlinear medium, we have the nonlinear refractive index change expressed in three ways

$$\begin{aligned} \Delta \epsilon &= \frac{3}{4} \epsilon_0 \overline{\overline{\chi}}^{(3)} |\mathbf{E}|^2 \\ &= 2\epsilon_0 n_{\text{nl}} (\Delta n + j\Delta \kappa) = 2\epsilon_0 n_{\text{nl}} (n_2 I + j \frac{c\beta_{\text{TPA}}}{2\omega} I) \\ &= 2\epsilon_0 n_{\text{nl}} (\Delta n + j\Delta \kappa) = 2\epsilon_0 n_{\text{nl}} (\frac{cI A_{\text{eff}}}{\omega}) \gamma \end{aligned} \quad (\text{A.18})$$

where A_{eff} is the effective mode area (see Eq. A.17). Thus the nonlinear parameters are related as follows

$$\frac{\omega}{c} n_2 + \frac{i}{2} \beta_{\text{TPA}} = \frac{3\omega}{4\epsilon_0 c^2 n_{\text{nl}}^2} \overline{\overline{\chi}}_{1111}^{(3)} = \gamma A_{\text{eff}} = \frac{\omega \beta_{\text{fwm}} n_{\text{nl}}^2 V_{\text{eff}}}{c^2} \quad (\text{A.19})$$

A.4 Comparison of nonlinear coupling coefficients in single- and triple-cavity resonators with travelling-wave and standing-wave excitations

In this section we use the general expressions for nonlinear coupling coefficients derived in A.1 to compare third-order nonlinearity in single- and triple-cavity resonator with travelling-wave and standing-wave excitations, respectively. Without loss of generality we assume that resonance modes of these resonators have the same transverse field profile, and they only differ in the longitudinal (propagation) direction. We also assume each constituent cavity of the triple-cavity resonator is the same as the single-cavity resonator. As an example, we compare the longitudinal field profiles of these resonators illustrated in Fig. 4.3 and summarized in Table. A.1.

The travelling-wave resonance modes of both single- and triple-ring resonators have azimuthally uniform intensity in each ring, while the standing-wave modes have sinusoidally varying intensity around the ring. Besides, the triple-ring resonator supermodes all have unequal energy in each constituent cavity. However, all supermodes (signal, pump and idler) have the same longitudinal order (i.e., angular propagation constant m), in contrast to the single-ring resonator where the three waves interacting in FWM have different longitudinal order ($m - n$, m and $m + n$). As a result of differences in their mode structures, these resonators have different nonlinear coupling coefficients (see Table. 4.2). We address such mode-dependent effective nonlinearity in Sec. 4.2.

The nonlinear coupling coefficients in different resonators can be compared using Eqs. A.6–A.9. As an example, we compare four-wave mixing coefficients in the single- and triple-ring resonators with travelling-wave excitations

$$\frac{\beta_{\text{fwm}}^{\text{SR,TW}}}{\beta_{\text{fwm}}^{\text{TR,TW}}} = \frac{V_{\text{eff}}^{\text{TR,TW}}}{V_{\text{eff}}^{\text{SR,TW}}} = \frac{\int_0^{2\pi} d\theta_1 \frac{1}{2} e^{jm\theta_1} \cdot \left(\frac{1}{\sqrt{2}} e^{-jm\theta_1}\right)^2 \cdot \frac{1}{2} e^{jm\theta_1} + \int_0^{2\pi} d\theta_3 \frac{1}{2} e^{jm\theta_3} \cdot \left(-\frac{1}{\sqrt{2}} e^{-jm\theta_3}\right)^2 \cdot \frac{1}{2} e^{jm\theta_3}}{\int_0^{2\pi} d\theta e^{j(m-n)\theta} \cdot e^{-2jm\theta} \cdot e^{j(m+n)\theta}}$$

$$= 4 \tag{A.20}$$

The effective mode volume for degenerate-pump FWM in travelling-wave triple-ring resonators increases to four, rather than three, times that in a single constituent ring resonator due to non-

Table A.1: Comparison of longitudinal field profiles of single- and triple-ring resonator with travelling-wave and standing-wave excitations. Each constituent ring of the triple-ring cavity is identical to the single-ring cavity. The amplitude of each field has been chosen to have equal energy in all resonator.

Resonator	Signal field	Pump field	Idler field
1-ring, TW	$e^{-j(m-n)\theta}$	$e^{-jm\theta}$	$e^{-j(m+n)\theta}$
3-ring, TW	$(\frac{1}{2}e^{-jm\theta_1}, \frac{1}{\sqrt{2}}e^{-jm\theta_2}, \frac{1}{2}e^{-jm\theta_3})$	$(\frac{1}{\sqrt{2}}e^{-jm\theta_1}, 0, -\frac{1}{\sqrt{2}}e^{-jm\theta_3})$	$(\frac{1}{2}e^{-jm\theta_1}, -\frac{1}{\sqrt{2}}e^{-jm\theta_2}, \frac{1}{2}e^{-jm\theta_3})$
1-ring, SW	$\sqrt{2}\cos[(m-n)\theta]$	$\sqrt{2}\cos[m\theta]$	$\sqrt{2}\cos[(m+n)\theta]$
3-ring, SW	$(\frac{\sqrt{2}}{2}\cos[m\theta_1], \cos[m\theta_2], \frac{\sqrt{2}}{2}\cos[m\theta_3])$	$(\cos[m\theta_1], 0, -\cos[m\theta_3])$	$(\frac{\sqrt{2}}{2}\cos[m\theta_1], -\cos[m\theta_2], \frac{\sqrt{2}}{2}\cos[m\theta_3])$

uniform energy distribution. In spite of larger nonlinear mode volume, a triple-cavity resonator wins over a single-cavity resonator with automatic phase matching and frequency matching (allowing for smaller constituent cavity), freedom in choice of resonance wavelength, resonance mode linewidth engineering, separation of strong pump light and weak signal and so on (see Sec. 2.3.1).

A.5 Free carrier absorption coefficients

Here we derive the loss rate of cavity mode amplitude envelop (A_k in the CMT model, for $k \in s, p, i$) due to free carrier absorption induced by two-photon absorption [see Eq. (4.6)]. On the one hand, free carriers are created through TPA with equal densities. In general, the dynamics of free carrier density, N_ν , is governed by the continuity equation [89]

$$\frac{\partial N_\nu}{\partial t} = G - \frac{N_\nu}{\tau_\nu} + D_\nu \nabla^2 N_\nu - s_\nu \mu_\nu \nabla \cdot (N_\nu \mathbf{E}_{dc}) \equiv G - \frac{N_\nu}{\tau_{\nu, \text{eff}}} \quad (\text{A.21})$$

where $\nu = e$ for electrons, $\nu = h$ for holes, $s_h = 1$, $s_e = -1$, D_ν is the diffusion coefficient, μ_ν is the mobility, \mathbf{E}_{dc} is applied dc electric field, τ_ν is the carrier lifetime, and $\tau_{\nu, \text{eff}}$ is the effective carrier lifetime that includes all the effects of recombination, diffusion and drift. G is the free carrier generation rate per volume due to TPA, where one pair of electron and hole is generated for every two photons absorbed

$$G = \frac{1}{2\hbar\omega} \frac{\Delta E}{\Delta t \cdot \Delta V} = \frac{1}{4\hbar\omega} \Re[\mathbf{E}_{\text{tot}}^* \cdot \mathbf{J}] = \frac{1}{4\hbar\omega} \Re[j\omega\epsilon_0 \mathbf{E}_{\text{tot}}^* \cdot \overline{\overline{\chi}}^{(3)} : \mathbf{E}_{\text{tot}}^3] \quad (\text{A.22})$$

where \mathbf{E}_{tot} is total electric field ($\mathbf{E}_{\text{tot}} = \mathbf{E}_s + \mathbf{E}_p + \mathbf{E}_i$). Thus the steady-state free carrier density is given by

$$N_\nu = G\tau_{\nu,\text{eff}}. \quad (\text{A.23})$$

On the other hand, these free carriers contribute to optical loss. The free carrier absorption coefficient of optical power (absorption rate per distance) is

$$\alpha_\nu = \sigma_\nu N_\nu \quad (\text{A.24})$$

where σ_ν is free carrier absorption cross section area. Note that both $\tau_{\nu,\text{eff}}$ and G are position-dependent, and therefore the free carrier absorption coefficient α_ν is non-uniform across the waveguide cross section. Besides, the optical field intensity is also non-uniform. As a result, the interplay between free carriers and optical field needs to be studied carefully. If the field decay rate due to free carrier loss is much smaller than the cavity resonance frequency, we can include the FCA loss into the perturbation theory of CMT model, with the free carrier loss rate of mode k (for $k \in s, p, i$) due to free carrier ν as

$$\begin{aligned} r_{\text{k,FC}}^\nu &= -\frac{j\omega \int d^3\mathbf{x} \left(\mathbf{E}_k^* \cdot \delta\mathbf{P}_k^{(\text{FCA},\nu)} \right)}{4 \int d^3\mathbf{x} \left(\frac{1}{2}\epsilon|\mathbf{E}_k|^2 \right)} = \frac{\omega \int d^3\mathbf{x} \left(\epsilon_0 n_{\text{nl}} \frac{\alpha_\nu}{k_0} |\mathbf{E}_k|^2 \right)}{4 \int d^3\mathbf{x} \left(\frac{1}{2}\epsilon|\mathbf{E}_k|^2 \right)} \\ &= \frac{\epsilon_0 n_{\text{nl}} \omega \sigma_\nu \int d^3\mathbf{x} \left(G\tau_{\nu,\text{eff}} |\mathbf{E}_k|^2 \right)}{4k_0 \int d^3\mathbf{x} \left(\frac{1}{2}\epsilon|\mathbf{E}_k|^2 \right)} = \frac{c\epsilon_0^2 n_{\text{nl}} \sigma_\nu \int d^3\mathbf{x} \left(\tau_{\nu,\text{eff}} (\mathbf{E}_{\text{tot}}^* \cdot \Im[\overline{\chi}^{(3)}] : \mathbf{E}_{\text{tot}}^3) |\mathbf{E}_k|^2 \right)}{16\hbar \int d^3\mathbf{x} \left(\frac{1}{2}\epsilon|\mathbf{E}_k|^2 \right)}. \end{aligned} \quad (\text{A.25})$$

This expression for free carrier absorption rate is true, but very complex to solve. We make some assumptions to simplify the expression above. First, we assume the effective free carrier lifetime, $\tau_{\nu,\text{eff}}$, is the same for electrons and holes. Second, we assume the steady-state free carrier density generated by TPA is uniform (invariant with respect to position) in the cavity. This assumption is valid when the carrier density equilibrates due to a diffusion that is much faster than recombination [90], or a fast drift due to an applied field for carrier sweepout. With these assumptions, we use the effective volume of nonlinear interaction, V_{eff} (defined in Sec. A.1), to

average out the free carrier density, N_ν . From Eqs. (6.1a)-(6.1c), using $\frac{\partial N_\nu}{dt} = -\frac{N_\nu}{\tau_{\text{eff}}} + \frac{1}{2\hbar\omega V_{\text{eff}}} \frac{d|A_k|^2}{dt} = 0$, we have

$$N_\nu = \frac{\tau_{\text{eff}}}{\hbar V_{\text{eff}}} (\beta_{\text{tpa,ss}}|A_s|^4 + \beta_{\text{tpa,pp}}|A_p|^4 + \beta_{\text{tpa,ii}}|A_i|^4 + 4\beta_{\text{tpa,sp}}|A_s|^2|A_p|^2 + 4\beta_{\text{tpa,ip}}|A_i|^2|A_p|^2 + 4\beta_{\text{tpa,si}}|A_s|^2|A_i|^2). \quad (\text{A.26})$$

The optical field decay rate due to FCA is given by

$$r_{\text{FC}} = \frac{\alpha_{\text{FC}} v_g}{2} = \frac{\sigma_a N_\nu v_g}{2} = \frac{\tau_{\text{eff}} \sigma_a v_g}{2\hbar V_{\text{eff}}} (\beta_{\text{tpa,ss}}|A_s|^4 + \beta_{\text{tpa,pp}}|A_p|^4 + \beta_{\text{tpa,ii}}|A_i|^4 + 4\beta_{\text{tpa,sp}}|A_s|^2|A_p|^2 + 4\beta_{\text{tpa,ip}}|A_i|^2|A_p|^2 + 4\beta_{\text{tpa,si}}|A_s|^2|A_i|^2) \quad (\text{A.27})$$

where σ_a is the free carrier absorption cross section area, including contributions from both free electrons and holes, v_g is group velocity of optical modes. σ_a and v_g both only have a meaning in the context of resonators formed from a waveguide, such as microring or waveguide Fabry-Perot resonators. The expression is still valid for 3D standing wave cavities such as photonic crystal microcavities, where only the product $\sigma_a v_g$ as a whole has a unique physical meaning.

One should note that in Eq. A.27 there is a factor of 4 for the term due to cross-TPA compared to that for self-TPA. The enhanced two-photon absorption rate when two different photons are absorbed results from quantum interference. As Fig. A.1 shows, there are two atomic transition paths ($1 - 2 - 3$ and $1 - 2' - 3$) between a pair of initial and final state in cross-TPA, in contrast to a single path in self-TPA. Since the intermediate state $|2\rangle$ and $|2'\rangle$ are virtual states, the two paths have the same magnitude. As a result, the total transition amplitude from $|1\rangle$ to $|3\rangle$ gains a factor of 2, leading to the factor of 4 in free carrier generation rate due to cross-TPA compared to self-TPA.

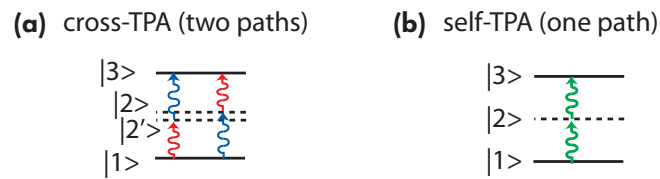


Figure A.1: Illustration of the atomic transition processes in cross two-photon absorption (cross TPA) and self two-photon absorption (self TPA). For the atomic transition from electronic state $|1\rangle$ to $|3\rangle$, there are two transition paths in cross TPA compared to a single transition path in self TPA. As a result of the quantum interference between the two transition paths, cross TPA has a factor of 4 in generating free carriers compared to self TPA.